MALS SALT-NOT Survey of MIR-selected Powerful Radio-bright AGN at $0 < z < 3.5$

N. Gupta, G. Shukla, R. Srianand, J. -K. Krogager, P. Noterdaeme, A. J. Baker, F. Combes, J. P. U. Fynbo, E. Momjian, M. Hilton, et al.

To cite this version:

N. Gupta, G. Shukla, R. Srianand, J. -K. Krogager, P. Noterdaeme, et al.. MALS SALT-NOT Survey of MIR-selected Powerful Radio-bright AGN at $0 < z < 3.5$. The Astrophysical Journal, 2022, 929, ⟨10.3847/1538-4357/ac4220⟩. ⟨insu-03717120⟩

The Astrophysical Journal, 929:108 (41pp), 2022 April 10 https://doi.org/10.3847/1538-4357/ac4220

MALS SALT-NOT Survey of MIR-selected Powerful Radio-bright AGN at $0 < z < 3.5$

N. Gupta[1], G. Shukla[1], R. Srianand[1], J.-K. Krogager[2], P. Noterdaeme[2], A. J. Baker[3], F. Combes[4], J. P. U. Fynbo[5,6], E. Momjian[7], M. Hilton[8], T. Hussain[1], K. Moodley[8], P. Petitjean[2], H.-W. Chen[9], P. Deka[1], R. Dutta[10], J. Jose[11], G. I. G. Józsa[12,13,14], C. Kaski[11], H.-R. Klöckner[15], K. Knowles[8], S. Sikhosana[8], and J. Wagenveld[15]

[1] Inter-University Centre for Astronomy and Astrophysics, Post Bag 4, Ganeshkhind, Pune 411 007, India
[2] Institut d'Astrophysique de Paris, UMR 7095, CNRS-SU, 98bis bd Arago, F-75014 Paris, France; ngupta@iucaa.in
[3] Department of Physics and Astronomy, Rutgers, the State University of New Jersey, 136 Frelinghuysen Road, Piscataway, NJ 08854-8019, USA
[4] Observatoire de Paris, Collège de France, PSL University, Sorbonne University, CNRS, LERMA, Paris, France
[5] Cosmic Dawn Center (DAWN), University of Copenhagen, Jagtvej 128, DK-2200, Copenhagen N, Denmark
[6] Niels Bohr Institute, University of Copenhagen, Jagtvej 128, DK-2200, Copenhagen N, Denmark
[7] National Radio Astronomy Observatory, P.O. Box O, Socorro, NM 87801, USA
[8] Astrophysics Research Centre and School of Mathematics, Statistics and Computer Science, University of KwaZulu-Natal, Durban 4041, South Africa
[9] Department of Astronomy & Astrophysics, The University of Chicago, 5640 South Ellis Avenue, Chicago, IL 60637, USA
[10] Dipartimento di Fisica G. Occhialini, Università degli Studi di Milano Bicocca, Piazza della Scienza 3, I-20126 Milano, Italy
[11] ThoughtWorks Technologies India Private Limited, Yerawada, Pune 411 006, India
[12] South African Radio Astronomy Observatory, 2 Fir Street, Black River Park, Observatory 7925, South Africa
[13] Department of Physics and Electronics, Rhodes University, P.O. Box 94, Makhanda, 6140, South Africa
[14] Argelander-Institut für Astronomie, Auf dem Hügel 71, D-53121 Bonn, Germany
[15] Max-Planck-Institut für Radioastronomie, Auf dem Hügel 69, D-53121 Bonn, Germany

Received 2021 July 20; revised 2021 December 5; accepted 2021 December 8; published 2022 April 18

Abstract

We present results of an optical spectroscopic survey using SALT and the Nordic Optical Telescope to build a Wide-field Infrared Survey Explorer mid-infrared color-based, dust-unbiased sample of powerful radio-bright (>200 mJy at 1.4 GHz) active galactic nuclei (AGN) for the MeerKAT Absorption Line Survey (MALS). Our sample has 250 AGN (median $z = 1.8$) showing emission lines, 26 with no emission lines, and 27 without optical counterparts. Overall, our sample is fainter ($\Delta i = 0.6$ mag) and redder ($\Delta(g-i) = 0.2$ mag) than radio-selected quasars, and representative of fainter quasar population detected in optical surveys. About 20% of the sources are narrow-line AGN (NLAGN)–65% of these, at $z < 0.5$ are galaxies without strong nuclear emission, and 10% at $z > 1.9$, have emission line ratios similar to radio galaxies. The farthest NLAGN in our sample is M1513-2524 ($z_{\rm em} = 3.132$), and the largest radio source (size ∼330 kpc) is M0909-3133 ($z_{\rm em} = 0.884$). We discuss in detail 110 AGN at $1.9 < z < 3.5$. Despite representing the radio loudest quasars (median $R = 3685$), their Eddington ratios are similar to the Sloan Digital Sky Survey quasars having lower R. We detect four C IV broad-absorption line (BAL) QSOs, all among AGN with least R, and highest black hole masses and Eddington ratios. The BAL detection rate ($4^{+3}_{-2}\%$) is consistent with that seen in extremely powerful ($L_{1.4\rm GHz} > 10^{25}$ W Hz^{-1}) quasars. Using optical light curves, radio polarization, and γ-ray detections, we identify seven high-probability BL Lacertae objects. We also summarize the full MALS footprint to search for H I 21 cm and OH 18 cm lines at $z < 2$.

Unified Astronomy Thesaurus concepts: Active galactic nuclei (16); Quasars (1319); Broad-absorption line quasar (183); Blazars (164)

Supporting material: machine-readable table

1. Introduction

Active galactic nuclei (AGN) radiate across the entire electromagnetic spectrum but in their early phases of evolution the thermal emission from the accretion disk especially at UV to optical wavelengths can be obscured by the dusty material fueling the central engine. Subsequently, as the radiative and mechanical feedback clears the obscuring material the central AGN can become observable as optically selected AGN (e.g., Sanders & Mirabel 1996). The direct view of the accretion disk may also be blocked by a dusty *torus*, which has been postulated to explain the appearances of different types of AGN through orientation-based unification schemes (e.g., Urry & Padovani 1995). In this paradigm, type I and type II AGN appear different merely due to varying amounts of dust along the observer's line of sight. The redder AGN are then more obscured simply because they are being viewed at inclinations closer to the equatorial plane of the torus.

In principle, AGN can also be obscured by dust from high-column density H I absorbers, such as damped Lyα systems (DLAs), which are defined to have N(H I) $>2 \times 10^{20}$ cm^{-2} (Wolfe & Prochaska 2000) and associated with intervening galaxies intercepting the line of sight. Despite the availability of large samples of intervening DLAs (e.g., Noterdaeme et al. 2009; Parks et al. 2018) and the fact that they trace the bulk of neutral hydrogen in the universe (Wolfe et al. 2005), the detected DLAs show little dust (e.g., Murphy & Liske 2004) and only a small fraction exhibit the presence of molecular hydrogen (Petitjean et al. 2000; Ledoux et al. 2003; Noterdaeme et al. 2008; Srianand et al. 2012; Muzahid et al. 2015; Noterdaeme et al. 2015; Balashev & Noterdaeme 2018; Zahedy et al. 2020; Boettcher et al. 2021).

Interestingly, none of the DLAs detected to date have properties similar to dense molecular clouds in the galaxy. In fact, PKS 1830-211, which exhibits extreme reddening (visual extinction, $A_V > 5.8$; Mathur & Nair 1997) due to an intervening absorber at $z = 0.89$ with properties similar to dense molecular clouds, was identified on the basis of its peculiar radio spectrum and morphology (Pramesh Rao & Subrahmanyan 1988; Jauncey et al. 1991). The redshift $z = 0.89$ of the lensing galaxy responsible for the intervening absorption was discovered through a spectroscopically blind search of molecular absorption at millimeter wavelengths (Wiklind & Combes 1996). A dust-unbiased census of DLAs is required to correctly estimate the key observables such as H I and metal mass densities of the universe, and the extent of dust-obscured AGN missed in UV-optical color-based surveys (e.g., Pei et al. 1991; Srianand & Kembhavi 1997; Ellison et al. 2001; Pontzen & Pettini 2009; Frank & Péroux 2010; Krogager et al. 2019).

Regardless of the origin of obscuration, it is desirable to build dust-unbiased samples of AGN to distinguish between competing paradigms based on evolution or orientation to understand the AGN population itself and its impact on galaxy evolution via feedback (e.g., Fabian 2012; Heckman & Best 2014). The most effective techniques to achieve this are naturally based on photometric selection at hard X-ray, mid-infrared (MIR) or radio wavelengths. In recent years the AllWISE catalog from the Wide-field Infrared Survey Explorer (WISE; Wright et al. 2010; Cutri et al. 2014) in its four bands, namely, W1 (3.4 μm), W2 (4.6 μm), W3 (12 μm), and W4 (22 μm) has emerged as an excellent resource to identify obscured AGN across the full sky. The 5σ point-source sensitivities of the WISE All-Sky release in the four bands in Vega-based magnitudes are 16.83, 15.60, 11.32, and 8.0, respectively.

The MIR selection of AGN works exactly in the same manner as the traditional optical color selection except that it is less susceptible to dust extinction. The near-IR spectrum of an AGN is simply an extension of the UV-optical power law. The MIR and longer wavelength IR emission comes from the hot dust in the *torus,* which absorbs UV-optical emission and reprocesses it (Netzer et al. 2007). All these give rise to a power-law spectrum that dominates at wavelengths longer than $\sim$1 μm and is easily distinguishable from a declining Rayleigh–Jeans spectrum of galaxies and stars in MIR color space up to $z \sim 3$. Thus, the MIR color selection can potentially detect obscured AGN missed in UV-optical and even X-ray selections over a wide redshift range (e.g., Lacy et al. 2004; Stern et al. 2005; Mateos et al. 2012; Stern et al. 2012).

Taking advantage of the segregation of various classes of objects, i.e., stars, early-type and spiral galaxies, brown dwarfs, and AGN in the WISE color space (see Figure 12 of Wright et al. 2010), several AGN identification techniques based on the AllWISE data release have been proposed in the literature. The majority of these are based on the W1 and W2 i.e., the two most sensitive bands of WISE (see Assef et al. 2018, for a large all sky catalog of AGN), and have been shown to yield AGN space density much higher than those from the optical and X-ray surveys (Stern et al. 2005; Assef et al. 2010). The MIR colors corresponding to Fermi detected AGN have been used to build large samples ($\sim$15,000) of blazars (D'Abrusco et al. 2019). The MIR color diagnostic has also been applied to identify dual AGN candidates, which represent a crucial and rare stage in the galaxy evolution (e.g., Satyapal et al. 2017).

In this paper, we present a MIR color scheme based on W1, W2, and W3 that efficiently selects quasars at $z > 1.4$. We have also carried out a large spectroscopic campaign using the Nordic Optical Telescope (NOT) and the Southern African Large Telescope (SALT) to measure the redshifts and confirm the nature of a subset of AGN candidates identified using our MIR color scheme. The NOT component of the survey has already been presented by Krogager et al. (2018). Here we present the complete SALT-NOT catalog of the 303 AGN at $0 < z < 3.5$ that constitutes radio sources brighter than 200 mJy at $\sim$1.4 GHz in the NRAO VLA Sky Survey (NVSS; Condon et al. 1998) and at decl. $\delta < +20°$.

The SALT-NOT sample represents a small minority of AGN that are extremely powerful in radio with 1.4 GHz spectral luminosity, $L_{1.4\mathrm{GHz}} > 10^{24}$ W Hz^{-1}. In past many studies have attempted to isolate the physical mechanisms responsible for the quasar radio-loudness dichotomy. The massive black holes (BHs) in radio-loud AGN are found to be systematically a few times heavier than those in their radio-quiet counterparts (e.g., Laor 2000). A further interesting trend that has emerged from these studies is the anticorrelation between the Eddington ratio and radio loudness (e.g., Sikora et al. 2007). The physical parameters such as BH mass, spin, and accretion rate along with the in situ magnetic field are believed to determine the extent of radio loudness and overall appearance of the AGN (e.g., Sikora & Begelman 2013). The SALT-NOT sample offers an opportunity to revisit these issues for extremely radio-loud quasars selected through MIR colors.

This paper is organized as follows. In Section 2, we present details of radio–infrared–optical crossmatching to select candidates for the SALT-NOT survey and the sample selection criteria. The latter is based on the requirements of the MeerKAT Absorption Line Survey (MALS; see Gupta et al. 2016 for key science objectives), an ongoing large survey at the South African precursor (Jonas & MeerKAT Team 2016) of the upcoming Square Kilometer Array (SKA). In Section 3, we present the details of SALT observations and data analysis. These details for the NOT component of the survey are available in Krogager et al. (2018). The details of emission line identification, redshift measurement, and AGN classifications based on the SALT-NOT spectra are provided in Section 4. Section 5 presents selected results based on radio continuum and optical emission line properties. For AGN at $1.9 < z < 3.5$, we also estimate BH masses, accretion rates, and the occurrence of broad-absorption lines (BALs), and revisit the issue of their dependence on radio loudness. We also discuss emission line less AGN with highest optical photometric variability and the targets with no optical counterparts. Finally, in Section 6, we summarize the results and complement the SALT-NOT catalog with AGN from the literature to assemble a target list of $\sim$650 AGN defining the MALS footprint to search for cold atomic and molecular gas at $z < 2$.

Throughout this paper we use a ΛCDM cosmology with $\Omega_m = 0.315$, $\Omega_\Lambda = 0.685$, and $H_0 = 67.4$ km s^{-1} Mpc^{-1} (Planck Collaboration et al. 2020).

2. Sample Selection

The SALT-NOT sample definition is based on the requirements of MALS. MALS is using MeerKAT's L and UHF bands covering 900–1670 and 580–1015 MHz to carry out a sensitive search for H I 21 cm (OH 18 cm) absorbers at $0 \leqslant z \lesssim 0.6$ ($0 \leqslant z \lesssim 0.9$) and $0.4 \lesssim z \lesssim 1.4$ ($0.6 \lesssim z \lesssim 1.9$), respectively (see Gupta et al. 2016 for key scientific objectives). In order to ensure reasonable observability with the MeerKAT telescope located in South Africa, the majority of MALS pointings will be at $\delta < +20°$. The survey is well underway and the first L- and UHF-band spectra based on the scientific verification data are presented in Gupta et al. (2021a) and Combes et al. (2021), respectively.

Each MALS pointing is centered at a radio source brighter than 200 mJy at ∼1 GHz. For the L band we require these bright AGN to be at $z > 0.6$, whereas for the UHF band all must be at $z > 0.4$ and a significant fraction at $z > 1.4$, i.e., the H I 21 cm line redshift corresponding to the lower frequency edge of the band.

Since dust bias can be very significant toward sight lines with cold atomic and molecular gas, it is also desirable that the central targets for MALS are selected without any bias toward dust extinction. Thus, to efficiently identify quasars that can be used for both the L and UHF bands we have developed a selection scheme optimized to identify $z > 1.4$ quasars based primarily on MIR colors from the AllWISE catalog. The WISE color space of radio sources identified as quasars in the Sloan Digital Sky Survey (SDSS) spectroscopic catalog is presented in Figure 2 of Krogager et al. (2018). This figure shows that low- and high-z quasars are separated in W1, W2, and W3 color space, and the following color cuts:

$$\mathrm{W1} - \mathrm{W2} < 1.3 \times (\mathrm{W2} - \mathrm{W3}) - 3.04;$$
$$\mathrm{W1} - \mathrm{W2} > 0.6 \qquad (1)$$

can be used to efficiently select high-z quasars.

To summarize, the SALT-NOT sample is based on the following three criteria: (i) flux density >200 mJy at ∼1 GHz, (ii) $\delta < +20°$, and (iii) MIR colors consistent with Equation (1). The last condition requires that the object is detected in the first three WISE bands. Note that only ∼10% of 747 million objects are detected in all three bands. We revisit the efficacy of the MIR color selection scheme in subsequent sections.

2.1. Crossmatching and Reference Sample

Crossmatching multiwavelength data sets poses multiple challenges. First, not all objects may be detected in all the data sets. Second, due to different spatial resolutions of data sets, an object in one data set may have multiple counterparts in the other. This is particularly relevant for radio sources, which often display extended emission made up of components such as core, jets, and lobes. Depending on the frequency the strongest radio component may be far away from the optical or IR counterpart. For reliable crossmatching it is desirable to have radio data with a spatial resolution of few arcseconds or better.

Another major challenge is that each selection method has its own systematics. For quasars, it is quite possible that selections using different methods may lead to objects with different characteristics such as different Eddington ratios, clustering properties, and host galaxy masses. The selected quasars may then be intrinsically different, therefore comparison with samples from other selection approaches ought to be done with caution.

Concerning our sample definition, only[16] the NVSS (Condon et al. 1998) and the Sydney University Molonglo Sky Survey (SUMSS; Mauch et al. 2003) at 1.4 GHz and 0.843 GHz, respectively, have the sensitivity, positional accuracy, and the sky coverage required to perform crossmatching with the AllWISE catalog (Cutri et al. 2014) at MIR wavelengths. But the spatial resolution offered by NVSS is typically 45″. In comparison, the angular resolutions in the four WISE bands are 6.″1, 6.″4, 6.″5, and 12.″0, respectively. The coarse resolution at radio wavelength might then lead to a bias against extended lobe-dominated quasars: either they will be assigned a wrong WISE counterpart or completely missed. To quantify the impact of this and the other abovementioned challenges in our selection process, we start with constructing a *reference* sample.

The process of building the reference sample is shown in Figure 1. We start with NVSS, which has 25,325 radio sources brighter than 200 mJy at 1.4 GHz and $\delta > -40°$. We use optical data from SDSS and higher spatial resolution (i.e ∼5″) radio data from the Faint Images of the Radio Sky at Twenty centimeters (FIRST; Becker et al. 1995) to examine our selection process. The FIRST survey has observed ∼10,000 deg^2 of the North and South Galactic Caps at 1.4 GHz, which overlaps very well with the SDSS sky coverage. These two surveys provide the best available radio-optical data covering a large area of the sky. Since the bulk of FIRST-SDSS coverage is at positive decl., we do not apply any decl. cuts to the reference sample.

We crossmatch 10,279 NVSS sources, which are within the SDSS footprint with FIRST. We adopt a search radius of 30″. Since FIRST has a spatial resolution of 5″ and positional accuracy of 0.″1, it will allow us to identify the resolved radio source components associated with the NVSS sources. Next, we crossmatch FIRST radio source components with SDSS (DR14 photometry) and AllWISE catalogs to identify the closest match. Note that we require a valid WISE match to have detections in all three bands, i.e., W1, W2, and W3. For this we adopt a search radius of 2″, which has been shown to provide a good compromise between completeness and random association for FIRST-SDSS quasars (e.g., Lu et al. 2007). We visually examined all 2327 FIRST-SDSS associations using the FIRST and SDSS i-band images, and excluded: (i) eight unreal radio source components: these are due to an artifact in the FIRST image; and (ii) 12 radio sources with complex morphology: for these it is not possible to reliably assign an optical-MIR counterpart to the radio source. Spectra of 1164 sources are available in SDSS. We inspect these and reject 13 cases with false spectral line identifications. Finally, we have a reference sample of 2294 sources from NVSS, with WISE detections in the W1, W2, and W3 bands, and crossmatching further refined by FIRST and SDSS.

The WISE colors of the reference sample are shown in the left panel of Figure 2. Among 1151 reference sample sources with SDSS spectra, 834 are identified as quasars and 317 as galaxies. Clearly, as expected the majority of radio-bright quasars have red W1-W2 colors. Only beyond $z \sim 3$, the rest-frame 1 μm minimum would shift into the W2 band causing the color to turn blue (see Stern et al. 2012). But for high-z quasars this can be compensated by even small amounts of dust, allowing the method based only on W1-W2 color to perform rather well even at high redshifts. However, significant host galaxy contribution can also turn W1-W2 blue. In the figure, we show the color wedge of Mateos et al. (2012) defined based on X-ray selected AGN. The additional constraint based on W2-W3 allows the wedge of (Mateos et al. 2012, also see their Figure 5) to efficiently identify AGN as long as the host galaxy contribution is less than 20%. Indeed, the wedge efficiently identifies the bulk of powerful reference quasars.

---

[16] The Rapid ASKAP Continuum Survey (McConnell et al. 2020) was unavailable at the time of planning this project.

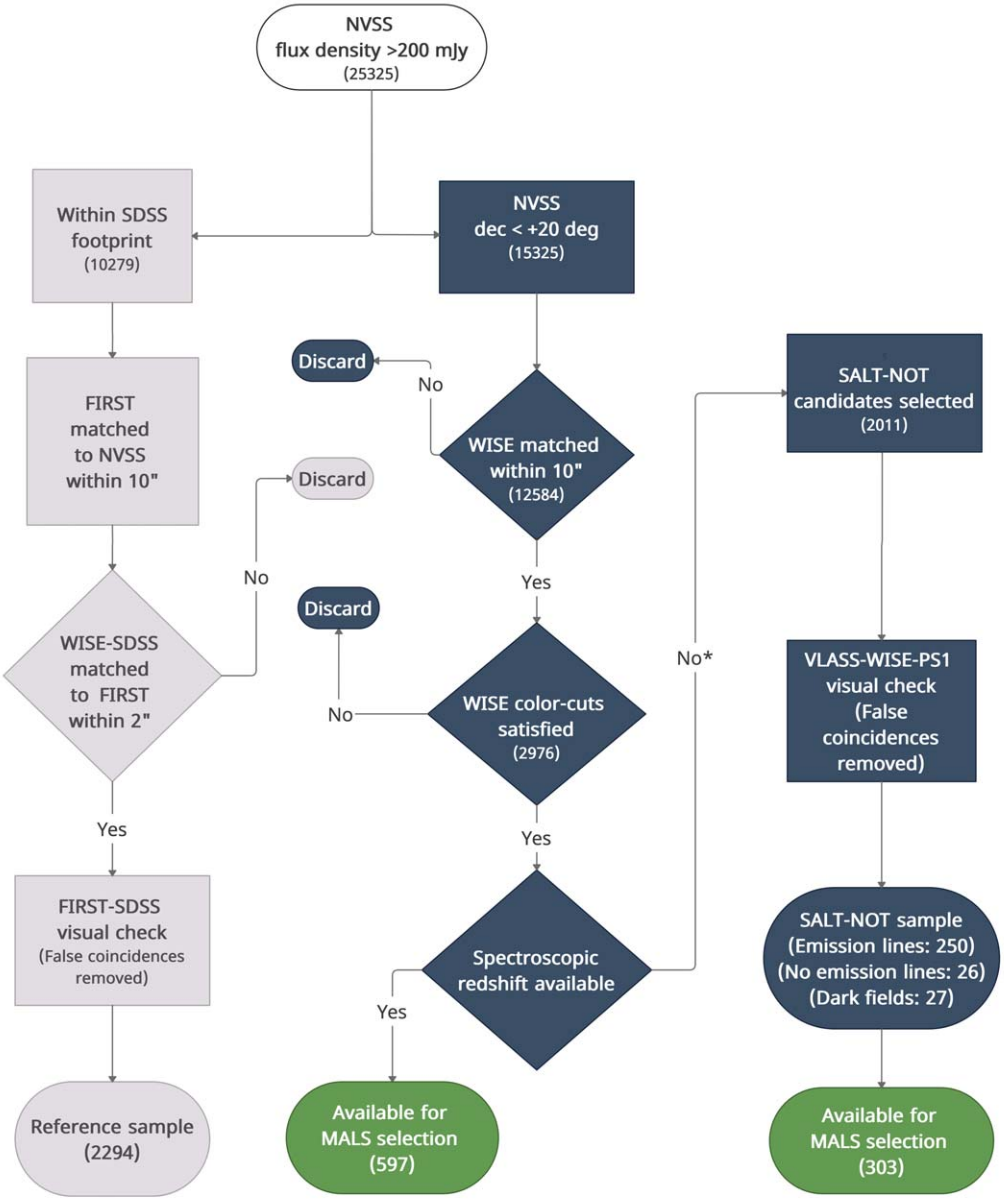

Figure 1. Schematic illustration of the selection process for the quasar reference sample and SALT-NOT targets. The numbers refer to sources at each step. The “$\star$” indicates that a handful of targets with spectra in SDSS were included in the SALT-NOT survey to verify our selection and observational strategy. See Section 4 for more details.

In Figure 2, we also demarcate the region corresponding to Equation (1). The redshift and i-band magnitude distributions of the reference sample are shown in the right panels of Figure 2. The median redshift and i-band magnitude are 0.9 and 18.6 mag, respectively. If we consider only quasars, these values are 1.3 and 18.6 mag, respectively. For quasars within our MIR wedge, these values are 2.0 and 19.1 mag, respectively (see vertical dashed lines in Figure 2). Also, within the wedge the fraction of AGN classified as quasars increases to $94 \pm 6\%$ (214/228), whereas for the full sample it is $73 \pm 3\%$ (834/1151). The fraction of $z > 1.4$ quasars also increases from 30% (full sample) to 75% (within the wedge). Thus, our MIR wedge preferentially selects more powerful and higher redshift quasars.

2.2. SALT-NOT Candidate Sample

The process of identifying candidates for SALT-NOT survey is shown in Figure 1. We start with 25,325 sources brighter than 200 mJy in NVSS but first restrict ourselves to 15,325 at $\delta < +20°$ and then to 12,584 with WISE matches within 10″. Since we use NVSS all the candidates are at $\delta > -40°$. Next we consider only 2976 sources that satisfy our WISE color cuts. Of these, 597 sources ($\sim$340 at $z > 1.4$) have spectroscopic redshifts from the literature,[17] and will be used later for MALS target selection (see Section 6). For the SALT-NOT survey, we exclude these and consider the remaining 2011 radio sources which have a high probability of being a quasar at $z > 1.4$.

Next, targets were drawn from the pool of 2011 candidates to fill the allocated and observable local sidereal time ranges at the NOT and SALT locations. The final sample of 303 candidates that could be observed in the allocated time is presented in Table 1. The sample has been subjected to visual checks using the quick look radio images at 2–4 GHz from the Very Large

---

[17] NASA/IPAC Extragalactic Database (NED) and the Million Quasars (Milliquas) Catalog v4.0.

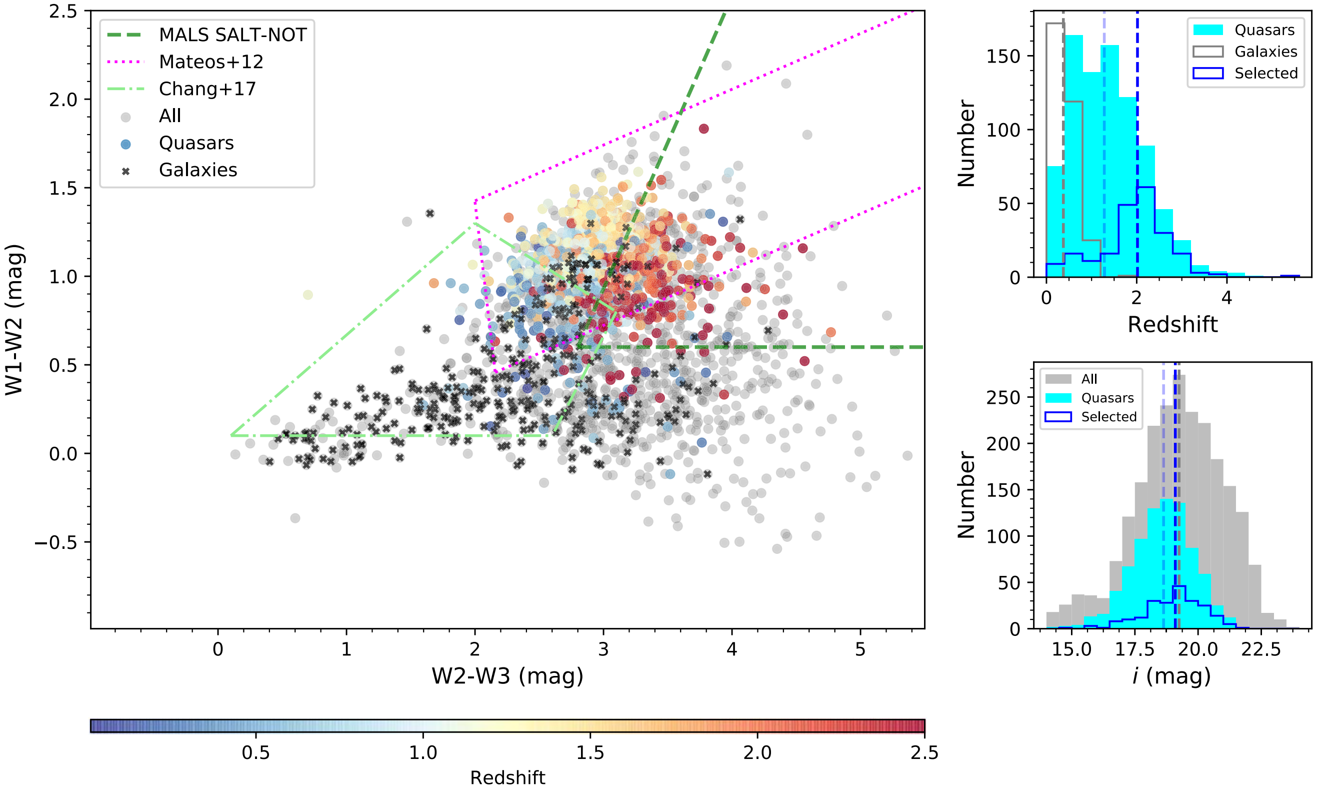

Figure 2. Left: WISE color–color plot in Vega magnitudes for radio-bright sources in the quasar reference sample. Sources with known spectroscopic redshifts are color coded according to redshift. The AGN wedges of Mateos et al. (2012), Chang et al. (2017), and our SALT-NOT criteria are shown using dotted, dashed–dotted, and dashed lines, respectively. Right, top panel: redshift distributions of quasars, galaxies, and WISE-selected quasars (i.e., quasars satisfying SALT-NOT WISE color cuts). Right, bottom panel: distributions of SDSS i-band AB magnitude for all sources, quasars, and WISE-selected quasars are shown. The vertical dashed lines indicate the median for each distribution. Note that SDSS 5σ depth for the i band is 22.2 mag.

Array Sky Survey (VLASS; Lacy et al. 2020). These quick look images have a spatial resolution of $\sim 2\farcs5$ but are not the final data products meeting the overall survey requirements. The positional accuracy is limited to $\sim 0\farcs5$. Therefore, we used these images only to verify the coincidence between the MIR source and the radio peak. In the cases where a VLASS image was unavailable or not of reasonable quality, the corresponding candidate was assigned a lower priority. Following the process described in Section 2.1, we rejected dubious coincidences, which primarily meant rejecting sources with complex radio morphologies. It was straightforward to verify and accept the compact radio sources (i.e., single component in VLASS), and indeed our overall selection process preferentially picks quasars associated with compact radio emission. But wherever possible we also included targets with clear core-jet or compact symmetric object type morphology. In both these cases it is possible to identify the location of MIR/optical AGN. The details of radio structure of AGN observed with SALT-NOT are presented in Section 5.

For candidates at $\delta > -30°$, we have also examined the i-band images from the Panoramic Survey Telescope and Rapid Response System (Chambers et al. 2016) by considering the nearest match within 2″. Ideally, in the pursuit of dust-obscured quasars one does not include any criteria based on optical wavelengths. Therefore, we limited the majority of our targets to those that could be successfully observed with SALT and NOT in a modest amount of observing time but included a small (∼10%) fraction with very faint ($i > 22$ mag) optical counterparts. Note that in Table 1 we excluded seven targets (list provided in the notes to Table 1) from the NOT sample presented in Table 1 of Krogager et al. (2018). The VLASS-WISE-PS1 visual check revealed that the lack of spectroscopic outcome in these cases is due to the misidentification of the optical/IR source associated with the radio source. Such misidentifactions have already been removed from the sample for the SALT component.

The sample presented in Table 1 is split into three categories: (i) with emission lines in the optical spectrum (250 objects), (ii) with no emission lines in the optical spectrum i.e., emission line less (ELLs; 26), and (iii) dark fields (DFs; 27), i.e., neither emission line nor a continuum source in optical spectra and images, respectively, despite being detected in WISE images. The distributions of 1.4 GHz flux density, W1- and i-band magnitudes are shown in Figure 3. Further details and comparison with the reference sample are provided in subsequent sections.

2.3. *Efficacy of Selection Process*

As previously mentioned, our target selection process is optimized for identifying powerful quasars at $z > 1.4$. We have therefore included a set of criteria on the WISE photometry (see Equation (1)). The mere fact that we require detections in all three WISE bands might introduce a bias in the resulting quasar sample, and the subsequent color criteria might further affect their optical properties. In this section, we aim to quantify any such selection effects.

Table 1

Sample of Radio Sources for the uGMRT Survey

NVSS ID	Flux	$B_{\rm maj}$	$B_{\rm min}$	$B_{\rm pa}$	Redshift	Telescope	AGN-type						
	WISE ID	R.A.$_W$	Decl.$_W$	W1	δW1	W2	δW2	W3	δW3				
	PS1 ID	nStackDets	nDetections	g	δg	r	δr	i	δi	z	δz	y	δy
(1)	(2)	(3)	(4)	(5)	(6)	(7)	(8)						
	(9)	(10)	(11)	(12)	(13)	(14)	(15)	(16)	(17)				
	(18)	(19)	(20)	(21)	(22)	(23)	(24)	(25)	(26)	(27)	(28)	(29)	(30)
Spectra with emission lines (250)													
M000234.52-052324.5	235.4	<16.7	<15.9	⋯	0.306	SALT	G						
	J000234.55-052324.0	0.6439997	−5.3900227	15	0.04	14.18	0.05	10.96	0.14				
	PSO J000.6440-05.3900	5	77	21.26	0.08	20.31	0.02	19.95	0.02	19.18	0.03	19.23	0.05
M000920.42-074057.5	269.9	<18.8	<16.7	⋯	1.672	SALT	Q						
	J000920.43-074057.3	2.3351346	−7.6826025	16.26	0.07	15.07	0.09	11.65	0.25				
	PSO J002.3351-07.6826	5	76	20.16	0.02	19.97	0.02	19.47	0.03	19.6	0.02	19.43	0.03
M000923.07-282153.9	205.8	<19.0	<18.0	⋯	1.796	SALT	Q						
	J000923.18-282152.0	2.3466024	−28.3644449	15.77	0.05	14.51	0.06	11.19	0.15				
	PSO J002.3465-28.3645	10	65	20.02	0.02	19.34	0.02	18.92	0.01	19.19	0.04	19.23	0.05
M001508.49+082803.8*b	384	<18.6	<17.4	⋯	1.710	SALT	Q						
	J001508.62+082802.2	3.7859185	8.4672841	15.06	0.04	14.26	0.05	10.95	0.14				
	PSO J003.7858+08.4674	5	49	19.46	0.02	19.02	0.04	18.67	0.02	18.71	0.01	18.42	0.02
M001708.03-125624.9	929.7	<17.1	<16.1	⋯	0.883	SUGAR	G						
	J001708.22-125625.5	4.2842556	−12.9404436	14.16	0.03	12.96	0.03	9.51	0.05				
	PSO J004.2842-12.9405	5	74	20.46	0.04	19.68	0.02	19.25	0.02	18.87	0.02	18.1	0.03
M002355.84-235717.8*b	211	<17.6	<16.3	⋯	1.442	SALT	Q						
	J002355.79-235719.3	5.9824792	−23.9553806	16.32	0.07	15.41	0.10	12.04	0.31				
	PSO J005.9820-23.9555	5	44	21.82	0.1	21.13	0.05	20.79	0.04	20.91	0.15	20.17	0.18
M002546.66-124725.2	394.4	<17.2	<15.3	⋯	0.770	SALT	Q						
	J002546.68-124724.9	6.444512	−12.7902504	15.85	0.05	15.21	0.10	11.77	⋯				
	PSO J006.4444-12.7904	8	22	−999	−999	21.64	0.09	21.25	0.07	20.72	0.08	−999	−999
M004243.06+124657.6	635	<18.3	<16.2	⋯	2.150	NOT	Q						
	J004243.02+124657.2	10.6792742	12.7825612	15.78	0.05	14.54	0.07	11.13	0.17				
	PSO J010.6793+12.7826	10	68	20.12	0.03	19.95	0.04	19.54	0.02	19.41	0.04	19.28	0.06
M005315.65-070233.4	248.2	<17.7	<14.8	⋯	2.130	NOT	Q						
	J005315.67-070232.5	13.3153062	−7.0423807	16.31	0.07	15.25	0.10	11.95	0.3				
	PSO J013.3154-07.0424	5	65	20.83	0.03	20.28	0.02	20.01	0.01	19.71	0.04	19.53	0.09
M010329.05+052131.2	589.1	<16.0	<15.6	⋯	1.421	SALT	Q						
	J010329.05+052132.4	15.871081	5.3590232	16.7	0.09	15.57	0.12	11.79	⋯				
	PSO J015.8710+05.3588	5	74	20.87	0.04	20.68	0.06	20.14	0.02	19.99	0.03	19.89	0.12
M010628.74-343409.0	259.8	<18.2	<16.0	⋯	0.116	SALT	G						
	J010628.71-343410.5	16.6196616	−34.5695834	13.66	0.03	12.96	0.03	9.07	0.03				
M011727.84-042511.5	421.4	<19.2	<16.8	⋯	1.720	NOT	Q						
	J011727.86-042510.4	19.3661239	−4.4195713	16.05	0.06	15	0.08	11.71	0.24				
	PSO J019.3661-04.4196	5	66	20.3	0.04	20.67	0.05	19.27	0.03	19.9	0.05	19.64	0.18
M013047.38-172505.6	250.3	<17.5	<16.1	⋯	2.528	SALT	Q						
	J013047.31-172506.2	22.697147	−17.4183991	16.71	0.1	16.01	0.18	12.09	⋯				
	PSO J022.6972-17.418	5	42	20.49	0.04	20.35	0.03	20.36	0.03	20.24	0.05	20.24	0.15
M013212.20-065236.8*c	1258.9	<18.3	<16.2	⋯	1.511	SALT	Q						
	J013212.24-065236.0	23.0510009	−6.8766872	15.95	0.05	14.73	0.06	11.32	0.16				
M013355.99-025635.2	270.2	<19.2	<16.9	⋯	0.261	SALT	G						
	J013355.91-025633.3	23.4829682	−2.9426108	13.58	0.03	12.67	0.03	9.56	0.04				
	PSO J023.4830-02.9426	5	73	18.96	0.03	18.28	0.02	18.26	0.01	17.9	0.02	17.9	0.02
M013721.79+072059.0	314.8	44.7	<18.4	3.3	0.255	SALT	G						
	J013721.81+072058.0	24.3408858	7.3494561	14.35	0.03	13.29	0.03	10.03	0.05				
	PSO J024.3406+07.3495	0	7	−999	−999	−999	−999	19.87	0.14	19.36	0.07	−999	−999

Table 1
(Continued)

NVSS ID	Flux	$B_{\rm maj}$	$B_{\rm min}$	$B_{\rm pa}$	Redshift	Telescope	AGN-type						
	WISE ID	R.A.$_W$	Decl.$_W$	W1	δW1	W2	δW2	W3	δW3				
	PS1 ID	nStackDets	nDetections	g	δg	r	δr	i	δi	z	δz	y	δy
(1)	(2)	(3)	(4)	(5)	(6)	(7)	(8)						
	(9)	(10)	(11)	(12)	(13)	(14)	(15)	(16)	(17)				
	(18)	(19)	(20)	(21)	(22)	(23)	(24)	(25)	(26)	(27)	(28)	(29)	(30)
M015647.53-361608.3	1296.9	<16.6	<16.4	⋯	0.354	SALT	G						
	J015647.59-361610.1	29.1983255	−36.2694836	14.76	0.03	13.49	0.03	10.14	0.06				
J021148.77+170723.2	539.8	<19.3	<17.9	⋯	1.980	NOT	Q						
	J021148.78+170722.6	32.9532841	17.1229521	16.22	0.06	15.42	0.10	11.82	0.24				
	PSO J032.9532+17.1230	5	45	20.24	0.07	20.12	0.03	19.88	0.02	19.64	0.03	19.61	0.04
M021231.86-382256.6	244.5	<18.6	<16.4	⋯	2.260	SALT	Q						
	J021231.72-382256.9	33.1321971	−38.382499	17.16	0.09	16.33	0.15	12.32	⋯				
M021650.70+172404.9	395.2	<17.5	<17.2	⋯	1.530	NOT	Q						
	J021650.74+172405.7	34.2114448	17.4016026	15.99	0.06	15.09	0.10	11.91	0.36				
	PSO J034.2114+17.401	5	54	20.73	0.05	20.16	0.04	19.8	0.04	19.89	0.03	19.64	0.09
M021715.31-271555.4	265.1	<18.7	<15.3	⋯	1.950	SALT	Q						
	J021715.33-271555.4	34.3138823	−27.265405	16.7	0.07	15.54	0.09	12.09	0.24				
	PSO J034.3138-27.2654	5	62	19.91	0.01	19.84	0.02	19.61	0.01	19.44	0.02	19.41	0.05
M022128.93-335827.0	219.8	<17.9	<16.0	⋯	0.524	SALT	Q						
	J022128.90-335826.8	35.3704341	−33.9741367	15.67	0.04	14.29	0.05	10.33	0.07				
M022613.72+093726.3	374.6	<17.1	<16.4	⋯	2.605	SUGAR	Q						
	J022613.71+093726.7	36.5571491	9.6240874	15.03	0.04	14.11	0.05	10.74	0.1				
	PSO J036.5571+09.6241	5	55	18.33	0.01	18.01	0.01	17.89	0.02	17.8	0.01	17.69	0.02
M022639.92+194110.1	209.8	<15.9	<14.0	⋯	2.190	NOT	Q						
	J022639.93+194110.5	36.6663794	19.686268	16.52	0.09	15.46	0.12	11.9	⋯				
	PSO J036.6665+19.6862	5	69	20.46	0.02	20.36	0.02	20.06	0.02	19.74	0.02	19.74	0.03
M022924.85-243600.9*b	276.7	14.1	<17.6	68.1	2.003	SALT	Q						
	J022924.93-243600.9	37.3538803	−24.6002552	16.04	0.05	15.28	0.07	12.21	0.24				
	PSO J037.3539-24.6003	5	11	−999	−999	−999	−999	21.61	0.04	−999	−999	20.24	0.18
M023939.11-135409.4	214	<18.3	<16.6	⋯	1.947	SALT	Q						
	J023939.14-135409.5	39.9131075	−13.9026396	16.04	0.05	14.95	0.06	11.66	0.17				
	PSO J039.9130-13.9026	5	44	19.66	0.02	19.55	0.02	19.38	0.02	19.27	0.03	19.25	0.09
M024027.19+095713.0	521.2	14.7	<19.0	−50.1	1.874	SALT	Q						
	J024027.16+095713.4	40.113197	9.9537378	16.36	0.07	15.49	0.12	12.43	0.45				
	PSO J040.1135+09.9537	5	44	21.01	0.05	20.98	0.04	20.48	0.05	20.27	0.05	−999	−999
M024046.80+083258.3	305.4	<19.6	<16.4	⋯	1.100	NOT	Q						
	J024046.81+083259.9	40.1950492	8.5499839	15.57	0.04	14.59	0.06	11.49	0.21				
	PSO J040.1951+08.5500	5	61	19.74	0.02	19.41	0.01	19.2	0.01	19.11	0.01	18.9	0.03
M024106.56-171640.3	453.9	<17.7	<16.6	⋯	0.365	SALT	G						
	J024106.57-171641.5	40.2774033	−17.2782204	15.26	0.04	14.64	0.05	11.81	0.25				
	PSO J040.2774-17.2782	5	81	21.03	0.07	19.88	0.02	19.62	0.02	19.15	0.03	19.18	0.04
M024939.93+044028.9	420.5	<17.0	<16.2	⋯	2.008	SUGAR	Q						
	J024939.97+044028.3	42.4165498	4.6745332	16.15	0.06	15.10	0.07	11.68	0.19				
	PSO J042.4165+04.6745	5	60	20.61	0.03	20.32	0.06	19.88	0.01	19.61	0.02	19.48	0.09
M025035.54-262743.1	389.2	<16.6	<15.3	⋯	2.918	SALT	Q						
	J025035.56-262742.4	42.6481981	−26.4617931	16.08	0.05	15.06	0.07	11.63	0.16				
	PSO J042.6482-26.4618	5	78	19.1	0.01	18.97	0.02	18.9	0.02	18.98	0.01	18.89	0.03
M025630.36-021844.5	260.3	<17.3	<15.6	⋯	1.970	NOT	Q						
	J025630.37-021844.2	44.1265641	−2.312278	15.21	0.03	13.88	0.04	10.27	0.06				
	PSO J044.1266-02.3123	5	72	18.85	0.03	18.63	0.01	18.46	0.01	18.25	0.01	18.32	0.01
M030032.15-302243.8	371.4	<16.6	<15.4	⋯	0.310	SALT	G						
	J030032.19-302242.4	45.1341357	−30.37846	14.66	0.03	13.8	0.03	10.26	0.05				

Table 1
(Continued)

NVSS ID	Flux	$B_{\rm maj}$	$B_{\rm min}$	$B_{\rm pa}$	Redshift	Telescope	AGN-type						
	WISE ID	R.A.$_W$	Decl.$_W$	W1	δW1	W2	δW2	W3	δW3				
	PS1 ID	nStackDets	nDetections	g	δg	r	δr	i	δi	z	δz	y	δy
(1)	(2)	(3)	(4)	(5)	(6)	(7)	(8)						
	(9)	(10)	(11)	(12)	(13)	(14)	(15)	(16)	(17)				
	(18)	(19)	(20)	(21)	(22)	(23)	(24)	(25)	(26)	(27)	(28)	(29)	(30)
M030413.80-112653.5	335	<16.6	<15.3	···	1.552	SUGAR	Q						
	J030413.74-112653.3	46.0572895	−11.4481531	16.98	0.09	15.84	0.12	12.34	···				
	PSO J046.0574-11.4480	5	82	20.33	0.02	20.02	0.03	19.76	0.04	19.93	0.03	19.74	0.11
M031022.90+055552.6	200.5	21.2	<17.8	52.5	0.399	SALT	G						
	J031023.01+055552.4	47.5958935	5.9312433	15.12	0.03	13.89	0.04	10.27	0.08				
	PSO J047.5959+05.9313	5	49	−999	−999	21.17	0.07	20.35	0.03	20.12	0.04	19.63	0.06
M031407.94-090946.9	226.8	44.5	<18.7	84.1	0.312	NOT	G						
	J031407.90-090948.5	48.532931	−9.1634772	15.25	0.04	14.61	0.05	11.72	0.24				
	PSO J048.5329-09.1635	10	64	21.38	0.07	20.1	0.02	19.67	0.04	19.51	0.03	19.16	0.04
M031551.28-364450.8	462.4	<19.6	<15.6	···	1.348	SALT	Q						
	J031551.34-364448.9	48.9639505	−36.7469393	15.8	0.04	14.84	0.05	11.74	0.17				
M031706.76+065550.3	247.9	23.9	<17.2	70.8	0.275	NOT	G						
	J031706.74+065549.6	49.2781024	6.9304589	14.78	0.03	14.12	0.05	11.13	0.16				
	PSO J049.2781+06.9305	5	61	21.41	0.08	20	0.04	19.46	0.02	18.95	0.04	18.83	0.04
M032128.78-294047.4*d	2061.7	<16.5	<15.6	···	0.583	SALT	Q						
	J032128.80-294046.3	50.3700396	−29.6795529	13.97	0.03	12.85	0.03	9.57	0.03				
	PSO J050.3701-29.6796	5	50	20.68	0.02	19.96	0.03	18.98	0.02	19.32	0.02	18.83	0.03
M032808.59-015220.2	221.9	<18.3	<15.9	···	2.679	SUGAR	Q						
	J032808.68-015221.0	52.0361812	−1.8725096	15.46	0.04	14.55	0.06	11.31	0.17				
	PSO J052.0363-01.8726	5	76	18.7	0.01	18.53	0.02	18.48	0.02	18.36	0.01	18.33	0.03
M034157.75+151925.5	200.4	<17.5	<15.1	···	1.699	NOT	Q						
	J034157.69+151925.0	55.4903908	15.3236243	16.32	0.08	15.22	0.09	11.77	···				
	PSO J055.4904+15.3235	5	60	20.87	0.05	20.58	0.04	20.18	0.05	20.04	0.03	19.85	0.09
M035016.86-035111.3	230.5	<17.5	<15.3	···	0.611	SUGAR	Q						
	J035016.85-035111.3	57.5702271	−3.8531559	15.21	0.04	14	0.04	10.65	0.1				
	PSO J057.5702-03.8532	5	75	19.25	0.02	19.06	0.02	18.81	0.01	18.86	0.02	18.79	0.05
M035211.06-251449.8	269.3	<17.0	<16.4	···	1.675	SALT	Q						
	J035211.06-251450.2	58.0460983	−25.2473	14.77	0.03	13.68	0.03	10.12	0.06				
	PSO J058.0461-25.2473	5	73	19.52	0.02	19.32	0.03	19.04	0.01	18.97	0.02	18.79	0.05
M035414.70-030804.3	725.6	<18.7	<18.1	···	0.442	SALT	G						
	J035414.72-030804.8	58.5613708	−3.1346696	14.79	0.03	13.98	0.04	10.82	0.13				
	PSO J058.5614-03.1348	5	58	20.58	0.03	19.87	0.02	19.18	0.01	19.17	0.03	18.54	0.02
M035633.46+190034.6	1051.3	<17.7	<17.0	···	1.480	NOT	Q						
	J035633.48+190034.3	59.1395029	19.0095492	15.76	0.05	14.95	0.08	11.73	0.32				
	PSO J059.1394+19.0090	3	31	−999	−999	−999	−999	20.64	0.02	19.9	0.03	19.42	0.05
M035634.55-083121.3	239.7	<18.3	<16.8	···	1.447	NOT	Q						
	J035634.52-083122.3	59.1438555	−8.522875	16.52	0.08	15.34	0.10	11.84	···				
	PSO J059.1439-08.5229	5	60	21.15	0.04	20.47	0.03	20.23	0.02	20.24	0.05	20.22	0.05
M040015.06-142328.0*c	409.7	<19.1	<15.8	···	1.136	SALT	Q						
	J040015.04-142328.2	60.0626992	−14.391167	15.81	0.05	15.16	0.08	12.11	0.33				
	PSO J060.0627-14.3911	10	73	19.38	0.01	19.14	0.01	19.22	0.01	19.07	0.02	18.96	0.04
M041530.42-234750.2	262	<17.4	<16.0	···	0.366	SALT	G						
	J041530.38-234751.3	63.8765933	−23.7975834	15.59	0.04	14.8	0.06	11.61	0.19				
	PSO J063.8767-23.7975	5	65	20.74	0.02	19.63	0.01	19.53	0.02	19.11	0.02	19.15	0.1
M041620.54-333931.3	264.1	<20.0	<15.8	···	3.045	SALT	Q						
	J041620.47-333931.6	64.0853255	−33.6587934	16.08	0.05	15.19	0.08	11.66	0.19				

Table 1

(Continued)

NVSS ID	Flux	$B_{\rm maj}$	$B_{\rm min}$	$B_{\rm pa}$	Redshift	Telescope	AGN-type						
	WISE ID	R.A.$_W$	Decl.$_W$	W1	δW1	W2	δW2	W3	δW3				
	PS1 ID	nStackDets	nDetections	g	δg	r	δr	i	δi	z	δz	y	δy
(1)	(2)	(3)	(4)	(5)	(6)	(7)	(8)						
	(9)	(10)	(11)	(12)	(13)	(14)	(15)	(16)	(17)				
	(18)	(19)	(20)	(21)	(22)	(23)	(24)	(25)	(26)	(27)	(28)	(29)	(30)
M042248.53-203456.6	224.3	<17.2	<16.7	···	2.582	SALT	Q						
	J042248.43-203455.8	65.7017923	−20.5821781	16.73	0.08	15.96	0.14	12.09	···				
	PSO J065.7019-20.5822	5	60	20.84	0.04	20.46	0.05	20.52	0.03	20.45	0.09	19.42	0.16
M042725.05+085330.3*c	937.7	<13.9	<13.9	···	1.215	SALT	Q						
	J042725.11+085329.9	66.8546587	8.8916425	15.91	0.06	14.9	0.08	11.64	0.27				
	PSO J066.8546+08.8916	5	52	20.79	0.08	20.13	0.04	19.75	0.03	19.5	0.08	19.46	0.05
M044604.72-114813.4	273.8	<17.7	<15.8	···	1.668	SALT	Q						
	J044604.67-114812.8	71.5194971	−11.8035664	15.12	0.03	14.28	0.04	11.08	0.12				
	PSO J071.5196-11.8035	5	82	18.78	0.01	18.52	0.01	18.22	0.01	18.16	0.01	18.16	0.02
M044849.48-093531.3	240.9	<17.9	<15.5	···	2.079	SALT	Q						
	J044849.47-093531.4	72.2061409	−9.5920798	14.57	0.03	13.64	0.03	10.27	0.08				
	PSO J072.2061-09.5921	10	76	18.3	0	17.88	0.01	17.59	0	17.43	0.01	17.41	0.02
M045541.91+185010.9	328.1	<16.3	<14.5	···	0.548	NOT	Q						
	J045541.81+185009.1	73.9242412	18.8358874	14.61	0.04	13.86	0.04	10.79	0.11				
	PSO J073.9245+18.8359	5	92	20.21	0.04	19.69	0.01	19.06	0.01	18.93	0.02	18.32	0.02
M050725.04-362442.9	212.4	<17.1	<14.7	···	2.930	SALT	Q						
	J050725.06-362443.1	76.8544416	−36.4119939	15.66	0.04	14.63	0.04	11.14	0.09				
M051024.23-195950.3	336.2	15.2	<16.6	89.5	0.472	NOT	G						
	J051024.07-195949.9	77.6003298	−19.9971964	14.95	0.03	14.15	0.04	11.16	0.12				
	PSO J077.6003-19.9972	10	65	20.61	0.12	20.31	0.03	19.76	0.04	19.69	0.04	19.22	0.04
M051134.05+024416.0	351.4	<18.3	<17.1	···	1.366	SALT	Q						
	J051134.13+024416.5	77.8922114	2.7379244	16.3	0.07	15.31	0.09	12.16	0.37				
	PSO J077.8921+02.7377	5	33	21.74	0.15	21.17	0.03	21.23	0.04	20.9	0	−999	−999
M051240.99+151723.8	966.5	<17.1	<15.3	···	2.568	NOT	Q						
	J051241.02+151723.4	78.1709541	15.289858	15.53	0.05	14.45	0.06	10.99	0.19				
	PSO J078.1709+15.2899	5	78	20.3	0.06	19.75	0.06	19.62	0.05	19.11	0.02	18.86	0.05
M051340.03+010023.6	447	<19.0	<17.0	···	2.673	SALT	Q						
	J051340.03+010021.7	78.4168243	1.0060487	15.73	0.05	14.88	0.07	11.56	0.27				
	PSO J078.4168+01.0060	10	87	19.14	0.01	18.83	0.01	18.8	0.02	18.71	0.01	18.54	0.02
M051511.18-012002.4	288.8	<17.5	<15.7	···	2.287	SALT	Q						
	J051511.18-012001.9	78.7965932	−1.3338644	15.79	0.05	14.81	0.07	11.35	0.17				
	PSO J078.7965-01.3339	10	62	18.81	0.01	18.66	0	18.6	0.02	18.59	0.04	18.4	0.02
M051656.35+073252.7	231.7	<17.7	<16.4	···	2.594	SUGAR	G						
	J051656.28+073251.6	79.2345275	7.5476931	14.18	0.03	13.53	0.03	10.65	0.15				
	PSO J079.2343+07.5473	5	30	21.14	0.09	20.29	0.03	19.7	0.03	19.27	0.05	19.13	0.02
M052318.55-261409.6	1354.9	<18.9	<15.7	···	3.110	SALT	Q						
	J052318.50-261409.2	80.8270963	−26.2359125	14.65	0.03	13.91	0.04	10.79	0.09				
	PSO J080.8270-26.2360	10	90	18.83	0.01	18.71	0.01	18.63	0.01	18.46	0.01	18.14	0.02
M052744.71-121153.7	335.6	<17.7	<16.2	···	0.316	SALT	G						
	J052744.69-121153.9	81.936226	−12.1983095	15.4	0.04	14.66	0.06	11.72	0.24				
	PSO J081.9362-12.1983	5	64	21.24	0.04	20.12	0.03	19.75	0.02	19.29	0.03	19.24	0.04
M052905.55-112607.5	455.8	<17.8	<16.0	···	1.007	SUGAR	Q						
	J052905.51-112607.8	82.2729967	−11.4355102	14.99	0.04	14.3	0.05	11.3	0.14				
	PSO J082.2730-11.4355	5	61	20.3	0.07	19.71	0.06	19.52	0.02	19.33	0.02	19.06	0.04
M054518.09-261857.3	236.9	<19.3	<16.3	···	0.800	SALT	Q						
	J054518.01-261856.3	86.3250527	−26.3156623	15.71	0.04	14.81	0.06	11.73	0.23				
	PSO J086.3251-26.3156	5	53	19.69	0.06	19.52	0.04	19.6	0.03	19.51	0.06	19.47	0.08

Table 1
(Continued)

NVSS ID	Flux	$B_{\rm maj}$	$B_{\rm min}$	$B_{\rm pa}$	Redshift	Telescope	AGN-type						
	WISE ID	R.A.$_W$	Decl.$_W$	W1	δW1	W2	δW2	W3	δW3				
	PS1 ID	nStackDets	nDetections	g	δg	r	δr	i	δi	z	δz	y	δy
(1)	(2)	(3)	(4)	(5)	(6)	(7)	(8)						
	(9)	(10)	(11)	(12)	(13)	(14)	(15)	(16)	(17)				
	(18)	(19)	(20)	(21)	(22)	(23)	(24)	(25)	(26)	(27)	(28)	(29)	(30)
M055007.33+002731.5	208.7	<17.6	<17.0	⋯	0.279	SALT	G						
	J055007.28+002731.6	87.5303628	0.4587796	14.06	0.03	13.13	0.03	9.98	0.06				
	PSO J087.5304+00.4588	5	64	20.91	0.03	19.88	0.03	19.33	0.01	18.67	0.03	18.51	0.04
M055205.32-345956.6	280	<17.8	<15.4	⋯	1.777	SALT	G						
	J055205.47-345958.1	88.0227953	−34.9994984	17.78	0.18	16.28	0.16	12.62	0.47				
M060248.09-254602.2*d	555.3	<17.8	<15.0	⋯	0.602	SALT	Q						
	J060248.05-254602.6	90.7002434	−25.7673954	15.5	0.04	14.87	0.06	11.69	0.2				
	PSO J090.7002-25.7674	5	66	21.5	0.04	21.4	0.4	20.23	0.02	20.07	0.05	19.4	0.06
M060958.94+021727.1	201.5	<17.7	<17.0	⋯	0.174	SALT	G						
	J060958.97+021726.5	92.4957371	2.2907017	13.38	0.03	12.22	0.02	8.29	0.02				
	PSO J092.4957+02.2907	5	69	21.31	0.06	19.85	0.03	18.6	0.02	18.86	0.03	18.58	0.04
M061038.80-230145.6	360.2	<16.5	<16.0	⋯	2.829	SALT	Q						
	J061038.78-230145.7	92.6615979	−23.0293781	15.33	0.04	14.36	0.05	10.74	0.1				
	PSO J092.6616-23.0294	5	67	18.62	0.01	18.47	0	18.35	0	18.27	0.01	18.14	0.01
M061856.02-315835.2	346.1	<16.5	<15.7	⋯	2.134	SALT	Q						
	J061856.00-315835.0	94.7333346	−31.97639	15.76	0.04	14.75	0.05	11.25	0.1				
M063602.28-311312.5	262.1	<16.6	<14.3	⋯	2.654	SALT	Q						
	J063602.35-311311.8	99.0098305	−31.2199453	13.88	0.03	12.77	0.03	9.39	0.03				
M063613.53-310646.3	208	<17.7	<15.4	⋯	2.757	SALT	Q						
	J063613.49-310644.1	99.0562279	−31.1122649	16.73	0.08	15.74	0.12	12.37	⋯				
M065254.73-323022.6	322.1	25.4	<17.7	−34.8	2.239	SALT	Q						
	J065254.55-323020.7	103.2273249	−32.5057682	14.86	0.03	14.08	0.04	10.9	0.1				
M070249.30-330205.0	314.6	<16.9	<15.8	⋯	2.410	SALT	Q						
	J070249.28-330204.2	105.7053378	−33.0345087	16.36	0.06	15.57	0.10	11.91	⋯				
M073159.01+143336.3	316.5	<17.9	<15.8	⋯	2.632	NOT	Q						
	J073158.97+143335.8	112.9957193	14.5599667	15.49	0.05	14.76	0.07	11.01	0.14				
	PSO J112.9958+14.5601	5	58	18.54	0.02	18.43	0.01	18.28	0.01	18.26	0.03	18.14	0.01
M073714.60-382841.9	219.3	14.2	<16.7	−17	2.107	SALT	Q						
	J073714.61-382839.3	114.3108811	−38.4776064	15.41	0.04	14.19	0.04	10.88	0.08				
M073748.06-381259.0	2436.5	18.2	<18.9	35.4	0.318	SALT	G						
	J073748.12-381257.6	114.4505408	−38.2160133	14.25	0.03	13.14	0.03	9.9	0.05				
M080217.91+080525.4	210.5	<18.3	<15.9	⋯	0.995	SALT	Q						
	J080217.84+080524.7	120.5743551	8.0902184	16.24	0.07	15.44	0.11	12.45	0.51				
	PSO J120.5743+08.0903	5	63	20.99	0.12	20.86	0.05	20.73	0.05	20.48	0.04	19.96	0.12
M080356.46+042102.8*c	318.1	<17.0	<16.4	⋯	1.252	SALT	Q						
	J080356.43+042102.6	120.9851521	4.3507431	15.27	0.04	14.14	0.04	10.86	0.11				
	PSO J120.9852+04.3508	5	76	19.22	0.02	18.94	0.02	18.87	0.01	18.88	0.02	18.9	0.03
M080804.34+005708.2	317	<17.2	<16.5	⋯	3.133	SALT	Q						
	J080804.34+005707.6	122.0181055	0.9521212	15.31	0.04	14.38	0.05	10.58	0.1				
	PSO J122.0181+00.9521	5	72	18.47	0.01	18.27	0.01	18.07	0	18.12	0.01	18.04	0.03
M081727.59-030737.7	502.7	<16.6	<15.4	⋯	1.785	SALT	Q						
	J081727.45-030737.2	124.3644078	−3.1270117	14.9	0.03	14.21	0.04	10.95	0.13				
	PSO J124.3645-03.1270	5	42	18.61	0.08	18.69	0.01	18.25	0.01	18.25	0.05	18.02	0.04
M081936.62-063047.9*a	280	<18.1	<16.3	⋯	2.507	SALT	Q						
	J081936.63-063048.4	124.9026465	−6.5134706	15.56	0.04	14.66	0.06	11.11	0.15				
	PSO J124.9027-06.5134	5	65	19.79	0.06	19.88	0.03	19.38	0.03	19.33	0.03	19.2	0.04

Table 1

(Continued)

NVSS ID	Flux	$B_{\rm maj}$	$B_{\rm min}$	$B_{\rm pa}$	Redshift	Telescope	AGN-type						
	WISE ID	R.A.$_W$	Decl.$_W$	W1	δW1	W2	δW2	W3	δW3				
	PS1 ID	nStackDets	nDetections	g	δg	r	δr	i	δi	z	δz	y	δy
(1)	(2)	(3)	(4)	(5)	(6)	(7)	(8)						
	(9)	(10)	(11)	(12)	(13)	(14)	(15)	(16)	(17)				
	(18)	(19)	(20)	(21)	(22)	(23)	(24)	(25)	(26)	(27)	(28)	(29)	(30)
M082638.44-032426.4	221.9	<18.3	<16.9	⋯	0.437	SALT	G						
	J082638.42-032427.2	126.6601067	−3.407575	15.49	0.04	14.77	0.07	11.63	0.28				
	PSO J126.6601-03.4076	0	79	20.29	0.05	20.36	0.03	19.57	0.02	19.61	0.04	19.26	0.05
M083601.35+040636.0	435.3	<18.2	<15.7	⋯	0.743	SUGAR	G						
	J083601.33+040637.4	129.005552	4.1104025	15.52	0.05	14.91	0.07	11.86	⋯				
	PSO J129.0057+04.1100	5	28	−999	−999	21.52	0.07	21.31	0.08	20.47	0.1	20.4	0.18
M083608.59-133635.1	919.2	48	<18.2	−63	0.160	SALT	G						
	J083608.56-133634.3	129.0356672	−13.6095406	14.01	0.03	13.18	0.03	9.82	0.06				
	PSO J129.0356-13.6095	5	78	19.56	0.03	18.65	0.03	18.23	0.02	18.04	0.04	17.81	0.03
M085826.92-260721.0	404.5	<18.6	<17.2	⋯	2.036	SALT	Q						
	J085826.85-260720.9	134.6118804	−26.12249	15.47	0.04	14.33	0.04	11.04	0.12				
	PSO J134.6118-26.1225	5	67	19.27	0.02	19.09	0.02	18.72	0.01	18.44	0.02	18.51	0.02
M090337.99-311739.0	209.5	<16.6	<15.7	⋯	1.670	SALT	Q						
	J090337.92-311739.0	135.9080123	−31.2941691	16.68	0.08	15.76	0.12	12.12	0.32				
M090910.66-163753.8	340.1	<15.7	<13.9	⋯	2.475	SUGAR	Q						
	J090910.56-163756.3	137.2940394	−16.6323287	15.87	0.06	15.2	0.09	11.84	⋯				
	PSO J137.2937-16.6327	6	2	−999	−999	−999	−999	21.67	0.16	−999	−999	−999	−999
M090911.33-313334.1	610.1	50	<16.7	−65.4	0.884	SALT	G						
	J090911.50-313335.3	137.2979271	−31.5598218	16.98	0.1	16.27	0.19	12.63	⋯				
M090916.99-050053.2	457.2	<16.7	<15.4	⋯	0.404	SUGAR	G						
	J090917.01-050052.5	137.3208807	−5.0146108	15.68	0.05	15	0.08	11.75	0.26				
	PSO J137.3209-05.0147	5	41	22.05	0.06	20.77	0.1	20.21	0.07	19.9	0.04	19.8	0.06
M091051.01-052626.8	337.9	15.8	<15.5	2.8	2.395	SUGAR	Q						
	J091050.99-052629.1	137.7124859	−5.4414291	14.57	0.03	13.61	0.04	10.46	0.08				
	PSO J137.7125-05.4414	5	83	18.24	0.01	18.03	0.02	17.86	0.01	17.73	0.01	17.48	0.02
M091253.34-135241.9*c	255.7	<16.5	<16.3	⋯	1.088	SALT	Q						
	J091253.36-135242.1	138.2223389	−13.8783827	15.62	0.04	14.98	0.07	11.9	0.24				
	PSO J138.2222-13.8785	5	38	21.29	0.07	20.83	0.09	20.62	0.13	20.56	0.1	19.99	0.09
M092902.69-293020.8	899.6	<18.8	<17.4	⋯	0.749	SALT	G						
	J092902.70-293019.9	142.2612874	−29.5055398	15.52	0.04	14.48	0.05	9.44	0.04				
	PSO J142.2613-29.5055	5	27	21.67	0.08	20.75	0.05	20.78	0.07	19.03	0.01	20.17	0.07
M092956.48+014843.8	248.7	<18.2	<17.2	⋯	2.331	SALT	Q						
	J092956.47+014844.2	142.485295	1.8123026	15.19	0.04	14.34	0.05	11.18	0.14				
	PSO J142.4852+01.8123	5	59	20.2	0.05	19.9	0.03	19.23	0.03	18.9	0.02	18.64	0.02
M093919.21-173135.4	263.3	<16.1	<15.3	⋯	1.831	SUGAR	Q						
	J093919.19-173135.6	144.8299719	−17.5265832	15.19	0.04	14.07	0.04	10.67	0.08				
	PSO J144.8300-17.5266	10	48	21.63	0.1	19.88	0.14	21	0.05	20.7	0.12	18.93	0.02
M094040.47-002800.1	359.3	<17.1	<16.1	⋯	2.383	SALT	Q						
	J094040.47-002801.4	145.1686386	−0.4670779	16.51	0.09	15.88	0.16	12	⋯				
	PSO J145.1686-00.4670	5	56	19.45	0.02	20	0.07	19.89	0.05	19.54	0.05	19.26	0.08
M094146.01-032121.7	346.2	<18.5	<17.5	⋯	1.848	SUGAR	Q						
	J094145.98-032121.7	145.4415998	−3.3560372	16.59	0.09	15.77	0.14	11.94	⋯				
	PSO J145.4417-03.3561	4	17	21.22	0.09	21.01	0.01	20.6	0.02	20.53	0.04	−999	−999
M095138.34-060138.0	378.8	<18.4	<16.1	⋯	1.844	SUGAR	Q						
	J095138.35-060137.5	147.9098297	−6.0270882	16.27	0.07	15.46	0.13	11.95	⋯				
	PSO J147.9098-06.0271	5	51	20.38	0.02	20.18	0.06	19.6	0.02	19.75	0.03	19.44	0.09

Table 1
(Continued)

NVSS ID	Flux	B_{maj}	B_{min}	B_{pa}	Redshift	Telescope	AGN-type						
	WISE ID	R.A.$_{W}$	Decl.$_{W}$	W1	δW1	W2	δW2	W3	δW3				
	PS1 ID	nStackDets	nDetections	g	δg	r	δr	i	δi	z	δz	y	δy
(1)	(2)	(3)	(4)	(5)	(6)	(7)	(8)						
	(9)	(10)	(11)	(12)	(13)	(14)	(15)	(16)	(17)				
	(18)	(19)	(20)	(21)	(22)	(23)	(24)	(25)	(26)	(27)	(28)	(29)	(30)
M095231.66-245349.1	209.5	<15.0	<14.0	⋯	2.626	SALT	Q						
	J095231.67-245351.0	148.1319654	−24.8975143	15.98	0.05	15.13	0.08	12.01	0.27				
	PSO J148.1319-24.8975	5	62	19.18	0.02	19.01	0.01	19.06	0.01	18.84	0.02	18.67	0.06
M095423.67+004350.5[*]b	291.6	<19.8	<17.6	⋯	1.712	SALT	Q						
	J095423.72+004351.3	148.5988716	0.7309207	15.93	0.06	14.88	0.08	11.71	0.26				
	PSO J148.5989+00.7310	5	62	20.67	0.04	20	0.06	19.74	0.04	19.63	0.05	19.52	0.14
M095654.60-131718.1[*]c	216	26	<16.6	−86.4	1.198	SALT	Q						
	J095654.65-131718.7	149.2277088	−13.2885524	16.19	0.05	15.24	0.08	12.04	0.48				
	PSO J149.2276-13.2884	0	4	−999	−999	21.42	0.16	21.69	0.2	−999	−999	−999	−999
M100715.18-124746.7	381.1	<15.7	<15.4	⋯	2.113	SALT	Q						
	J100715.22-124745.9	151.8134506	−12.7961	15.38	0.04	14.24	0.05	11.01	0.12				
	PSO J151.8134-12.7961	10	74	18.4	0.01	18.28	0	18.18	0.01	18	0.01	18.07	0.02
M100743.51-181732.4	205.2	49.2	<19.5	84.6	0.493	NOT	G						
	J100743.58-181731.1	151.9316084	−18.2919748	14.96	0.03	14.22	0.05	10.16	0.06				
	PSO J151.9316-18.2919	5	60	21.56	0.06	20.37	0.05	19.63	0.03	19.54	0.04	19.29	0.03
M100802.27-095919.3	645.3	15.7	<18.6	−82	1.688	NOT	Q						
	J100802.30-095919.8	152.0095896	−9.9888589	15.7	0.05	14.55	0.06	11.24	0.19				
	PSO J152.0098-09.9888	10	78	19.34	0.02	19.35	0.04	19.3	0.04	19.04	0.01	19.01	0.02
M100954.53+160203.8	201.9	<15.9	<15.2	⋯	1.770	NOT	Q						
	J100954.55+160203.4	152.4772922	16.0342888	16.09	0.06	15.18	0.10	11.57	0.25				
	PSO J152.4773+16.0343	5	83	20.88	0.02	20.74	0.02	20.55	0.02	20.36	0.03	20	0.06
M101313.10-254654.7	248.8	<16.0	<14.0	⋯	2.965	SALT	Q						
	J101313.09-254654.7	153.3045753	−25.7818673	17.14	0.12	15.98	0.15	12.12	⋯				
	PSO J153.3046-25.7819	5	13	21.6	0.08	21.12	0.08	20.82	0.01	20.55	0.21	19.32	0.06
M101357.73-245933.6	255	<18.7	<15.6	⋯	1.814	SALT	Q						
	J101357.81-245932.9	153.4908974	−24.9924937	16.67	0.09	15.53	0.10	12.07	⋯				
	PSO J153.4909-24.9925	5	59	20.1	0.03	20.22	0.02	19.92	0.03	19.79	0.04	19.52	0.05
M101555.33-082245.7	250.5	<18.6	<16.4	⋯	1.430	SALT	Q						
	J101555.39-082245.5	153.9808222	−8.3793266	17.95	0.27	16.04	0.19	11.74	0.27				
	PSO J153.9809-08.3794	5	28	22.19	0.14	21.55	0.06	21.46	0.05	20.84	0.05	−999	−999
M102159.78-011002.4	500.6	<16.1	<14.0	⋯	1.493	SALT	Q						
	J102159.77-011002.5	155.4990517	−1.1673705	15.72	0.05	15.01	0.09	11.92	0.33				
	PSO J155.4990-01.1674	3	44	21.6	0.07	20.97	0.08	20.49	0.04	20.13	0.04	19.54	0.09
M102441.29-153025.2	226.3	<16.9	<16.7	⋯	0.792	SALT	Q						
	J102441.30-153026.3	156.1720931	−15.5073221	15.39	0.04	14.44	0.05	11.25	0.17				
	PSO J156.1721-15.5073	5	58	20.23	0.03	19.88	0.02	19.67	0.02	19.3	0.02	19.33	0.03
M102444.61-085206.4	463.8	39.3	<19.1	−29.8	0.455	SUGAR	G						
	J102444.56-085205.9	156.1856868	−8.8683093	16.36	0.07	15.58	0.12	12.51	0.49				
	PSO J156.1857-08.8684	5	44	−999	−999	21.28	0.04	20.57	0.04	20.44	0.02	19.65	0.16
M102548.78-042933.7	363.5	<16.5	<15.9	⋯	2.292	SALT	Q						
	J102548.76-042933.0	156.4531736	−4.4925229	16.25	0.07	15.47	0.11	12.11	⋯				
	PSO J156.4532-04.4924	5	75	19.57	0.01	19.75	0.03	19.66	0.02	19.45	0.02	19.31	0.04
M103051.52-092525.0[*]d	890.9	<17.5	<15.5	⋯	0.413	SALT	G						
	J103051.50-092523.8	157.7146096	−9.4232841	16.16	0.06	15.32	0.09	12.03	⋯				
M103335.61-121032.1	2065.1	14.3	<17.3	−46.2	1.328	NOT	G						
	J103335.62-121032.0	158.3984486	−12.1755657	16.59	0.08	15.8	0.13	11.7	0.23				
	PSO J158.3981-12.1757	5	47	21.1	0.03	21.01	0.03	20.97	0.03	20.74	0.04	−999	−999

Table 1

(Continued)

NVSS ID	Flux	$B_{\rm maj}$	$B_{\rm min}$	$B_{\rm pa}$	Redshift	Telescope	AGN-type						
	WISE ID	R.A.$_W$	Decl.$_W$	W1	δW1	W2	δW2	W3	δW3				
	PS1 ID	nStackDets	nDetections	g	δg	r	δr	i	δi	z	δz	y	δy
(1)	(2)	(3)	(4)	(5)	(6)	(7)	(8)						
	(9)	(10)	(11)	(12)	(13)	(14)	(15)	(16)	(17)				
	(18)	(19)	(20)	(21)	(22)	(23)	(24)	(25)	(26)	(27)	(28)	(29)	(30)
M104051.07-144919.4	269.6	<17.4	<17.0	···	1.526	SALT	Q						
	J104051.04-144918.9	160.2126978	−14.8219317	17.2	0.13	16.44	0.25	12.61	···				
	PSO J160.2126-14.8219	5	54	21.41	0.05	20.95	0.05	20.72	0.08	20.68	0.05	20.28	0.08
M104314.53-232317.5	212.1	<19.7	<14.7	···	2.881	SALT	Q						
	J104314.52-232319.3	160.8105239	−23.3886967	16.57	0.08	15.95	0.16	12.14	···				
	PSO J160.8104-23.3886	5	54	19.9	0.05	19.72	0.03	19.72	0.02	19.62	0.08	19.35	0.06
M104347.34+164106.9	259.1	<16.4	<15.7	···	0.399	NOT	G						
	J104347.32+164107.4	160.9471896	16.6854078	15.82	0.05	15.19	0.12	11.74	···				
	PSO J160.9472+16.6854	5	58	22.21	0.05	21.24	0.05	20.54	0.03	20.06	0.04	19.8	0.11
M105024.43-031808.8	243.5	<18.3	<16.3	···	1.813	SUGAR	Q						
	J105024.49-031808.4	162.6020829	−3.302339	15.25	0.04	14.06	0.04	10.77	0.1				
	PSO J162.6021-03.3023	5	59	19.07	0.01	18.85	0.01	18.54	0	18.59	0.02	18.5	0.04
M105955.36-111818.7	314.5	<16.5	<14.1	···	1.939	SUGAR	Q						
	J105955.37-111818.2	164.9807386	−11.3050771	16.6	0.09	15.71	0.14	12.18	···				
	PSO J164.9808-11.3051	5	62	20.43	0.05	20.61	0.06	20.2	0.02	19.83	0.03	19.6	0.12
M111820.61-305459.0	233.2	<16.9	<15.6	···	2.352	SALT	Q						
	J111820.61-305458.5	169.5859042	−30.9162666	14.8	0.03	13.99	0.04	10.63	0.1				
M111917.36-052707.9	1174.4	14.7	<18.6	38.7	2.651	SUGAR	Q						
	J111917.40-052707.5	169.8225305	−5.4521081	16.58	0.09	15.94	0.17	11.65	···				
	PSO J169.8226-05.4520	5	54	20.47	0.02	20.26	0.03	20.2	0.02	19.94	0.04	19.62	0.09
M112402.56-150159.1	261.9	<17.0	<16.4	···	2.551	SUGAR	Q						
	J112402.53-150158.7	171.0105586	−15.0329758	16.65	0.09	15.77	0.15	11.87	0.3				
	PSO J171.0107-15.0330	5	57	19.79	0.05	19.61	0.01	19.72	0.02	19.56	0.03	19.45	0.05
M113750.46-153458.7	241.1	<17.9	<14.0	···	1.496	SALT	Q						
	J113750.49-153457.8	174.4604049	−15.5827307	16.46	0.08	15.15	0.09	11.78	0.26				
	PSO J174.4603-15.5827	10	78	19.88	0.05	19.69	0.02	19.55	0.03	19.48	0.03	19.63	0.05
M114226.58-263313.7	294.7	<18.1	<15.9	···	3.237	SALT	Q						
	J114226.59-263313.0	175.6107945	−26.5536221	15.6	0.04	14.86	0.07	11.54	0.21				
	PSO J175.6107-26.5536	10	56	18.9	0.02	18.73	0.01	18.76	0.01	18.74	0.01	18.61	0.08
M114825.45+140449.7	322	<17.8	<17.1	···	0.727	NOT	G						
	J114825.54+140451.1	177.106422	14.0808677	16.27	0.07	15.61	0.14	11.79	···				
	PSO J177.1060+14.0803	3	15	−999	−999	21.65	0.16	21.68	0.04	20.62	0.05	−999	−999
M115043.70+131736.1	254.4	<17.5	<16.5	···	1.530	NOT	Q						
	J115043.60+131735.3	177.6817055	13.2931528	16.31	0.07	15.24	0.10	12.02	0.36				
	PSO J177.6817+13.2931	5	71	19.76	0.04	19.77	0.04	19.51	0.04	19.58	0.03	19.42	0.06
M115222.04-270126.3	238.2	<17.7	<15.4	···	2.703	SALT	Q						
	J115222.02-270126.1	178.0917554	−27.0239355	16.93	0.1	16.16	0.18	12.4	···				
	PSO J178.0919-27.0238	5	37	21.01	0.04	20.97	0.07	20.9	0.05	20.76	0.11	−999	−999
M115306.72-044254.5	684.8	<19.3	<17.9	···	2.591	SALT	Q						
	J115306.66-044255.8	178.2777737	−4.7155199	14.96	0.04	14.04	0.04	10.41	0.08				
	PSO J178.2777-04.7155	5	76	18.68	0.02	18.33	0.02	18.29	0.01	18.04	0.01	17.89	0.01
M115450.38-281249.7[*]c	444.5	<18.3	<17.2	···	0.897	SALT	Q						
	J115450.43-281251.0	178.7101313	−28.2141796	16.47	0.08	15.54	0.11	12.08	0.41				
	PSO J178.7101-28.2141	5	53	20.48	0.06	20.32	0.03	19.98	0.02	19.91	0.04	19.77	0.05
M120632.23-071452.6	698.8	<16.9	<15.6	···	2.263	NOT	Q						
	J120632.18-071453.1	181.634117	−7.2480922	16.03	0.06	15.41	0.13	11.68	0.3				
	PSO J181.6341-07.2481	5	68	19.69	0.01	19.67	0.03	19.57	0.04	19.38	0.03	19.31	0.04

Table 1
(Continued)

NVSS ID	Flux	B_{maj}	B_{min}	B_{pa}	Redshift	Telescope	AGN-type						
	WISE ID	R.A.$_W$	Decl.$_W$	W1	δW1	W2	δW2	W3	δW3				
	PS1 ID	nStackDets	nDetections	g	δg	r	δr	i	δi	z	δz	y	δy
(1)	(2)	(3)	(4)	(5)	(6)	(7)	(8)						
	(9)	(10)	(11)	(12)	(13)	(14)	(15)	(16)	(17)				
	(18)	(19)	(20)	(21)	(22)	(23)	(24)	(25)	(26)	(27)	(28)	(29)	(30)
M121059.72-162042.7	328.3	<19.2	<17.0	⋯	1.083	SALT	Q						
	J121059.64-162043.4	182.7485411	−16.345399	16.83	0.11	15.99	0.17	12.43	0.51				
	PSO J182.7487-16.3454	5	55	21.63	0.04	21.27	0.04	20.68	0.03	20.39	0.03	19.81	0.08
M121211.89-373826.9	343.4	<18.1	<16.4	⋯	1.9243	SALT	Q						
	J121211.96-373826.5	−37.6407047	183.0498351	15.89	0.04	15.01	0.06	11.77	0.18				
M121514.42-062803.5	360.4	<18.5	<13.9	⋯	3.218	SUGAR	Q						
	J121514.39-062803.7	183.8099607	−6.4677219	15.78	0.06	15.01	0.11	11.76	⋯				
	PSO J183.8100-06.4678	5	50	19.88	0.02	19.74	0.03	19.68	0.04	19.5	0.06	19.26	0.04
M121836.18-063115.8	409.1	<17.2	<16.6	⋯	0.658	SUGAR	Q						
	J121836.19-063116.9	184.6508305	−6.5213777	14.35	0.03	13.5	0.04	10.41	0.08				
	PSO J184.6508-06.5213	5	63	18.84	0.03	18.84	0.02	18.71	0.02	18.64	0.03	18.85	0.04
M121905.45-180911.2	300.3	<17.5	<15.6	⋯	0.189	NOT	G						
	J121905.43-180910.9	184.7726392	−18.1530363	14.8	0.03	14.15	0.04	11.26	0.16				
	PSO J184.7726-18.1531	5	76	20.16	0.02	19.19	0.02	18.73	0.01	18.44	0.02	18.32	0.02
M122123.49-123724.1	343.7	14.5	<15.7	85.1	1.882	NOT	Q						
	J122123.57-123723.0	185.3482462	−12.6230677	15.67	0.05	14.79	0.07	11.77	0.25				
	PSO J185.3482-12.6230	5	59	19.77	0.02	19.47	0.04	19.01	0.01	18.9	0.01	18.81	0.03
M123150.30-123637.5	276	<16.3	<15.6	⋯	2.106	SUGAR	Q						
	J123150.26-123636.8	187.9594437	−12.6102438	15	0.04	13.86	0.04	10.42	0.1				
	PSO J187.9594-12.6103	5	66	19.07	0.02	18.83	0.01	18.58	0.01	18.33	0.01	18.18	0.02
M123410.08-332638.5	297.9	<19.9	<16.1	⋯	2.820	SALT	Q						
	J123409.97-332638.7	188.5415468	−33.4441047	17.59	0.15	16.75	0.29	12.83	⋯				
M124448.99-044610.2	384.9	<16.8	<13.9	⋯	3.104	SALT	Q						
	J124449.01-044608.8	191.2042373	−4.7691286	16.25	0.07	15.58	0.12	11.92	0.31				
	PSO J191.2043-04.7692	5	55	20.84	0.02	20.58	0.02	20.46	0.03	20.43	0.04	19.9	0.1
M125215.28-310351.2	331.6	<17.9	<16.0	⋯	1.943	SALT	Q						
	J125215.17-310351.2	193.0632173	−31.0642344	16.47	0.07	15.44	0.09	12.14	0.26				
M125442.98-383356.4	219.2	<18.8	<17.6	⋯	2.776	SALT	Q						
	J125443.00-383357.3	193.6791669	−38.5659343	17.07	0.1	16.07	0.15	12.52	0.42				
M125611.49-214411.7	260.7	<15.2	<15.2	⋯	2.178	SALT	Q						
	J125611.41-214410.9	194.0475791	−21.7363772	14.55	0.03	13.77	0.04	10.8	0.09				
	PSO J194.0476-21.7363	5	73	18.8	0.01	18.32	0.01	17.96	0.01	17.69	0.01	17.68	0.02
M130457.29-015457.7	325.8	<17.0	<15.6	⋯	2.100	SALT	Q						
	J130457.38-015458.6	196.2391148	−1.9162803	16.68	0.1	15.76	0.17	12.49	0.45				
	PSO J196.2389-01.9163	5	46	20.6	0.02	20.67	0.02	20.54	0.05	20.07	0.03	20.13	0.04
M130958.32+073217.5	205	<16.8	<15.2	⋯	0.487	SALT	G						
	J130958.33+073217.3	197.4930738	7.5381498	16.2	0.06	15.21	0.09	11.38	0.18				
	PSO J197.4931+07.5382	5	16	−999	−999	21.63	0.15	21.41	0.07	21.08	0.1	20.26	−999
M131139.29-221641.2*d	4093	<17.7	<16.6	⋯	0.885	SALT	Q						
	J131139.34-221642.1	197.913957	−22.2783632	15.63	0.04	14.97	0.07	11.94	0.27				
	PSO J197.9139-22.2782	5	39	21.86	0.17	21.56	0.09	20.73	0.03	20.33	0.04	19.53	0.06
M131207.86-202652.4*f	778.1	<19.6	<16.5	⋯	0.977	SALT	G						
	J131207.85-202652.8	198.032746	−20.448026	16.51	0.08	15.76	0.13	12.64	0.42				
	PSO J198.0328-20.4480	3	4	−999	−999	−999	−999	21.58	0.19	20.88	0.34	−999	−999
M131301.41-272258.6	239.3	14.9	<16.3	41.8	1.567	SALT	Q						
	J131301.42-272258.7	198.2559293	−27.3829913	15.54	0.05	14.47	0.05	11.16	0.13				
	PSO J198.2559-27.3830	5	38	21.45	0.05	21.03	0.12	20.77	0.08	20.23	0.04	19.79	0.06

Table 1
(Continued)

NVSS ID	Flux	$B_{\rm maj}$	$B_{\rm min}$	$B_{\rm pa}$	Redshift	Telescope	AGN-type						
	WISE ID	R.A.$_W$	Decl.$_W$	W1	δW1	W2	δW2	W3	δW3				
	PS1 ID	nStackDets	nDetections	g	δg	r	δr	i	δi	z	δz	y	δy
(1)	(2)	(3)	(4)	(5)	(6)	(7)	(8)						
	(9)	(10)	(11)	(12)	(13)	(14)	(15)	(16)	(17)				
	(18)	(19)	(20)	(21)	(22)	(23)	(24)	(25)	(26)	(27)	(28)	(29)	(30)
M131517.56-274504.0	468.4	40.1	<18.0	17	1.912	SALT	G						
	J131517.61-274505.1	198.823416	−27.7514337	16.86	0.09	15.96	0.15	12.12	0.28				
M131736.55-134532.8	244.5	<19.3	<16.3	⋯	1.407	SALT	Q						
	J131736.56-134532.6	199.4023338	−13.7590663	15.64	0.04	14.47	0.05	11.1	0.12				
	PSO J199.4022-13.7591	5	52	20.55	0.06	20.22	0.02	20.21	0.03	20.1	0.05	19.81	0.1
M131856.01-144155.0	283	20.1	<17.8	51.3	0.632	NOT	Q						
	J131856.07-144154.4	199.7336621	−14.6984528	15.14	0.03	14.08	0.04	10.67	0.09				
	PSO J199.7336-14.6985	5	68	19.73	0.07	19.63	0.02	19.28	0.02	19.51	0.04	19.43	0.04
M132333.24-223934.5	276.1	<19.7	<16.1	⋯	1.478	SALT	Q						
	J132333.24-223934.0	200.8885365	−22.6594475	16.18	0.06	15.2	0.08	11.91	0.23				
	PSO J200.8885-22.6595	5	63	20.73	0.06	20.24	0.05	20.01	0.03	20.11	0.04	19.82	0.07
M132657.20-280831.4	404.5	<18.9	<17.2	⋯	2.238	SALT	Q						
	J132657.18-280832.6	201.738268	−28.1424123	16.35	0.06	15.53	0.11	12.45	0.52				
	PSO J201.7379-28.1420	5	51	20.54	0.03	20.67	0.14	20.11	0.06	20.03	0.09	19.94	0.11
M133520.56-391144.6	306.2	<17.1	<15.5	⋯	2.055	SALT	Q						
	J133520.57-391146.0	203.835731	−39.1961354	15.98	0.04	15.14	0.07	11.85	0.21				
M134309.26-083457.5	241.5	<19.3	<16.5	⋯	1.076	SUGAR	Q						
	J134309.30-083456.6	205.7887762	−8.5824088	15.93	0.05	15.09	0.08	11.88	0.24				
	PSO J205.7887-08.5825	5	64	20.07	0.03	19.73	0.04	19.44	0.02	19.61	0.05	19.29	0.05
M135131.98-101932.9	726.1	<18.9	<17.4	⋯	2.999	SUGAR	Q						
	J135131.98-101932.1	207.8832846	−10.3256104	15.02	0.03	14.12	0.04	10.74	0.09				
	PSO J207.8833-10.3256	5	89	18.15	0.01	17.93	0.01	17.86	0.01	17.86	0.01	17.7	0.01
M135547.99-370955.5*c	248.8	<18.0	<17.0	⋯	1.323	SALT	Q						
	J135547.99-370956.3	208.9499945	−37.1656536	16.4	0.06	15.4	0.09	11.88	0.21				
M141327.20-342235.1	274.7	<17.1	<14.9	⋯	2.812	SALT	Q						
	J141327.16-342235.6	213.3631998	−34.3765588	15.42	0.04	14.35	0.05	10.81	0.09				
M141338.15-071625.3	232.7	17.2	<16.7	−88.6	0.416	SALT	G						
	J141338.23-071624.5	213.4093225	−7.2734885	17.16	0.12	16.29	0.21	12.37	0.38				
	PSO J213.4090-07.2735	5	32	22.15	0.01	21.48	0.11	20.68	0.05	20.93	0.05	20.29	0.23
M142155.55-310427.9	732.6	<18.0	<17.7	⋯	1.568	SALT	Q						
	J142155.57-310425.1	215.48157	−31.07366	16.96	0.12	16.06	0.20	12.3	⋯				
M142213.87-091018.4	398.7	<18.8	<16.8	⋯	0.876	SALT	G						
	J142213.88-091018.2	215.5578602	−9.1717354	15.82	0.05	15.14	0.09	11.09	0.13				
	PSO J215.5579-09.1717	4	11	−999	−999	−999	−999	21.38	0.18	21.03	0.06	20.6	0.13
M143709.04-294718.5	273.8	<18.6	<17.3	⋯	2.331	SALT	Q						
	J143708.95-294718.7	219.2873327	−29.7885418	16.23	0.08	15.36	0.14	12.17	0.32				
	PSO J219.2874-29.7885	5	21	19.6	0.05	19.54	0.03	19.37	0.03	19.15	0.01	19.15	0.05
M144032.09+053120.7	214.9	<18.6	<18.1	⋯	0.754	SALT	Q						
	J144032.02+053122.4	220.1334503	5.5229058	15.39	0.04	14.52	0.05	11.44	0.16				
	PSO J220.1335+05.5229	5	69	20.33	0.04	20.31	0.04	20.17	0.03	19.75	0.03	19.8	0.05
M144851.10-112215.6	455.5	<13.9	<13.9	⋯	2.630	SALT	Q						
	J144851.15-112215.6	222.2131474	−11.3710267	14.95	0.04	14.18	0.05	10.87	0.1				
	PSO J222.2132-11.3710	5	72	18.21	0.02	18.07	0.02	18.03	0.02	17.9	0.01	17.77	0.01
M145212.06-255639.8*b	229.9	<16.2	<15.8	⋯	1.693	SALT	Q						
	J145212.09-255639.5	223.050385	−25.9443099	15.88	0.05	14.75	0.07	11.3	0.14				
	PSO J223.0503-25.9444	5	64	20.11	0.01	19.82	0.01	19.45	0.01	19.49	0.02	19.4	0.07

Table 1
(Continued)

NVSS ID	Flux	$B_{\rm maj}$	$B_{\rm min}$	$B_{\rm pa}$	Redshift	Telescope	AGN-type						
	WISE ID	R.A.$_W$	Decl.$_W$	W1	δW1	W2	δW2	W3	δW3				
	PS1 ID	nStackDets	nDetections	g	δg	r	δr	i	δi	z	δz	y	δy
(1)	(2)	(3)	(4)	(5)	(6)	(7)	(8)						
	(9)	(10)	(11)	(12)	(13)	(14)	(15)	(16)	(17)				
	(18)	(19)	(20)	(21)	(22)	(23)	(24)	(25)	(26)	(27)	(28)	(29)	(30)
M145342.95-132738.2	254.5	<19.6	<17.3	⋯	2.370	SALT	Q						
	J145342.94-132735.8	223.4289562	−13.4599571	14.6	0.03	13.51	0.04	10.13	0.05				
	PSO J223.4290-13.4600	5	59	18.4	0.01	17.98	0.02	17.86	0.01	17.67	0.01	17.47	0.01
M145502.84-170014.2[*]a	294.7	<17.1	<15.8	⋯	2.291	SALT	Q						
	J145502.77-170012.5	223.7615501	−17.0034926	16.41	0.08	15.7	0.18	11.85	0.28				
	PSO J223.7617-17.0039	5	33	21.21	0.07	21.04	0.06	20.82	0.04	20.61	0.03	20.07	0.15
M145536.16-095709.2	438.2	<18.8	<17.1	⋯	1.992	SALT	G						
	J145536.14-095707.4	223.9005923	−9.9520677	17.3	0.15	15.87	0.15	11.31	0.12				
M145625.83+045645.2	287.9	<18.7	<17.8	⋯	2.134	SUGAR	Q						
	J145625.81+045644.5	224.1075561	4.9457114	16.21	0.06	15.5	0.10	12.62	0.42				
	PSO J224.1075+04.9458	10	59	20.3	0.03	20.01	0.01	19.73	0.01	19.38	0.02	19.36	0.03
M145908.92-164542.3	378.9	<16.9	<15.4	⋯	2.006	SALT	Q						
	J145908.90-164541.9	224.7870882	−16.7616588	16.4	0.09	15.4	0.16	11.88	⋯				
	PSO J224.7871-16.7621	10	29	21.26	0.05	21.25	0.11	20.8	0.04	20.55	0.05	−999	−999
M150425.30+081858.6	210.8	<14.4	<14.0	⋯	2.035	SALT	Q						
	J150425.26+081858.7	226.1052909	8.3163078	16.33	0.06	15.24	0.08	11.71	0.18				
	PSO J226.1054+08.3163	10	64	20.89	0.02	20.75	0.07	20.47	0.01	20.2	0.05	20.04	0.07
M150712.88-313729.6	295.5	<17.7	<15.4	⋯	1.920	SALT	Q						
	J150712.97-313731.8	226.8040709	−31.6255152	15.88	0.06	14.75	0.07	11.47	0.25				
M151129.01-072255.3	326.3	<18.6	<15.2	⋯	2.582	SALT	Q						
	J151128.97-072256.1	227.8707292	−7.3822515	15.62	0.04	14.98	0.09	11.85	0.22				
	PSO J227.8707-07.3823	5	76	18.95	0.02	18.79	0.01	18.89	0.01	18.59	0.01	18.46	0.02
M151204.81-132833.0[*]b	295	<17.1	<16.1	⋯	1.737	SALT	Q						
	J151204.73-132833.0	228.0197468	−13.4758439	16.35	0.08	15.45	0.11	12.26	0.35				
	PSO J228.0198-13.4758	5	58	20.59	0.04	20.57	0.03	20.12	0.02	20.2	0.03	20.02	0.06
M151304.72-252439.7	217.6	26.4	<16.0	−86.2	3.132	SALT	G						
	J151304.76-252439.7	228.2698707	−25.4110515	17.31	0.16	16.61	0.33	11.79	0.27				
M151944.77-115144.6[*]a	441	<15.8	<15.2	⋯	2.014	SALT	Q						
	J151944.76-115144.8	229.9365081	−11.862463	16.54	0.09	15.36	0.12	11.99	0.36				
	PSO J229.9366-11.8624	5	61	20.99	0.05	20.93	0.12	20.29	0.03	20.19	0.05	20.1	0.09
M154015.23-145341.5	203.3	<17.9	<16.4	⋯	2.098	SALT	Q						
	J154015.24-145341.9	235.0635366	−14.8949753	16.41	0.09	15.48	0.14	11.58	⋯				
	PSO J235.0634-14.8952	5	62	20.68	0.02	20.42	0.03	19.98	0.03	19.98	0.02	19.71	0.06
M154414.23-231200.8[*]c	296.4	<16.3	<16.0	⋯	1.026	SALT	Q						
	J154414.17-231200.7	236.0590426	−23.2002035	16.52	0.11	15.85	0.21	11.62	0.24				
	PSO J236.0591-23.2004	10	50	21.12	0.08	20.53	0.07	20.31	0.04	20.18	0.07	19.86	0.05
M155212.77-073246.5[*]c	222.3	<17.3	<16.6	⋯	1.015	SALT	Q						
	J155212.76-073246.5	238.0532006	−7.5462598	17.16	0.14	16.52	⋯	12.11	⋯				
	PSO J238.0532-07.5462	5	59	20.48	0.02	20.25	0.03	20.35	0.02	19.92	0.01	19.67	0.04
M155709.44+055216.1[*]d	231.7	<18.6	<16.8	⋯	0.668	SALT	G						
	J155709.42+055215.4	239.2892897	5.870947	16.34	0.07	15.51	0.10	11.27	0.15				
	PSO J239.2893+05.8709	5	51	−999	−999	21.53	0.07	20.99	0.04	20.49	0.04	−999	−999
M155825.35-215511.5	206.9	<19.5	<15.6	⋯	2.760	SALT	Q						
	J155825.36-215511.1	239.6056955	−21.9197627	14.6	0.03	13.52	0.04	10.17	0.08				
	PSO J239.6057-21.9198	5	53	20.4	0.01	19.95	0.03	19.43	0.02	18.97	0.02	18.55	0.03
M160903.37-145457.6[*]d	213.6	<17.2	<14.0	⋯	0.931	SALT	G						
	J160903.34-145458.2	242.2639473	−14.9161735	15.98	0.06	15.19	0.10	12.13	⋯				
	PSO J242.2641-14.9162	5	4	−999	−999	−999	−999	21.65	0.11	−999	−999	−999	−999

Table 1
(Continued)

NVSS ID (1)	Flux WISE ID PS1 ID (2) (9) (18)	$B_{\rm maj}$ R.A.$_W$ nStackDets (3) (10) (19)	$B_{\rm min}$ Decl.$_W$ nDetections (4) (11) (20)	$B_{\rm pa}$ W1 g (5) (12) (21)	Redshift δW1 δg (6) (13) (22)	Telescope W2 r (7) (14) (23)	AGN-type δW2 δr (8) (15) (24)	W3 i (16) (25)	δW3 δi (17) (26)	z (27)	δz (28)	y (29)	δy (30)
M161454.47-154550.7	473.8	<16.9	<14.7	⋯	0.920	SALT	Q						
	J161454.39-154549.1	243.7266435	−15.7636422	15.19	0.04	14.27	0.05	11.17	0.17				
	PSO J243.7267-15.7637	5	75	20.6	0.02	19.74	0.12	19.6	0.04	20.1	0.03	19.44	0.07
M161907.44-093953.1	340.3	<16.5	<15.6	⋯	2.891	SALT	Q						
	J161907.44-093952.5	244.7810354	−9.6646096	15.87	0.05	14.8	0.07	11.29	0.2				
	PSO J244.7810-09.6647	5	62	19.97	0.02	19.5	0.02	19.17	0.01	19.06	0.04	18.87	0.02
M162047.94+003653.2	317.8	<16.7	<15.7	⋯	2.438	SALT	Q						
	J162047.96+003653.1	245.1998398	0.6147621	14.77	0.03	14.05	0.04	11.13	0.16				
	PSO J245.1998+00.6148	10	71	18.92	0.01	18.7	0.01	18.61	0.03	18.28	0.01	18.12	0.02
M164950.51+062653.3	389.2	<18.0	<16.8	⋯	2.144	SUGAR	Q						
	J164950.54+062652.8	252.4606031	6.4480267	14.75	0.04	13.64	0.03	10.4	0.07				
	PSO J252.4604+06.4482	5	77	18.87	0.02	18.73	0.02	18.54	0.03	18.44	0.01	18.43	0.02
M165038.03-124854.5	275.5	<18.5	<15.5	⋯	2.527	SUGAR	Q						
	J165038.01-124853.2	252.6584023	−12.8147998	16.23	0.07	15.07	0.09	11.27	0.17				
	PSO J252.6585-12.8149	5	68	21.06	0.05	20.58	0.04	20.37	0.05	20.08	0.04	19.77	0.05
M165357.67-010214.2	317.4	<17.9	<15.5	⋯	1.088	SUGAR	Q						
	J165357.67-010213.4	253.4903148	−1.0370705	15.71	0.05	14.8	0.06	11.67	⋯				
	PSO J253.4904-01.0371	5	73	21.04	0.03	20.48	0.04	20.09	0.02	19.85	0.02	19.4	0.06
M165435.38+001719.5	255.3	<17.9	<15.3	⋯	2.363	SALT	Q						
	J165435.38+001719.2	253.6474532	0.2886674	16.92	0.11	15.92	0.16	12.49	0.48				
	PSO J253.6474+00.2888	5	71	20.08	0.04	20.01	0.03	19.84	0.03	19.67	0.04	19.39	0.04
M170333.50+064539.7	236.6	<17.9	<16.7	⋯	0.399	SALT	G						
	J170333.53+064539.3	255.8897404	6.7609306	15.24	0.04	14.07	0.04	10.66	0.1				
	PSO J255.8898+06.7609	5	55	22.02	0.21	21.18	0.03	20.35	0.04	20.07	0.05	19.57	0.05
M171627.09-061356.5	229.9	17.6	<20.0	−48.4	1.840	NOT	Q						
	J171627.07-061356.3	259.1128304	−6.2323088	14.03	0.03	12.82	0.03	9.49	0.05				
	PSO J259.1128-06.2323	5	67	19.95	0.01	19.07	0.03	18.41	0.01	18.13	0.01	17.89	0.02
M172105.79+162649.1	507.9	<17.8	<16.5	⋯	1.814	NOT	Q						
	J172105.77+162649.4	260.2740504	16.4470577	16.11	0.05	15.31	0.08	11.8	0.19				
	PSO J260.2741+16.4470	5	85	19.95	0.03	19.97	0.01	19.58	0.02	19.51	0.02	19.47	0.05
M172214.09+044316.8	765.5	19.9	<16.8	64.3	0.603	SALT	G						
	J172214.07+044317.0	260.5586294	4.7213966	15.01	0.04	14.29	0.05	11.1	0.14				
	PSO J260.5586+04.7214	4	35	−999	−999	21.62	0.09	20.6	0.03	20.33	0.08	20.13	0
M172507.45+062242.1	213.4	<18.5	<16.2	⋯	1.355	SUGAR	Q						
	J172507.43+062240.9	261.280972	6.3780555	15.4	0.04	14.49	0.05	11.36	0.17				
	PSO J261.2812+06.3781	10	73	19.45	0.02	19.05	0.02	18.8	0.03	18.76	0.01	18.77	0.04
M190923.40-392311.7	204.9	<18.9	<16.2	⋯	2.513	SALT	Q						
	J190923.31-392312.1	287.3471522	−39.3867043	16.62	0.1	15.54	0.14	11.57	0.25				
M192956.85-351619.6	276.4	<19.0	<19.0	⋯	0.333	SALT	G						
	J192956.83-351619.7	292.4867973	−35.2721648	14.25	0.03	13.52	0.04	10.24	0.09				
M193147.88-360659.1	779.6	<17.6	<16.9	⋯	0.449	SALT	G						
	J193147.94-360658.1	292.9497658	−36.1161433	14.73	0.04	13.85	0.04	9.84	0.05				
M194110.28-300720.9	315	<19.5	<15.1	⋯	2.059	SALT	Q						
	J194110.25-300720.5	295.2927432	−30.1223853	13.65	0.03	12.88	0.03	9.94	0.06				
M195243.90-193623.7	596.3	<19.3	<18.2	⋯	1.946	SALT	Q						
	J195243.87-193622.1	298.1828116	−19.6061565	16.06	0.08	14.85	0.10	11.24	0.18				
	PSO J298.1828-19.6064	10	67	20.65	0.03	20.48	0.02	20.16	0.02	19.87	0.06	19.55	0

Table 1

(Continued)

NVSS ID	Flux	$B_{\rm maj}$	$B_{\rm min}$	$B_{\rm pa}$	Redshift	Telescope	AGN-type						
	WISE ID	R.A.$_W$	Decl.$_W$	W1	δW1	W2	δW2	W3	δW3				
	PS1 ID	nStackDets	nDetections	g	δg	r	δr	i	δi	z	δz	y	δy
(1)	(2)	(3)	(4)	(5)	(6)	(7)	(8)						
	(9)	(10)	(11)	(12)	(13)	(14)	(15)	(16)	(17)				
	(18)	(19)	(20)	(21)	(22)	(23)	(24)	(25)	(26)	(27)	(28)	(29)	(30)
M195629.92-054246.9	351.3	<18.0	<16.8	⋯	1.103	SALT	Q						
	J195630.01-054247.4	299.1250677	−5.7131809	14.79	0.04	13.84	0.04	10.52	0.09				
	PSO J299.1250-05.7130	5	66	18.91	0.01	18.47	0.01	18.31	0.01	18.37	0.02	18.24	0.01
M200008.58-192138.3*c	896.7	<16.3	<16.1	⋯	1.187	SALT	Q						
	J200008.56-192138.3	300.0356945	−19.3606496	16.17	0.07	15.04	0.10	11.59	⋯				
	PSO J300.0357-19.3604	5	80	20.2	0.03	19.74	0.03	19.54	0.02	19.58	0.03	19.39	0.11
M200209.37-145531.8	620.3	<17.0	<15.6	⋯	2.192	SALT	Q						
	J200209.37-145532.4	300.539052	−14.9256698	16.41	0.08	15.46	0.12	12.34	0.45				
	PSO J300.5390-14.9255	5	67	20.52	0.03	20.26	0.01	19.88	0.01	19.56	0.02	19.7	0.06
M201708.96-293354.7	327.2	<17.1	<15.8	⋯	2.617	SALT	Q						
	J201708.95-293355.2	304.2873084	−29.5653586	15.91	0.06	14.89	0.08	11.42	0.21				
	PSO J304.2873-29.5653	5	67	19.79	0.02	19.37	0.01	19.51	0.02	19.03	0.01	18.89	0.04
M201952.74-394808.3*c	234.6	<19.2	<17.2	⋯	1.194	SALT	Q						
	J201952.68-394809.1	304.9695021	−39.8025426	16.17	0.06	15.32	0.10	12.15	0.32				
M203425.65-052332.2	419.7	14.9	<18.0	58.5	2.070	NOT	Q						
	J203425.62-052331.8	308.6067642	−5.3921681	15.58	0.05	14.61	0.06	11.18	0.16				
	PSO J308.6067-05.3922	5	66	18.67	0.01	18.64	0.02	18.41	0.01	18.23	0.01	18.28	0.02
M204608.17-391840.7	250	<17.0	<16.6	⋯	2.619	SALT	Q						
	J204607.98-391841.9	311.5332541	−39.3116438	16.63	0.08	15.74	0.14	12.53	⋯				
M204737.66-184141.6	241.7	<17.2	<16.1	⋯	2.994	SALT	Q						
	J204737.67-184141.2	311.9069909	−18.6947958	15.26	0.04	14.37	0.06	10.73	0.11				
	PSO J311.9069-18.6948	10	97	18.51	0.01	18.4	0.01	18.33	0.01	18.26	0.01	18.12	0.03
M205245.03-223410.6	330.9	<18.1	<15.9	⋯	2.072	SALT	Q						
	J205244.97-223410.3	313.1873933	−22.569539	15.11	0.04	14.08	0.04	10.82	0.12				
	PSO J313.1874-22.5695	5	96	18.36	0.01	18.17	0.01	18.07	0.01	17.87	0.01	17.93	0.01
M205456.08-093240.8	313.6	<18.1	<15.5	⋯	1.373	SUGAR	Q						
	J205456.07-093241.0	313.733661	−9.5447295	16.42	0.08	15.44	0.13	11.74	0.38				
	PSO J313.7336-09.5447	5	61	20.76	0.08	20.06	0.04	20.1	0.03	19.94	0.02	20.02	0.08
M205548.51-190545.6*c	227.3	<18.6	<16.0	⋯	0.809	SALT	Q						
	J205548.49-190546.1	313.9520661	−19.096164	16.41	0.09	15.38	0.12	12.2	0.46				
	PSO J313.9521-19.0961	10	73	21.15	0.07	21.1	0.09	20.63	0.02	20.63	0.03	20.45	0.19
M205842.96-173649.9	332.5	<17.6	<17.0	⋯	0.754	SALT	G						
	J205842.93-173650.6	314.6789027	−17.614082	15.63	0.05	14.8	0.08	11.6	⋯				
	PSO J314.6789-17.6141	5	46	22.43	0.19	21.69	0.06	21.07	0.03	20.21	0.03	20.16	0.14
M205959.61-144043.1	1018.1	<19.3	<16.7	⋯	0.689	SUGAR	G						
	J205959.57-144042.0	314.9982203	−14.6783358	14.63	0.03	13.63	0.04	10.45	0.11				
	PSO J314.9982-14.6783	10	68	21.28	0.05	20.54	0.05	20.05	0.02	19.41	0.05	19.5	0.04
M210143.29-174759.2	959.5	<16.5	<16.2	⋯	2.803	SALT	Q						
	J210143.32-174759.2	315.4305276	−17.7997963	17.31	0.15	16.48	0.29	12.35	0.48				
	PSO J315.4303-17.7997	5	68	21.2	0.03	20.84	0.05	20.98	0.02	20.74	0.08	−999	−999
M211311.86-393933.7	554.2	<18.4	<16.0	⋯	0.843	SALT	Q						
	J211311.86-393934.6	318.2994201	−39.6596198	15.12	0.04	14.13	0.04	10.89	0.11				
M211949.40-343938.6	287.2	<17.7	<17.1	⋯	0.452	SALT	G						
	J211949.37-343939.1	319.9557426	−34.6608848	15.43	0.04	14.76	0.06	11.78	⋯				
M212042.48+132724.2	401.5	<18.1	<16.5	⋯	1.110	NOT	Q						
	J212042.48+132727.1	320.177014	13.4575549	14.68	0.03	13.91	0.04	10.56	0.07				
	PSO J320.1771+13.4580	5	66	21.16	0.02	20.11	0.01	19.52	0.02	19.12	0.03	18.91	0.05

Table 1
(Continued)

NVSS ID	Flux	$B_{\rm maj}$	$B_{\rm min}$	$B_{\rm pa}$	Redshift	Telescope	AGN-type						
	WISE ID	R.A.$_W$	Decl.$_W$	W1	δW1	W2	δW2	W3	δW3				
	PS1 ID	nStackDets	nDetections	g	δg	r	δr	i	δi	z	δz	y	δy
(1)	(2)	(3)	(4)	(5)	(6)	(7)	(8)						
	(9)	(10)	(11)	(12)	(13)	(14)	(15)	(16)	(17)				
	(18)	(19)	(20)	(21)	(22)	(23)	(24)	(25)	(26)	(27)	(28)	(29)	(30)
M212758.87-385856.3	355.8	<16.9	<15.8	⋯	2.663	SALT	Q						
	J212758.91-385855.9	321.9954748	−38.9821988	16.81	0.1	16.01	0.17	11.58	0.21				
M212821.83-150453.2	245.5	<16.2	<14.7	⋯	2.547	SALT	Q						
	J212821.89-150453.1	322.0912098	−15.0814335	15.84	0.06	14.97	0.08	11.91	0.39				
	PSO J322.0912-15.0813	5	86	19.32	0.01	19.16	0.02	19.19	0.01	19.01	0.01	18.84	0.02
M213135.55-270159.0*b	205.9	<18.5	<15.9	⋯	1.921	SALT	Q						
	J213135.55-270159.1	322.8981403	−27.0331064	15.85	0.05	14.71	0.07	11.4	0.2				
	PSO J322.8981-27.0331	5	86	19.02	0.01	18.93	0.02	18.78	0.01	18.72	0.03	18.82	0.03
M213937.03+171826.9	219.4	20.3	<17.5	−63	1.700	NOT	Q						
	J213937.14+171825.9	324.90478	17.3072104	15.43	0.04	14.23	0.05	10.88	0.09				
	PSO J324.9048+17.3072	5	79	19.16	0.01	18.9	0.02	18.58	0.01	18.51	0.02	18.47	0.02
M214120.76-351516.9	371.3	<18.7	<16.0	⋯	2.599	SALT	Q						
	J214120.77-351517.1	325.3365774	−35.2547519	17.21	0.12	16.09	0.17	12.74	0.5				
M215445.08-382632.5	759.8	<18.5	<15.0	⋯	2.797	SALT	Q						
	J215445.04-382632.5	328.6876684	−38.4423862	13.5	0.03	12.64	0.03	9.46	0.04				
M215800.88+092546.4	437.7	<15.5	<14.4	⋯	0.447	SUGAR	G						
	J215800.86+092546.0	329.5036223	9.4294464	15.19	0.04	14.33	0.05	9.91	0.06				
	PSO J329.5037+09.4294	5	68	21.27	0.05	20.16	0.03	19.77	0.03	19.72	0.03	19.27	0.02
M220127.50+031215.6	300.5	<18.4	<15.7	⋯	2.181	SUGAR	Q						
	J220127.47+031215.6	330.3644887	3.2043567	16.31	0.07	15.61	0.12	11.78	⋯				
	PSO J330.3646+03.2042	8	48	20.46	0.2	21.04	0.08	20.95	0.05	20.47	0.18	−999	−999
M221843.50-122912.9*c	230.4	<16.7	<15.6	⋯	1.156	SALT	Q						
	J221843.45-122913.6	334.681072	−12.4871191	16.99	0.13	15.99	0.20	11.74	⋯				
	PSO J334.6810-12.4870	5	76	20.99	0.04	20.59	0.04	20.17	0.03	20.18	0.04	19.82	0.19
M222004.97+130712.1	812	21.8	<17.2	−5.7	0.760	NOT	Q						
	J222005.10+130710.9	335.0212696	13.1197105	14.94	0.04	14.19	0.05	11.11	0.17				
	PSO J335.0212+13.1197	5	74	20.59	0.02	20.31	0.03	20.11	0.01	19.55	0.03	19.75	0.12
M222332.81-310117.3	231.7	<16.1	<15.4	⋯	3.206	SALT	Q						
	J222332.79-310117.7	335.8866347	−31.0216	16.15	0.05	15.18	0.08	11.91	0.31				
M222420.03+130450.2	294.5	<17.3	<16.8	⋯	0.685	NOT	Q						
	J222420.06+130450.7	336.0836105	13.0807776	16.15	0.06	15.13	0.10	11.67	⋯				
	PSO J336.0835+13.0807	5	60	21.1	0.04	20.64	0.04	20.23	0.05	20.02	0.07	19.74	0.07
M223050.19+034836.8	242.8	<17.8	<16.7	⋯	1.330	SUGAR	Q						
	J223050.19+034835.8	337.7091503	3.8099591	16.53	0.08	15.92	0.15	12.15	⋯				
	PSO J337.7092+03.8101	5	20	22.39	0.26	21.88	0.04	21.63	0.03	21.04	0.07	−999	−999
M223816.27-124036.4	213.6	<18.4	<16.2	⋯	2.623	SALT	Q						
	J223816.28-124036.6	339.5678681	−12.6768403	16.31	0.07	15.47	0.12	11.83	0.32				
	PSO J339.5676-12.6768	5	86	21.21	0.06	20.56	0.02	20.53	0.03	20.12	0.02	19.7	0.11
M223826.48-134422.6	241.2	14.7	<16.6	−50.1	0.257	NOT	G						
	J223826.55-134421.5	339.6106451	−13.7393129	14.78	0.03	13.97	0.04	10.78	0.12				
	PSO J339.6104-13.7396	5	73	20.94	0.06	19.81	0.03	19.46	0.02	19.24	0.04	18.88	0.1
M223831.50-173119.1	348.8	<19.3	<16.0	⋯	1.831	SALT	Q						
	J223831.46-173117.7	339.6311027	−17.5215972	15.77	0.06	14.9	0.08	11.66	0.25				
	PSO J339.6310-17.5215	5	64	18.88	0.01	18.79	0.01	18.57	0.02	18.5	0.02	18.5	0.04
M224018.74+022030.0*c	211	<17.0	<15.8	⋯	0.694	SALT	Q						
	J224018.90+022028.5	340.0787841	2.3412684	15.63	0.05	14.98	0.09	11.16	0.21				
	PSO J340.0781+02.3415	5	75	19.7	0.05	19.41	0.02	19.34	0.02	19.08	0.04	19.17	0.05

Table 1
(Continued)

NVSS ID (1)	Flux WISE ID PS1 ID (2) (9) (18)	B_{maj} R.A.$_W$ nStackDets (3) (10) (19)	B_{min} Decl.$_W$ nDetections (4) (11) (20)	B_{pa} W1 g (5) (12) (21)	Redshift δW1 δg (6) (13) (22)	Telescope W2 r (7) (14) (23)	AGN-type δW2 δr (8) (15) (24)	W3 i (16) (25)	δW3 δi (17) (26)	z (27)	δz (28)	y (29)	δy (30)
M224111.48-244239.0	211.4	<16.7	<15.3	···	2.242	SALT	Q						
	J224111.50-244238.3	340.2979416	−24.7106643	15.54	0.05	14.44	0.06	11.03	0.14				
	PSO J340.2980-24.7107	5	89	18.8	0.04	18.47	0.01	18.58	0.01	18.44	0.01	18.41	0.02
M224354.81+181445.9	1004.4	<17.9	<16.5	···	0.760	NOT	G						
	J224354.81+181444.6	340.9784026	18.2457301	15.94	0.05	14.48	0.05	10.34	0.08				
	PSO J340.9785+18.2457	5	53	21.07	0.02	20.29	0.01	20.08	0.02	18.93	0.03	20.04	0.03
M224705.52+121151.4	223.7	<16.9	<16.7	···	2.185	NOT	Q						
	J224705.55+121151.8	341.7731632	12.1977348	17.27	0.14	16.66	···	12.25	···				
	PSO J341.7731+12.1976	5	35	21.43	0.05	21.22	0.06	21.03	0.01	20.55	0.09	20.7	0.17
M224950.57-263459.6	228.8	<16.3	<15.8	···	2.174	SALT	Q						
	J224950.57-263459.5	342.4607113	−26.5832163	16.23	0.07	15.26	0.09	12.06	0.38				
	PSO J342.4607-26.5832	5	61	20.23	0.02	20.04	0.05	19.98	0.03	19.58	0.02	19.42	0.07
M225137.19-331056.9	515.3	14	<16.9	−47.5	0.624	SALT	Q						
	J225137.20-331058.0	342.9050396	−33.1827883	15.15	0.04	14.46	0.05	10.93	0.11				
M225236.48-030551.4	240.1	<16.5	<14.8	···	1.633	SALT	Q						
	J225236.46-030550.4	343.1519288	−3.0973526	16.18	0.07	14.91	0.09	11.22	···				
	PSO J343.1519-03.0973	5	75	19.7	0.03	19.66	0.08	19.31	0.04	19.25	0.03	19.1	0.09
M230036.41+194002.9	210.4	14.9	<16.1	−29.6	2.160	NOT	Q						
	J230036.35+194001.3	345.1514973	19.6670443	15.94	0.06	15.22	0.09	12.19	0.4				
	PSO J345.1515+19.6671	5	64	19.63	0.02	19.58	0.01	19.36	0.02	19.12	0.02	19.05	0.02
M230040.87+033710.3	509	<17.3	<15.3	···	1.861	SUGAR	Q						
	J230040.89+033710.8	345.1703754	3.6196709	15.54	0.05	14.45	0.06	10.89	0.13				
	PSO J345.1704+03.6197	5	67	19.5	0.03	19.48	0.02	19.31	0.01	19.31	0.01	19.08	0.05
M230805.25-114945.7	256.8	<18.2	<16.3	···	1.940	NOT	Q						
	J230805.22-114945.2	347.0217611	−11.8292281	16.66	0.1	15.9	0.22	12.07	···				
	PSO J347.0218-11.8292	5	58	20.37	0.02	20.29	0.03	20.18	0.02	19.98	0.03	19.79	0.1
M231002.89+111403.6	248.1	<16.8	<16.3	···	1.550	NOT	Q						
	J231002.90+111404.6	347.512118	11.2346199	16.55	0.08	15.39	0.11	12.12	···				
	PSO J347.5121+11.2346	5	70	19.69	0.01	19.77	0.03	19.51	0.02	19.38	0.03	19.46	0.04
M231634.61+042940.2	214	<19.0	<16.6	···	2.180	SUGAR	Q						
	J231634.61+042939.8	349.1442147	4.4943985	15.72	0.05	14.46	0.06	11.15	0.16				
	PSO J349.1442+04.4944	5	78	19.35	0.01	19.2	0.03	18.89	0.04	18.62	0.01	18.65	0.03
M233231.61-142318.8	234.1	25.5	16	−46.8	0.524	NOT	Q						
	J233231.76-142320.7	353.132351	−14.3890852	14.79	0.03	14.1	0.05	11.06	0.16				
	PSO J353.1324-14.3891	10	47	20.97	0.05	20.28	0.04	19.64	0.02	19.53	0.07	19.32	0.02
M233808.04-121851.4	450.9	14.9	<16.5	6.4	1.185	NOT	Q						
	J233808.06-121850.5	354.5336244	−12.3140449	16.01	0.06	15.04	0.08	11.81	0.24				
	PSO J354.5336-12.3141	5	57	19.95	0.02	19.45	0.04	19.44	0.01	19.37	0.02	19.26	0.05
M234159.52-400856.2	460.7	<15.2	<13.9	···	0.562	SALT	Q						
	J234159.50-400854.4	355.4979212	−40.1484663	14.8	0.03	14.02	0.04	10.93	0.1				
M234207.38-092346.5	451.2	<19.5	<16.6	···	1.723	SALT	Q						
	J234207.43-092346.4	355.5309878	−9.3962396	15.69	0.05	14.46	0.06	10.99	0.14				
	PSO J355.5310-09.3962	5	40	21.6	0.07	21.48	0.09	20.7	0.03	20.45	0.03	19.99	0.03
M234910.12-043803.2	206.1	<16.4	<16.2	···	2.240	SALT	Q						
	J234910.16-043803.2	357.2923581	−4.6342274	15.77	0.05	14.99	0.09	11.61	0.29				
	PSO J357.2924-04.6343	5	72	18.68	0.01	18.76	0.01	18.6	0.01	18.43	0.01	18.37	0.02

Table 1
(Continued)

NVSS ID	Flux	$B_{\rm maj}$	$B_{\rm min}$	$B_{\rm pa}$	Redshift	Telescope	AGN-type						
	WISE ID	R.A.$_W$	Decl.$_W$	W1	δW1	W2	δW2	W3	δW3				
	PS1 ID	nStackDets	nDetections	g	δg	r	δr	i	δi	z	δz	y	δy
(1)	(2)	(3)	(4)	(5)	(6)	(7)	(8)						
	(9)	(10)	(11)	(12)	(13)	(14)	(15)	(16)	(17)				
	(18)	(19)	(20)	(21)	(22)	(23)	(24)	(25)	(26)	(27)	(28)	(29)	(30)
M235722.47-073134.3	235.5	<16.9	<15.9	⋯	2.764	SALT	Q						
	J235722.56-073134.1	359.3440369	−7.5261639	16.24	0.07	15.62	0.17	12.28	0.47				
	PSO J359.3438-07.5261	5	79	19.97	0.03	19.58	0.01	19.38	0.01	19.41	0.02	19.21	0.03
No emission lines (26)													
M001053.65-215703.9	387.8	<18.9	<16.3	⋯	⋯	SALT							
	J001053.64-215704.2	2.7235144	−21.9511886	14.8	0.03	13.79	0.04	10.57	0.08				
	PSO J002.7235-21.9512	5	43	21.07	0.05	20.38	0.06	20.11	0.06	20.01	0.16	19.72	0.07
M002232.46+060804.6	339.7	<17.7	<15.5	⋯	⋯	NOT							
	J002232.44+060804.2	5.6351816	6.1345179	13.23	0.03	12.21	0.02	9.03	0.03				
	PSO J005.6352+06.1345	5	83	18.45	0.04	18.52	0.02	18.54	0.06	18.1	0.03	17.9	0.07
M002945.04-174043.6	394.3	<19.5	<16.3	⋯	⋯	SALT							
	J002945.09-174042.4	7.4378894	−17.6784528	15.65	0.05	14.57	0.06	11.25	0.18				
	PSO J007.4379-17.6786	5	58	19.17	0.01	19.15	0.02	18.91	0.01	18.87	0.01	18.77	0.03
M005147.15+174710.3	1367.5	<17.9	<16.1	⋯	⋯	NOT							
	J005147.15+174710.4	12.9464982	17.786248	15.59	0.04	14.65	0.06	11.42	0.19				
	PSO J012.9465+17.7863	5	49	21.17	0.02	20.3	0.01	19.69	0.02	19.55	0.04	19.19	0.02
M010549.69+184507.1	339.5	<16.6	<15.2	⋯	⋯	NOT							
	J010549.66+184506.6	16.4569295	18.7518446	15.61	0.04	14.81	0.06	11.66	0.20				
	PSO J016.4569+18.7521	5	69	20.21	0.02	19.7	0.02	19.56	0.01	19.67	0.04	19.44	0.06
M055341.91-084003.3	273.8	<19.3	<13.9	⋯	⋯	SALT							
	J055341.91-084002.4	88.4246476	−8.6673536	15.78	0.05	14.75	0.07	11.55	0.18				
	PSO J088.4246-08.6672	20	0	23.21	0.16	22.04	0.08	21.15	0.03	21.19	0.08	20.63	0.11
M082444.81-102943.6	345.4	<16.0	<15.5	⋯	⋯	SUGAR							
	J082444.78-102943.4	126.1866017	−10.4954068	15.42	0.04	14.70	0.06	11.28	0.16				
	PSO J126.1867-10.4951	5	82	18.72	0.01	18.36	0.01	18.23	0.01	18.18	0.01	18.18	0.01
M085838.19+093745.2	421.5	<17.7	<17.3	⋯	⋯	SALT							
	J085838.21+093745.8	134.6592162	9.6293919	15.94	0.06	14.86	0.07	11.6	0.21				
	PSO J134.6591+09.6292	5	59	20.79	0.04	20.29	0.03	19.79	0.02	19.6	0.03	19.27	0.02
M110125.00-212429.4	215.3	<17.5	<14.0	⋯	⋯	SALT							
	J110125.01-212429.6	165.3542383	−21.4082386	16.21	0.06	15.52	0.116	11.95	⋯				
	PSO J165.3542-21.4083	31	7	−21.61	0.05	21.41	0.04	20.98	0.04	20.48	0.05	20.94	0.16
M111457.57-051721.4	325.7	<17.3	<14.3	⋯	⋯	SALT							
	J111457.53-051721.8	168.7397484	−5.2893949	17.81	0.23	16.06	0.20	11.96	0.31				
M112712.45-073512.7	459.5	14.6	<17.6	57.9	⋯	SALT							
	J112712.40-073512.2	171.8016899	−7.5867435	14.8	0.03	14.03	0.04	10.96	0.12				
	PSO J171.8018-07.5867	10	40	21.35	0.09	20.97	0.11	20.76	0.09	20.2	0.11	19.81	0.15
M120746.68-133201.0	203.2	<17.7	<17.1	⋯	⋯	SALT							
	J120746.69-133200.3	181.9445650	−13.5334438	17.34	0.16	16.42	0.26	12.08	⋯				
	PSO J181.9446-13.5335	5	37	21.14	0.07	20.6	0.1	20.48	0.07	20.21	0.05	19.95	0.12
M121157.77-192607.5	479.8	14.0	<17.2	63.2	⋯	SALT							
	J121157.73-192607.7	182.9905819	−19.4354923	15.89	0.05	15.1	0.08	11.89	0.33				
	PSO J182.9906-19.4355	5	39	−999	−999	21.47	0.05	20.67	0.03	20.27	0.05	−999	−999
M124553.81-161645.2	516.2	<17.2	<16.7	⋯	⋯	SALT							
	J124553.74-161645.7	191.4739578	−16.2793658	15.13	0.04	13.99	0.04	10.56	0.09				
	PSO J191.4739-16.2794	5	66	20.66	0.05	20.2	0.05	20.03	0.06	19.58	0.03	19.28	0.08
M130508.50-285042.0	328.4	<17.0	<15.8	⋯	⋯	SALT							
	J130508.44-285041.8	196.2851755	−28.8449497	16.05	0.05	15.05	0.07	11.81	0.21				
	PSO J196.2853-28.8450	5	7	22.15	0.07	21.69	0.18	−999	−999	21.05	0.07	−999	−999

Table 1

(Continued)

NVSS ID	Flux	$B_{\rm maj}$	$B_{\rm min}$	$B_{\rm pa}$	Redshift	Telescope	AGN-type						
	WISE ID	R.A.$_W$	Decl.$_W$	W1	δW1	W2	δW2	W3	δW3				
	PS1 ID	nStackDets	nDetections	*g*	δg	*r*	δr	*i*	δi	*z*	δz	*y*	δy
(1)	(2)	(3)	(4)	(5)	(6)	(7)	(8)						
	(9)	(10)	(11)	(12)	(13)	(14)	(15)	(16)	(17)				
	(18)	(19)	(20)	(21)	(22)	(23)	(24)	(25)	(26)	(27)	(28)	(29)	(30)
M131403.21+084209.5	267.1	<16.6	<16.3	···	···	SALT							
	J131403.18+084209.2	198.5132651	8.7025622	15.72	0.04	14.73	0.06	11.62	0.18				
	PSO J198.5133+08.7025	5	36	21.55	0.06	21.21	0.05	20.35	0.18	20.49	0.06	19.87	0.16
M135547.91-094756.5	322.7	<19.0	<15.9	···	···	SALT							
	J135547.87-094754.7	208.9494924	−9.7985281	17.72	0.21	16.35	0.25	12.33	···				
	PSO J208.9496-09.7987	5	38	21.73	0.05	21.4	0.03	21.06	0.06	20.83	0.09	20.04	0.16
M162422.33-301252.0	282.6	<15.5	<14.1	···	···	SALT							
	J162422.36-301251.8	246.0931921	−30.2143945	15.56	0.05	14.59	0.06	11.48	0.18				
M200429.50-101433.1	286.4	<18.5	<15.3	···	···	SALT							
	J200429.41-101432.1	301.1225449	−10.2422589	15.55	0.05	14.59	0.06	11.3	0.19				
	PSO J301.1225-10.2423	5	44	21.55	0.04	21.64	0.1	21.03	0.06	20.71	0.11	20.2	0.14
M214230.92-244440.1	290.5	<17.8	<17.0	···	···	SALT							
	J214230.94-244438.7	325.6289573	−24.7440982	14.75	0.03	13.84	0.04	10.71	0.11				
	PSO J325.6290-24.7441	5	79	21.02	0.06	20.36	0.04	19.29	0.02	19.28	0.11	19.31	0.09
M215720.05-360411.1	256.4	<18.8	<17.1	···	···	SALT							
	J215719.97-360412.8	329.3332138	−36.0702417	16.43	0.07	15.51	0.11	12.2	0.54				
M222359.11+121338.9	246.4	<16.1	<15.2	···	···	NOT							
	J222359.07+121339.1	335.9961626	12.2275338	15.05	0.04	13.99	0.04	10.76	0.15				
	PSO J335.9962+12.2275	5	47	21.48	0.17	21.14	0.04	20.61	0.03	20.2	0.07	19.88	0.1
M223240.99-144226.7	396.0	<17.2	<16.7	···	···	SALT							
	J223240.91-144227.4	338.1704879	−14.7076348	16.25	0.08	15.46	0.12	11.88	···				
	PSO J338.1706-14.7075	5	51	20.43	0.02	20.51	0.03	19.91	0.03	19.99	0.03	19.82	0.03
M224500.21-343030.0	396.6	<17.8	<16.9	···	···	SALT							
	J224500.08-343031.6	341.2503530	−34.5087858	15.0	0.03	14.33	0.05	10.89	0.10				
M233004.06-052447.7	303.5	<17.5	<17.0	···	···	SALT							
	J233004.05-052447.4	352.516875	−5.4131766	16.32	0.07	15.39	0.11	11.83	···				
	PSO J352.5168-05.4132	67	10	21.41	0.03	20.91	0.02	20.56	0.02	20.17	0.03	20.19	0.08
M233405.71-022517.8	219.1	<19.3	<17.1	···	···	SALT							
	J233405.72-022518.2	353.5238400	−2.4217257	16.48	0.08	15.48	0.12	11.92	···				
	PSO J353.5239-02.4215	5	26	21.83	0.02	21.62	0.13	21.07	0.05	21.08	0.04	−999	−999
Dark fields (27)													
M010253.16-120541.3	370.1	14.4	<16.3	25.1	···	SALT							
	J010253.22-120541.2	15.7217535	−12.0948007	16.76	0.10	16.04	0.20	11.99	···				
	PSO J015.7218-12.0948	1	0	22.99	0.17	23.25	0.16	22.82	0.13	23.54	0.61	22.51	0.55
M012156.62-265747.8	244	<18.2	<17.7	···	···	SALT							
	J012156.60-265747.7	20.485842	−26.9632715	16.75	0.09	15.68	0.12	11.89	···				
M051700.70+071225.2	203.4	<16.3	<14.9	···	···	SALT							
	J051700.70+071225.3	79.2529287	7.2070517	16.44	0.08	15.33	0.10	11.6	···				
	PSO J079.2529+07.2070	3	0	23.54	0.31	22.31	0.09	21.99	0.08	21.53	0.12	21.29	0.20
M064255.16-325917.6	240.6	<18.7	<16.2	···	···	SALT							
	J064255.14-325918.2	100.7297545	−32.9883921	16.17	0.05	14.86	0.05	11.19	0.11				
M084548.34-111800.1	264.4	<16.6	<16.4	···	···	SUGAR							
	J084548.25-111801.7	131.4510672	−11.300489	16.18	0.06	15.29	0.09	12.03	0.30				
	PSO J131.4512-11.3001	0	0	23.88	0.85	23.26	0.30	23.2	0.15	21.88	0.18	23.05	1.68

Table 1
(Continued)

NVSS ID	Flux	$B_{\rm maj}$	$B_{\rm min}$	$B_{\rm pa}$	Redshift	Telescope	AGN-type						
	WISE ID	R.A.$_W$	Decl.$_W$	W1	δW1	W2	δW2	W3	δW3				
	PS1 ID	nStackDets	nDetections	g	δg	r	δr	i	δi	z	δz	y	δy
(1)	(2)	(3)	(4)	(5)	(6)	(7)	(8)						
	(9)	(10)	(11)	(12)	(13)	(14)	(15)	(16)	(17)				
	(18)	(19)	(20)	(21)	(22)	(23)	(24)	(25)	(26)	(27)	(28)	(29)	(30)
M095414.75+125222.6	355.7	<17.3	<16.2	⋯	⋯	NOT							
	J095414.78+125222.5	148.5616137	12.8729286	16.95	0.13	15.74	0.143	11.79	⋯				
M095903.16-023604.5	269.1	<19.1	<16.6	⋯	⋯	SALT							
	J095903.12-023604.5	149.7630038	−2.6012773	16.75	0.10	15.61	0.129	12.12	⋯				
	PSO J149.7632-02.6013	6	0	23.76	0.23	22.80	0.13	21.98	0.07	21.76	0.08	22.15	0.49
M101448.67-294433.7	229	<16.8	<14.7	⋯	⋯	SALT							
	J101448.55-294433.5	153.7023142	−29.7426467	16.19	0.06	15.41	0.09	12.35	⋯				
M101730.54-384643.7	336.5	<18.7	<17.0	⋯	⋯	SALT							
	J101730.47-384643.8	154.3769644	−38.7788586	16.41	0.07	15.57	0.11	11.92	0.25				
M101838.68-222502.4	288.1	<17.9	<16.9	⋯	⋯	SALT							
	J101838.61-222501.9	154.6608814	−22.4172125	16.29	0.06	15.43	0.10	11.91	⋯				
M104015.57+062747.0	600.4	<18.4	<16.7	⋯	⋯	SALT							
	J104015.61+062745.9	160.0650746	6.4627552	17.32	0.17	16.42	0.273	11.96	⋯				
M110552.25-015628.1	477.5	26.6	<16.8	−76.3	⋯	SALT							
	J110552.18-015627.1	166.4674275	−1.9408789	15.49	0.04	14.45	0.05	10.73	0.101				
	PSO J166.4675-01.9408	11	1	22.29	0.07	22.10	0.07	21.61	0.08	21.35	0.08	21.42	0.26
M114450.43-145502.7	444	14.4	<16.9	57.1	⋯	SALT							
	J114450.42-145501.9	176.2100931	−14.9171983	16.05	0.06	15.45	0.137	12.27	⋯				
	PSO J176.2101-14.9172	3	0	23.45	0.25	23.01	0.12	22.09	0.07	21.44	0.11	20.94	0.14
M115855.48-170524.7	359.5	48.1	<16.6	75.2	⋯	SALT							
	J115855.44-170523.7	179.7310087	−17.0899371	16.41	0.07	15.40	0.12	12.10	0.42				
	PSO J179.7312-17.0901	2	1	22.74	0.15	22.47	0.11	23.14	0.32	22.39	0.24	22.18	0.31
M121128.51-351003.4	280.1	<16.4	<15.3	⋯	⋯	SALT							
	J121128.44-351002.5	182.8685401	−35.1673751	14.9	0.03	14.17	0.041	11.25	0.14				
M125203.09-040638.5	392.6	<18.7	<16.5	⋯	⋯	SALT							
	J125203.15-040638.4	193.01315	−4.1106828	16.69	0.09	16.02	0.19	12.45	⋯				
M131615.50-242824.1	234.7	<15.9	<15.3	⋯	⋯	SALT							
	J131615.51-242822.8	199.0646338	−24.4730071	16.56	0.07	15.90	0.14	12.50	0.36				
	PSO J199.0646-24.4733	0	0	22.77	0.13	22.61	0.13	22.51	0.13	22.79	0.32	21.48	0.23
M133621.59-105243.4	397.3	14.7	<16.7	50.5	⋯	SALT							
	J133621.66-105243.7	204.090252	−10.8788322	17.43	0.16	16.43	0.23	12.44	⋯				
M135150.53-243921.3	225.5	<18.0	<15.7	⋯	⋯	SALT							
	J135150.35-243920.1	207.9598266	−24.6555845	16.05	0.06	15.3	0.10	12.27	⋯				
	PSO J207.9601-24.6557	1	0	25.19	1.32	23.24	0.26	22.39	0.18	21.28	0.08	20.97	0.16
M140807.52+095348.1	261.9	<18.7	<15.3	⋯	⋯	SALT							
	J140807.50+095347.6	212.031289	9.8965777	16.27	0.06	15.43	0.10	12.41	0.36				
	PSO J212.0314+09.8964	1	0	25.18	1.30	25.19	1.11	23.60	0.28	21.99	0.14	21.60	0.27
M152601.27+071525.5	288.2	<16.4	<14.7	⋯	⋯	SALT							
	J152601.29+071525.2	231.5053995	7.2570161	17.42	0.14	16.46	0.23	12.35	0.31				
	PSO J231.5054+07.2570	0	0	25.64	1.55	23.43	0.29	23.34	0.19	23.46	0.41	25.87	9.37

Table 1

(Continued)

NVSS ID (1)	Flux WISE ID PS1 ID (2) (9) (18)	B_{maj} R.A.$_W$ nStackDets (3) (10) (19)	B_{min} Decl.$_W$ nDetections (4) (11) (20)	B_{pa} W1 g (5) (12) (21)	Redshift δW1 δg (6) (13) (22)	Telescope W2 r (7) (14) (23)	AGN-type δW2 δr (8) (15) (24)	W3 i (16) (25)	δW3 δi (17) (26)	z (27)	δz (28)	y (29)	δy (30)
M154044.18-145528.3	313.1	<16.9	<16.1	⋯	⋯	SALT							
	J154044.17-145529.7	235.1840445	−14.9249201	16.94	0.13	16.12	0.24	11.72	⋯				
M164548.19-121024.8	386.1	<16.6	<16.0	⋯	⋯	SALT							
	J164548.18-121025.3	251.4507554	−12.1736957	16.46	0.09	15.59	0.13	12.03	⋯				
	PSO J251.4509-12.1734	2	0	25.70	1.61	23.29	0.24	22.17	0.07	21.19	0.07	20.90	0.14
M195302.23-203633.0	516.4	<18.6	<17.0	⋯	⋯	SALT							
	J195302.24-203631.7	298.2593374	−20.6088241	16.68	0.10	15.61	0.17	12.29	⋯				
M204439.43-182852.2	219.5	<17.7	<16.5	⋯	⋯	SALT							
	J204439.40-182851.4	311.1641793	−18.4809453	16.42	0.08	15.38	0.107	12.12	⋯				
	PSO J311.1644-18.4812	4	0	−999.0	−999.0	22.63	0.10	22.18	0.05	21.87	0.13	−999.0	−999.0
M211410.44-105558.3	280.3	<17.5	<16.1	⋯	⋯	SALT							
	J211410.40-105557.6	318.5433725	−10.93268	16.51	0.09	15.76	0.16	12.21	⋯				
	PSO J318.5431-10.9326	0	0	−999.0	0.65	24.06	0.67	23.64	0.26	22.24	0.18	23.02	1.10
M225813.47-095817.2	225.7	<19.7	<16.5	⋯	⋯	SUGAR							
	J225813.45-095816.7	344.5560625	−9.9713208	17.37	0.17	16.52	0.34	12.19	⋯				

Note. Column 1: NVSS ID based on R.A. and decl. (J2000); M stands for MALS SALT-NOT survey. Column 2: 20 cm flux density from NVSS. Columns 3–5: deconvolved radio sources size from NVSS (major and minor axes in arcseconds, and position angle in degrees). Column 6: spectroscopic redshift based on SALT-NOT spectra. Column 7: telescope used for spectroscopy. SUGAR = observed with both SALT and NOT. Column 8: AGN type (G or Q corresponding to NLAGN or BLAGN). Columns 9–17: WISE ID and W1, W2, and W3 magnitudes (mag) with errors. Columns 18–30: PS1 ID, number of stack detections, number of single epoch detections in all filters, and g, r, i, z, and y magnitudes with errors from PS1 mean for sources with redshifts and ELLs, and PS1 stack for DFs.

List of targets excluded from the NOT sample presented in Table 1 of Krogager et al. (2018): M024944.50+123706.3, M051938.34+174641.2, M163906.46+114409.2, M162303.03+123958.4, M060012.92-071037.9, M162539.34-041616.3, and M172423.07+032632.5 (see also Section 2.2).

(This table is available in its entirety in machine-readable form.)

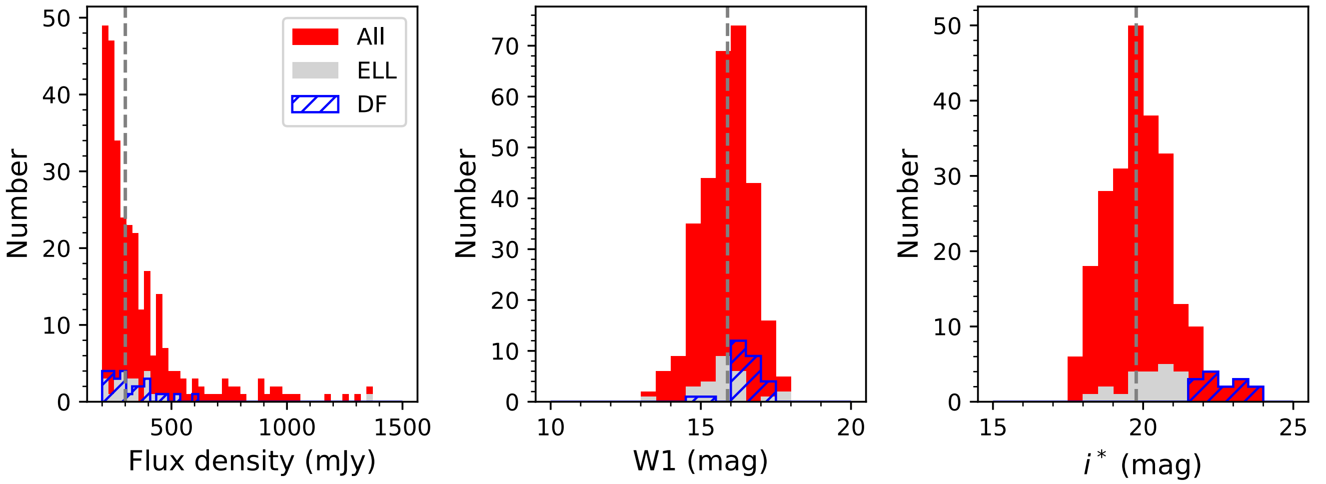

Figure 3. Distribution of flux density at 1.4 GHz, W1 and i mag for our MIR-selected sample. The gray and blue-hashed distributions show objects with no clear emission lines (ELLs) and objects with no detected spectrum (DF), respectively. The vertical dashed lines mark the median for all the sources in each panel. In the first panel, four targets brighter than 1500 mJy are out of frame. Note that for DFs, the i-band magnitudes are from the more sensitive PS1 stack catalog (Waters et al. 2020).

For this purpose, we compile a highly complete spectroscopic sample of 10,498 quasars from the SDSS (DR16) in the so-called *Stripe 82* region where the spectroscopic completeness is the highest in SDSS. We then crossmatch this sample with the AllWISE catalog to produce our optical comparison sample. We note that although no radio flux density limits have been applied here, only 347/10,498 are detected in FIRST, and only seven of these are brighter than 200 mJy. We will ignore this distinction in our statistical analysis.

We first check the effect of requiring detections in all three WISE bands used in our criteria. We find that out of the 10,498 quasars, only 56% have WISE photometry in all three bands. Overall, the quasars *with* WISE detections are brighter and have slightly redder colors compared to the quasars without WISE detections in all three bands. The median i-band brightness is 19.9 and 20.4 mag for quasars with and without WISE detections, respectively, and the median $g - i$ color differs by 0.034 mag (Figure 4). When restricting the color comparison to quasars with the same brightness ($i < 20$ mag), the color difference diminishes to 0.023 mag, i.e., at the order of the photometric uncertainty.

The average redshift of quasars with WISE detections is lower ($\langle z \rangle = 1.48$) than quasars without WISE detections ($\langle z \rangle = 1.86$), which is in line with the brighter i-band magnitudes for quasars with WISE detections. Yet, there are no significant color differences as a function of redshift.

The next step is to quantify the effect of our WISE color criteria. We use the same optical comparison sample as defined above to check the optical brightness and colors of those quasars that meet the criteria in Equation (1) and those that do not. Our WISE criteria have been designed to reduce the number of $z < 1.4$ quasars, and as shown in Figure 2, our sample effectively reduces the number of low-redshift quasars. Due to the largely different redshift distributions, it is not surprising to find that the quasars that follow Equation (1) are 0.4 mag fainter on average. Considering only quasars at $z > 2$, the quasars that follow our WISE criteria Equation (1) are on average only 0.2 mag fainter. We find no significant difference in optical color between quasars that meet our criteria and those that do not.

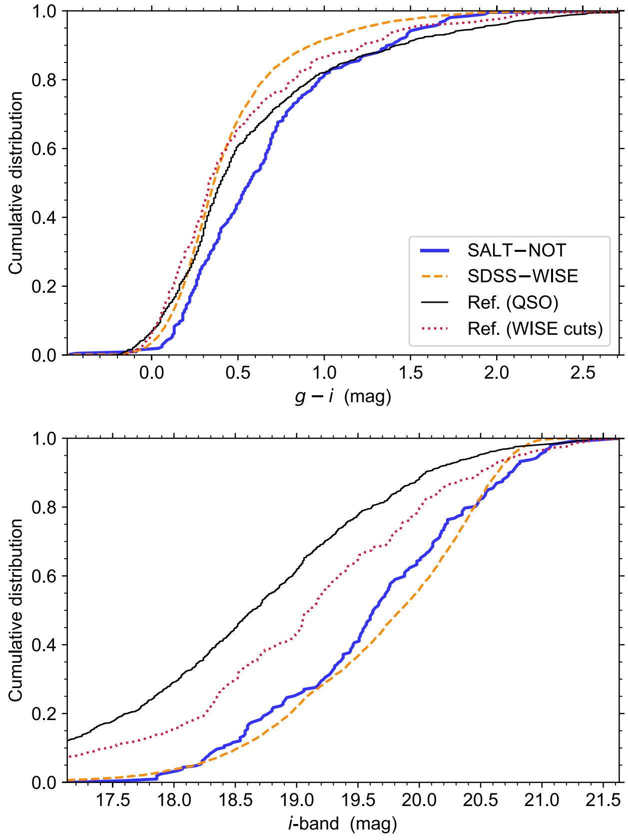

Figure 4. Comparison of the MALS SALT-NOT sample (blue, thick line) with the full quasar reference sample (black, thin line), the quasar reference sample that fulfills Equation (1) red-dotted line), and the SDSS+WISE quasar comparison sample (orange-dashed line).

Lastly, we compare the SALT-NOT sample with the reference sample of quasars as well as the optically selected SDSS quasar sample. In Figure 4, we show the cumulative distributions of $g - i$ color and i-band brightness. We find that the SALT-NOT sample has on average redder colors than the other samples, with the optically selected sample showing the bluest colors. The median color difference is 0.2 mag. On the other hand, the SALT-NOT sample is fainter than the reference quasar sample and shows a distribution of optical brightness similar to the SDSS quasar sample.

In conclusion, we find that our imposed WISE criteria result in a sample of radio-bright quasars that is fainter and slightly redder than radio-selected (reference) quasars. Part of this difference in color and brightness can be attributed to the difference in the respective redshift distributions. Nonetheless, our sample is representative in terms of redder optical colors commonly observed in radio-selected samples while probing fainter quasars more representative of deep, optically selected samples.

3. Observations and Data Analysis

We observed 255 and 99 targets with SALT and NOT, respectively. Of these, 40 targets, labeled as SUGAR (NOT-SALT) in Column 7 of Table 1, are common to both the sub-surveys. In this section, we present details of SALT observations and data analysis. The corresponding details for NOT observations carried out in 2016 August (`P53-012`) and 2017 February (`P54-005`; PI: Krogager) are presented by Krogager et al. (2018).

We used the Robert Stobie Spectrograph (RSS; Burgh et al. 2003; Kobulnicky et al. 2003) on SALT to obtain optical spectra of 255 targets. These service mode observations were carried out between 2014 November and 2017 April through the programs: `2014-2-SCI-027`, `2015-1-SCI-012`, `2015-2-SCI-030`, `2016-1-SCI-022`, and `2016-2-SCI-17` (PI: N. Gupta). Each observing block typically contained two ∼10 minute science exposures, in the long-slit mode having a slit width of 2″. We note that the calibration lamp and the flat-field images required for the wavelength calibration and flat-fielding were obtained separately, as part of `2015-1-SCI-012`. The detector in RSS consists of a mosaic of three CCDs with a total size of 3171×2052 pixels. The pixel size is 15 μm which corresponds to a spatial sampling of 0.″1267 per pixel. We opted for 2×2 pixel binning to improve the signal-to-noise ratio (S/N). We used RSS PG0900 grating with a grating tilt angle of 15.875°. This provides a wavelength coverage of 4486–7533 Å, but with gaps at 5497–5551 and 6542–6589 Å. The resulting spectral resolution is $R = 1064$ at 6041 Å. The observations were performed on clear nights with a median seeing of ∼1.″5. The fainter targets were assigned higher priority for observations on dark and gray nights.

The preliminary data reduction, i.e., gain correction, overscan bias subtraction, cross-talk correction, and amplifier mosaicing were performed by the SALT observatory staff using the semiautomated pipeline PySALT,[18] the Python/PyRAF software package for SALT data reduction (Crawford et al. 2010). Using IRAF[19] packages, we further removed cosmic-rays and applied the flat-field correction. The wavelength calibration was performed using an xenon arc lamp and the spectrophotometric standard star L377 was used for flux calibration. We extracted 1D spectra from individual exposures after subtracting the background. We also corrected the 1D spectra for atmospheric extinction and applied the air to vacuum correction to the wavelengths. The final 1D spectra of the quasars used for analysis is the combination of all the available exposures (typically ∼20 minutes on-source).

4. Spectral Analysis

We visually examined all the spectra for the presence of emission lines. In Figure 5, we show five representative SALT spectra. These represent: low-z ($z < 1.0$; top two panels), intermediate-z ($1.0 < z < 1.9$; middle panel), high-z ($z > 1.9$; second panel from the bottom), and the ELLs (bottom panel) AGN. Flux scale for each spectrum is corrected for slit losses using the PS1 photometry. Here, we have ignored the possibility of continuum variability between our spectra and the PS1 observations.

For the spectra exhibiting two or more emission lines, the line identifications are robust, and hence the redshifts estimated are also correct within the wavelength uncertainty. However, the line identification is more challenging in the cases with very faint trace/emission lines or with only single emission line detection (see second panel from the top in Figure 5, for example). For such sources the identification is based on line widths, expected relative strengths and the absence of other lines within the observed wavelength range. We also used various AGN (QSO, Seyfert1, and Seyfert2) templates from the literature[20] to aid the process of line identification.

After line identification, we used peaks of prominent lines, i.e., Lyα for $z > 2.66$, C IV for $1.87 < z < 3.86$, Mg II for $0.58 < z < 1.69$, C III for $1.328 < z < 2.938$, [O II] for $0.19 < z < 1.01$, and [O III] and Hβ for $z < 0.50$, to measure the redshifts. The rest wavelengths are taken from the SDSS emission line list.[21] In the cases where the peak of the prominent emission line is affected by absorption or it falls in the CCD gap, we fit the emission line avoiding these regions and take the centroid of the fit to estimate the redshift. The overall uncertainty in redshift (Δz) that is introduced due to wavelength calibration issues and uncertainty in measuring the peak is roughly $\Delta z \approx 0.005$.

The redshift distribution of all the AGN (250) with emission line identifications is shown in Figure 6. In 32 cases the redshift is based on a single emission line assumed to be C IV, C III, Mg II, [O II], or Lyα. In Table 1, these are marked with *a, *b, *c, *d, and *f, respectively. In 26 cases, no emission lines (i.e., ELLs) are detected in the spectra. In 27 cases, no continuum or emission lines are detected (i.e., DFs).

5. Results

The properties of the SALT-NOT sample consisting of 250 quasars with emission lines, 26 ELLs, and 27 DFs are provided in Table 1. In this section, we present selected results based on continuum and emission lines detected in our optical spectra. It is well beyond the scope of this paper to discuss all the aspects in detail. Hence, we present overall properties of the observed sample and comparison with the reference sample in Section 5.1. This is followed by short overviews of AGN detected at $z < 3.5$ in Sections 5.2–5.5 on the basis of different groups of observable emission lines. For AGN at $z < 1.9$, we discuss only the fraction of narrow emission line objects (type II quasars or radio galaxies) found in different redshift intervals and the morphology of

---

[18] http://pysalt.salt.ac.za

[19] IRAF is distributed by the National Optical Astronomy Observatories, which are operated by the Association of Universities for Research in Astronomy, Inc., under cooperative agreement with the NSF.

[20] https://archive.stsci.edu/hlsps/reference-atlases/cdbs/grid/agn

[21] http://classic.sdss.org/dr6/algorithms/linestable.html

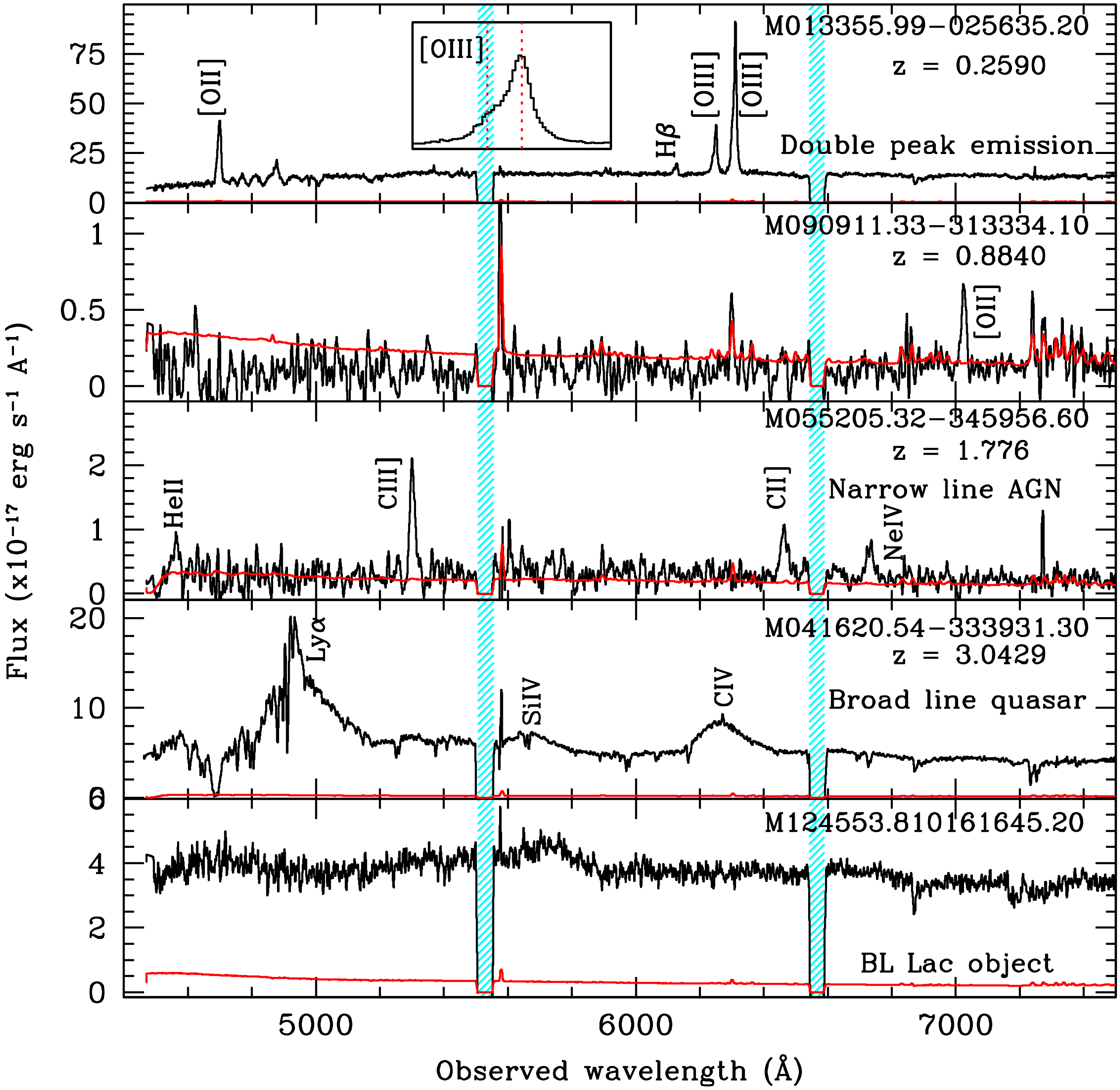

Figure 5. Spectra of five representative AGN from our sample at increasing redshifts from top to bottom. Different emission lines based on which the redshift was determined are identified. All the spectra are smoothed by 3–7 pixels for visual clarity. The error spectra are shown in red in each panel. The hashed regions mark the spectral range falling in the CCD gaps. Inset in the top most panel shows the double peak [O III]λ5007 profile. In the bottom panel an example of AGN without detectable emission lines is shown. We use photometric variability to identify such objects as BL Lacs (see Section 5.7).

associated radio emission. For quasars at $1.9 < z < 3.5$, we also present the distribution of BH masses and the fraction of BAL quasars. The farthest narrow-line AGN (NLAGN) in our sample is M1513-2524 ($z_{\rm em} = 3.132$), and the one with largest projected linear size of radio emission (size ∼330 kpc) is M0909-3133 ($z_{\rm em} = 0.884$). For some individual objects the details, such as the morphology of associated radio emission, host galaxy, and emission line properties, relevant to the discussion presented in these sections are provided in Appendix B. The properties of M1312-2026, the potential highest redshift AGN in the sample, are discussed in Section 5.6. In Sections 5.7 and 5.8, we discuss AGN with no optical emission lines and dark fields, respectively.

5.1. Overall Properties

The basic properties, i.e., redshift, W1- and *i*-band magnitudes of the SALT-NOT sample are summarized in Figure 7. We have also used emission lines detected in our spectra to classify objects as NLAGN or broad-line AGN (BLAGN). In Table 1, these are labeled as “G” and “Q”, respectively. In total, 51/250 objects are NLAGN and 33 of these are at $z < 0.5$. As expected the fraction of NLAGN in our sample falls off at higher redshifts.

Figure 7 also provides a comparison with the reference sample of quasars satisfying our MIR cut (see Section 2.1). The median redshift of the SALT-NOT sample is only slightly lower but a deficit of lower redshift AGN in the reference

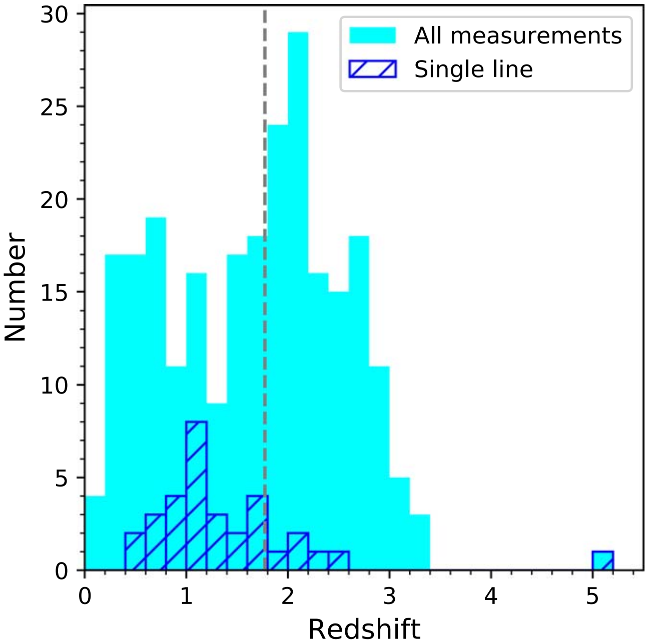

Figure 6. Redshift distribution for all the SALT-NOT targets with spectroscopic redshifts. The vertical dashed lines mark the median value. The distribution of redshifts based on single emission line (blue-hashed histogram) is also shown. The redshifts based on a single emission line should be treated with caution. The correct redshift of AGN marked at $z \sim 5$ is $z = 0.977$ (see Section 5.6 for details).

sample is apparent. A two-sample Kolmogorov–Smirnoff (K-S) test shows that there is a less than 1 percent chance (p-value = 0.008) that the two samples are different purely by chance. Related to this, we also note that in the SALT-NOT sample, 20 ± 3% objects are NLAGN, whereas based on the reference sample only $6^{+2.1}_{-1.6}\%$ are expected.

In Figure 7, we also compare W1- and i-band magnitudes of the two samples. Clearly, the SALT-NOT sample corresponds to a population of fainter AGN. We note that the probabilities of two samples being drawn from the sample populations are 1.7×10^{-4} for W1 brightness and 1.6×10^{-8} for i-band brightness. This further confirms the assertion made in Section 2.3 that the inclusion of W3, the less sensitive WISE band, in our target selection has not biased our sample toward brighter objects. In particular, the i-band magnitudes of AGN in our sample at $z < 0.5$ and $z > 0.5$ are similar. Therefore, the excess of NLAGN at $z < 0.5$ in our sample is intriguing. It is likely a direct consequence of the selection of optically fainter targets through MIR color selection. Excluding these $z < 0.5$ NLAGN renders the z-distributions of the SALT-NOT sample and the reference sample statistically identical.

5.2. *AGN at* z < *0.5*

For $z < 0.5$ AGN, our SALT spectra cover the [O II], [O III], and Hβ emission lines. The NOT spectra cover the Mg II emission line as well. Overall, the SALT-NOT sample has 33/303, i.e., 11% AGN in our sample are at $z < 0.5$. We find the spectra in all the 33 cases to be mostly dominated by narrow permitted emission lines (with FWHM <2000 km s^{-1}). The available optical images are also consistent with their hosts being galaxies with weak or no nuclear emission. Compared to this, in the reference sample (SDSS), only ∼32% (6/19) of the $z < 0.5$ AGN satisfying our MIR wedge are classified as galaxies. As mentioned above, this difference with respect to the reference sample is most likely due to the optical faintness of the SALT-NOT sample and the specific goal to reject low-redshift AGN (Barrows et al. 2021).

The radio emission associated with these NLAGN is often extended, the largest projected linear size being ∼250 kpc (details in Appendix B). An examination of optical emission lines led to identification of two dual AGN showing double peaked spectra (an example is shown in top panel of Figure 5; more details in Appendix B). Our detection rate of $6^{+8}_{-4}\%$ is marginally higher, but only at 1σ, than the detection rate (1%) of dual AGN in SDSS (Liu et al. 2010).

5.3. *AGN at 0.5* < z < *1.0*

For AGN at $0.5 \leqslant z \leqslant 1.0$ (35/303), the SALT-NOT spectra cover both the Mg II and [O II] emission lines. About $32^{+13}_{-10}\%$ (12/35) of these show emission lines of [O II], Ne IV, and Ne V without (or narrow) Mg II broad emission lines. The fraction of NLAGN (8/28 i.e., $29^{+14}_{-9}\%$) is consistent with the reference sample.

In VLASS 3 GHz images, 8/12 ($75^{+25}_{-23}\%$) of the NLAGN in the SALT-NOT sample exhibit extended radio emission with lobes, the largest projected linear size being 330 kpc. Among BLAGN, as expected, a much smaller fraction (∼40%) is associated with extended radio emission (Padovani et al. 2017; Hickox & Alexander 2018). The largest extent is only 180 kpc (see Appendix B for details). We also examined the radio morphology and optical emission line profiles for evidence of interaction between radio jet and the host galaxy emission (see, e.g., Mullaney et al. 2013). In three cases, the radio morphology is distorted. But only in one of these (details in Appendix B), the [O II] line is asymmetric, which may be an indication of radio jet-interstellar medium interaction (e.g., Gupta et al. 2005).

5.4. *AGN at 1.0* < z < *1.9*

At $1.0 \leqslant z \leqslant 1.9$, our sample has 71 AGN. Only two of these are possibly NLAGN and the radio emission in both the cases has a double-lobed morphology (details in Appendix B). This low fraction (3%; 2/71) of NLAGN is consistent with the reference sample, which has 0/53 such AGN in this redshift range.

5.5. *AGN at 1.9* < z < *3.5*

As previously mentioned, for these redshifts the SALT-NOT spectra of 110 AGN in our sample allow detection of C IV emission lines. Based on the width of C IV emission line (i.e FWHM < 2000 km s^{-1}) we identify four of these objects to be the NLAGN. In comparison, the reference sample has no NLAGN (0/128) at $z > 1.9$, which is consistent at 2σ considering one-sided Poissonian statistics. The details of NLAGN at $1.9 < z < 3.5$ in our sample are provided in Appendix B. The emission line ratios are typical of what is observed in high-z radio galaxies. Two of these, i.e., M1315-2745 and M1513-2524 are among the largest radio galaxies at these redshifts (see Figure 13 of Shukla et al. 2021, for the latest compilation). In the rest of this section, we discuss BH masses, Eddington ratios, and BALS associated with the BLAGN.

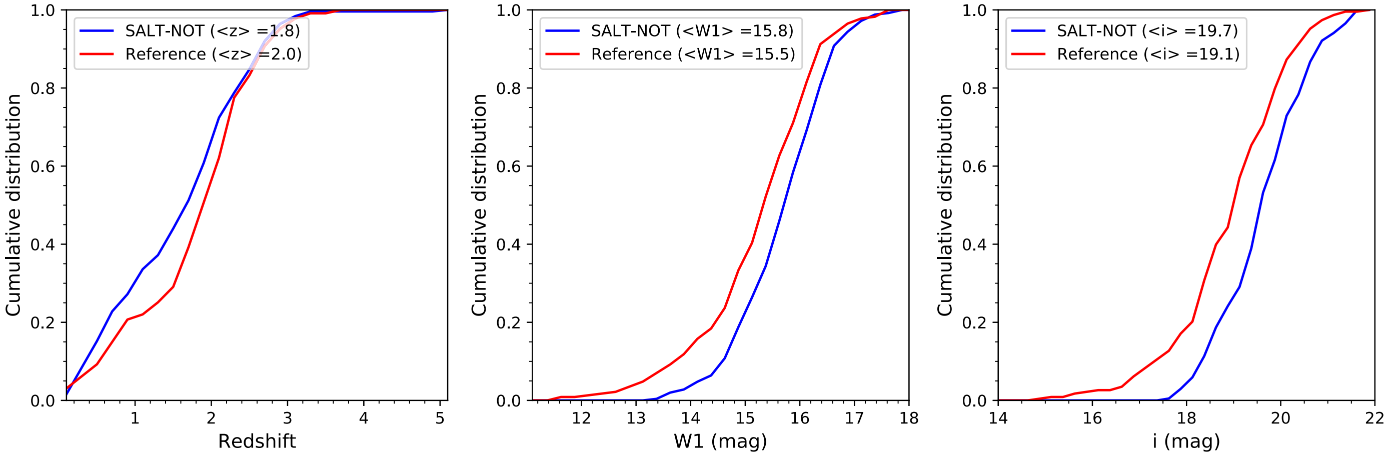

Figure 7. Comparison of our SALT-NOT sample and the subset of the reference sample satisfying our WISE criteria. The median values are also provided.

5.5.1. BH Masses and Eddington Ratios

Under the assumption that broad-line region (BLR) clouds are in virial equilibrium, the mass of the BH, $M_{\rm BH}$, is given by

$$M_{\rm BH} = f\ \frac{R_{\rm BLR}\ {\rm FWHM}^2}{G}, \tag{2}$$

where G is the gravitational constant and f is the virial coefficient that depends on the geometry and kinematics of the BLR. The radius of the BLR, $R_{\rm BLR}$, is generally estimated using empirical relations between continuum or line luminosity (e.g., Kaspi et al. 2000). The value of f is also empirically determined (e.g., Onken et al. 2004). Following Shen et al. (2011), we estimate virial BH masses for quasars with the C IV emission line using a relation of the form

$$\log\left(\frac{M_{\rm BH}}{M_\odot}\right) = a + b\ \log(\lambda L_\lambda) + 2\ \log({\rm FWHM}), \tag{3}$$

where a and b are calibrated from reverberation mapping for a particular emission line (e.g., Denney et al. 2010). The broad-line FWHM is in kilometers per second and the continuum luminosity, λL_λ, which is a proxy for R_{BLR}, is in units of 10^{44} erg s^{-1}. We adopt $a = 0.660$ and $b = 0.53$ for Equation (3) based on the empirical relationship provided by Vestergaard & Peterson (2006) to estimate the BH mass for our sample.

Further, to place our SALT-NOT sample in the broader context of the overall quasar population, we compare our measurements to the compilation of 105,783 SDSS DR7 quasars provided by Shen et al. (2011). For direct comparability of the measurements, we largely follow the method of Shen et al. (2011) to measure C IV FWHM and λL_λ at 1350 Å. In short, we fit a power law to the continuum in the rest wavelength ranges of 1445–1465 and 1700–1705 Å. Prior to continuum fitting we mask any unwanted spikes stronger than 5σ. Then, we fit the continuum subtracted emission line in the wavelength range 1500–1600 Å using three Gaussians. The FWHM of the emission line, referred to as the *full* line FWHM, is then estimated from the fit after rejecting any individual components with strength <5%. The continuum luminosity at 1350 Å (L_{1350}) is estimated using the same power law used to fit the continuum underlying the C IV emission line. We are able to reliably estimate full C IV line FWHM, continuum luminosity at 1350 Å and BH mass of 86/110 quasars ($z > 1.9$) from our sample. We have excluded 24 AGN with low S/N profiles or lines affected by the CCD edge. Similar to Shen et al. (2011), the bolometric luminosity ($L_{\rm Bol}$) have been estimated by applying the bolometric correction factor of 3.81 to L_{1350} (Richards et al. 2006). The Eddington ratio ($\lambda_{\rm Edd}$) is estimated as $L_{\rm Bol}/L_{\rm Edd}$, where $L_{\rm Edd}$ is the Eddington luminosity.

The compilation of Shen et al. (2011) consists of 11,840 non-BAL quasars at $1.9 < z < 3.5$ (median $z = 2.29$), the redshift range covered by our sample (median $z = 2.34$). We have restricted the sample of Shen et al. (2011) to the subset that has been identified by a uniform target selection algorithm and flux limited to $i = 19.1$ at $z < 2.9$ or $i = 20.2$ at $z > 2.9$ (Richards et al. 2002). A distinguishing feature of the SALT-NOT sample is the high radio brightness of quasars. In particular, the $z > 1.9$ quasars in SALT-NOT sample have predominantly flat radio spectra. The median spectral index,[22] $\alpha_{0.4}^{1.4}$, derived using the NVSS 1420 MHz and the uGMRT 420 MHz total flux densities is ~ -0.38 (Gupta et al. 2021b). In the uGMRT images, 79/88 of these are represented by a single Gaussian component. Therefore, we further restrict the sample of Shen et al. (2011) to 786 core-dominated quasars, hereafter Shen11-core in short, detected in FIRST.

In left panel of Figure 8, we show the distributions of full C IV FWHM and 1350 Å luminosity for SALT-NOT and Shen11-core quasars. The SALT-NOT sample extends about 0.5 dex fainter in 1350 Å luminosity. The two-sample K-S test probability of these two samples being drawn from the same parent sample is extremely small (p-value $= 4 \times 10^{-13}$). The C IV FWHM of the SALT-NOT sample (median FWHM = 4445 km s^{-1}) is marginally smaller than the Shen11-core sample (median FWHM = 4660 km s^{-1}), and this difference is statistically insignificant. We note that if the C IV profiles are affected by non-virial motions such as outflows (Coatman et al. 2016), the influence ought to be similar in both the samples. Due to the luminosity dependence of $\lambda L_\lambda^{0.66}$ in the virial mass estimator, the overall BH masses estimated using Equation (3) are lower for the SALT-NOT sample (see right panel of Figure 8). The K-S test probability of two $M_{\rm BH}$ distributions being drawn from the same parent sample is extremely small (p-value $= 3 \times 10^{-5}$; see the left panel of Figure 9).

In the middle panel of Figure 9, we show the radio-loudness parameter ($R = f_{\rm 5GHz}/f_{2500}$), defined as the ratio of the rest-frame

---

[22] Spectral index α is defined by the power law, $S_\nu \propto \nu^\alpha$.

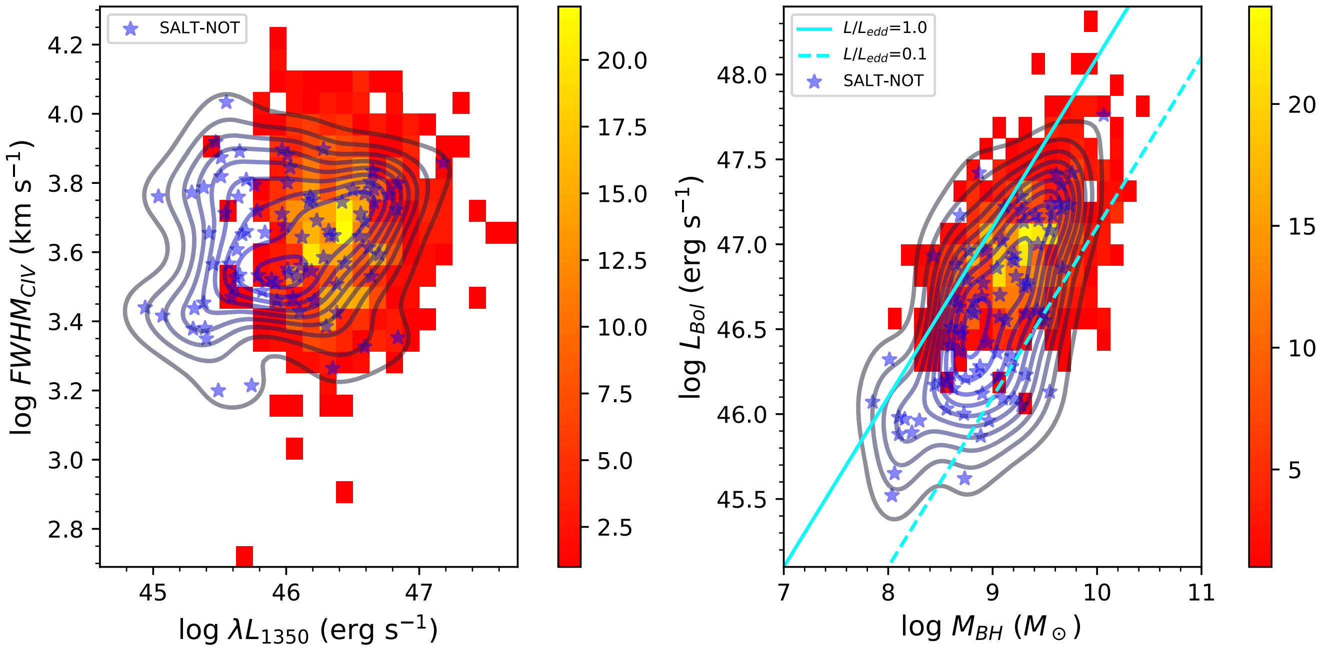

Figure 8. Comparison of luminosity λL_{1350} vs. full C IV FWHM (left), and L_{Bol} vs. $M_{\rm BH}$ (right). In both the panels, the core-dominated quasars from from (Shen et al. 2011) are shown as a 2D histogram, and SALT-NOT quasars are ⋆ and contours.

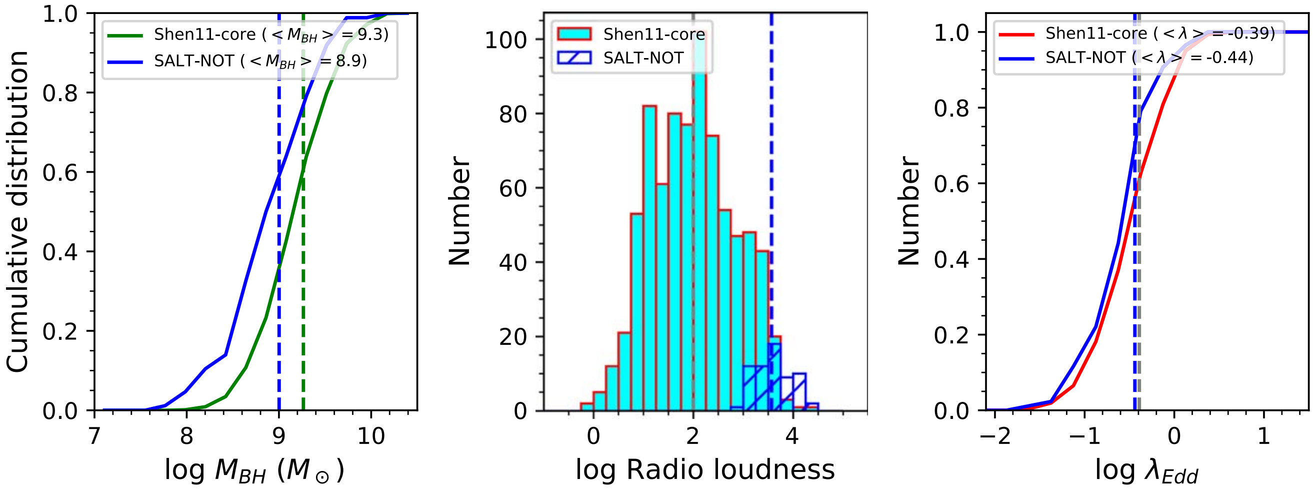

Figure 9. Comparison of BH mass (left), radio loudness (middle), and Eddington ratios (right) for quasars from Shen et al. (2011) and the SALT-NOT sample. The vertical lines represent median values.

flux densities at 5 GHz ($f_{\rm 5GHz}$) and at 2500 Å (f_{2500}) for the two samples. For SALT-NOT quasars, the values of $f_{\rm 5GHz}$ have been estimated using the flux density at 1.4 GHz from NVSS using the spectral slopes $\alpha_{0.4}^{1.4}$ from Gupta et al. (2021b). In cases where $\alpha_{0.4}^{1.4}$ is unavailable, we have used the median $\alpha_{0.4}^{1.4}$ of −0.38 instead. The values of f_{2500} have been estimated by interpolating the PS1 photometry. Clearly, the SALT-NOT sample represents extremely radio-loud quasars (median $R = 3685$). The corresponding Eddington ratio is only slight smaller (median log $\lambda_{\rm Edd} = -0.44$ versus −0.39) as compared to the Shen11-core sample and the difference is statistically insignificant (p-value = 0.02). Thus, over four orders of magnitude covered by the radio loudness in the SALT-NOT and Shen11-core quasars, we see no dependence of radio loudness on the accretion rate. This confirms the saturation of radio loudness observed at low Eddington ratios (see Figure 3 of Sikora et al. 2007).

5.5.2. BAL Occurrence

We focus now on the 105 SALT-NOT AGN showing C IV emission at $z_e \geqslant 1.9$ to search for BALs representing outflowing gas. We exclude seven cases at $z \sim 2.6$ where the blue wing of C IV emission line falls in the CCD gap. In the remaining, we detect four C IV BAL quasars (see Figure 10), i.e., an overall BAL detection rate of $4/98 = 4^{+3}_{-2}\%$. We find a consistent BAL fraction in our reference sample, without any MIR cut, where nine out of 175 quasars at $z \geqslant 2.0$ show C IV BALs ($5 \pm 2\%$).

Typically, 10%–20% of radio sources are detected as BAL QSOs. Becker et al. (2000) studied the properties of radio-selected BAL quasars from First Bright Quasar Survey sample. They also noticed that while the BAL detection rate is high among radio-loud quasars their dependence on the radio luminosity is complex. In particular, the authors find a

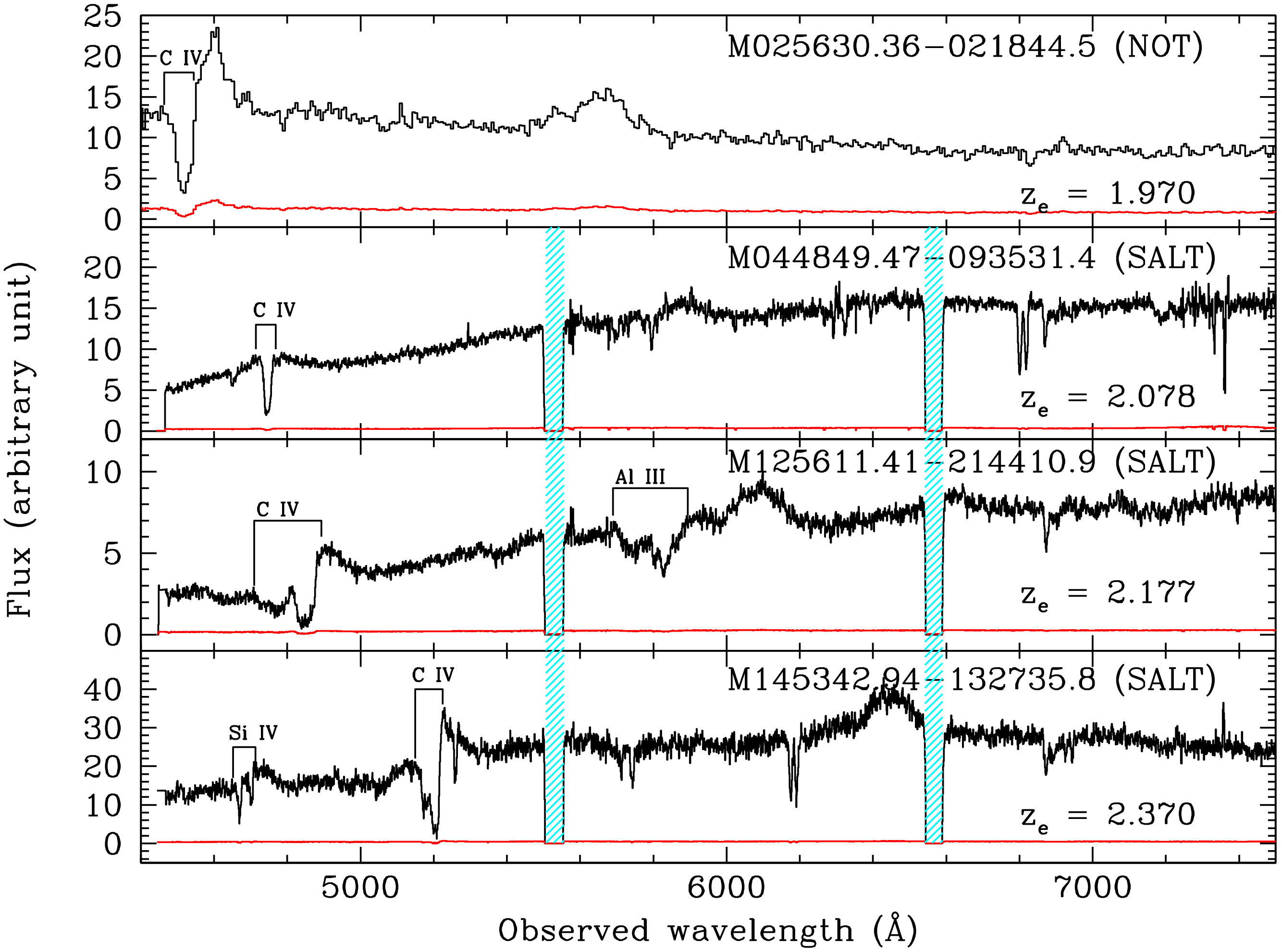

Figure 10. Spectra of four BAL QSOs found in our sample and associated error spectra (in red) are shown. Different BAL absorption are marked in each panel. Hashed regions are the CCD gaps in our SALT observations.

deficiency of BAL QSOs among very radio-bright quasars. Specifically, the BAL fraction drops from $20.5^{+7.3}_{-5.9}\%$ at $L_{1.4\,\mathrm{GHz}}$ $\sim 10^{25}$ W Hz^{-1} to $<8\%$ at $L_{1.4\,\mathrm{GHz}} \sim 3 \times 10^{26}$ W Hz^{-1} (Shankar et al. 2008). The low BAL detection rate in the SALT-NOT sample, which has $L_{1.4\,\mathrm{GHz}} > \sim 10^{27}$ W Hz^{-1}, is consistent with this trend in luminosity.

The radio emission associated with M1453-1327 is extended (largest angular size, $\sim 17.''1$) with a projected linear size of 140 kpc. In the other three cases, the radio emission is dominated by a compact component (projected linear size <5 kpc). This is consistent with the previous results that the radio emission associated with BAL QSOs is compact (Becker et al. 2000). Notably, the four BAL QSOs have $R_{5\mathrm{GHz}/2500\,\text{Å}}$, λ_{Edd} and M_{BH} in the range of $10^{2.9-3.2}$, $10^{0.2-0.5}$, and $10^{9.1-9.8}$ $M_\odot$, respectively, which correspond to objects with the least radio loudness, and highest BH mass and Eddington ratios.

5.6. M1312-2026: A Powerful AGN at z ∼ 5?

The bright radio sources at high-z are extremely rare. This is partly due to the interaction between the emitting electrons and the cosmic microwave background, which makes AGN less luminous in radio (Ghisellini et al. 2014). In the SALT spectrum of M1312-2026 (Figure 11), we identify only a single narrow emission line over the wavelength range covered. If this emission line is Lyα, then the corresponding redshift will be $z = 5.068$. At 4.86 GHz, the radio source has a flux density of 233 mJy and a size of $<2''$ (Table 3), and is unambiguously identified with a WISE and PS1 object with colors that are consistent with it being a high-z radio-loud quasar.

In order to confirm the redshift of M1312-2026, we reobserved the object with X-shooter of the Very Large Telescope on 2022 February 1. In the X-shooter spectrum, we do not detect expected Mg II, C III, and C IV lines corresponding to the presumed Lyα at $z = 5.068$. Instead, the detection of [O III], Hα, and Hβ emission lines confirm the above identified line to be [O II] and the systemic redshift of the quasar to be $z = 0.977$. Further details of the X-shooter spectrum of this highly reddened object will be presented in a future paper.

5.7. Objects without Emission Lines

In recent times, the locus of MIR colors of known Fermi-detected AGN have been used to build large samples of blazars (e.g., Chang et al. 2017; D'Abrusco et al. 2019). These MIR color selection techniques use the first three or all four bands of WISE, and typically extract ∼0.5% (<0.001%) of the overall radio[23] (WISE) source population as blazars. They include both classes of blazars: (i) BL Lacertae objects (BL Lacs) with featureless optical spectra, i.e., no emission lines (equivalent

---

[23] Based on the NVSS sensitivity.

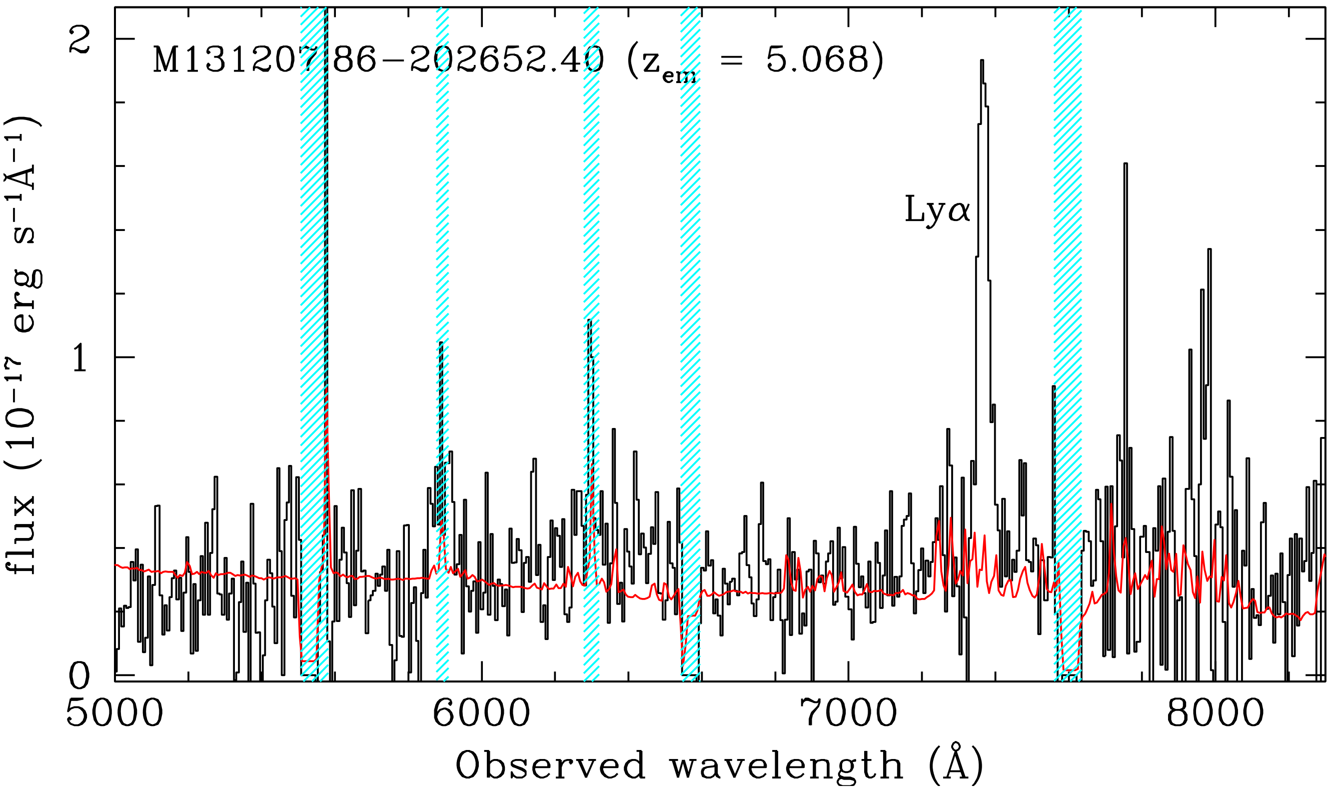

Figure 11. The SALT spectrum of M1312-2026. The overall SALT spectrum and the single emission line assumed to be Lyα at $z = 5.068$ have been consistently reproduced in four individual exposures, two of which were taken using a different spectral setup. The error spectrum is shown in red. The shaded regions (cyan) mark the spectral gap and spectral range affected by sky subtraction residuals. The VLT X-shooter spectrum shows that the actual $z_{em} = 0.977$ (see text for details).

width <5 Å; Stickel et al. 1991), and (ii) flat spectrum, radio-loud quasars (FSRQs) with quasar-like emission lines. In the recent literature, these two classes are also referred to as BZBs, i.e., blazars of BL Lac type and BZQs, i.e., blazars of quasar type, respectively (Massaro et al. 2009).

In the following, we focus on the 26 objects without emission lines (ELLs) in our sample that can be considered candidate BZBs (see Figure 12). The median q_{12} parameter which is defined as the logarithm of the ratio of flux densities measured in the W3 band and at 20 cm of ELL targets is −2.8. This is well outside the range of (−1.85, −1) for BZB candidates based on the locus of Fermi-detected BL Lacs (D'Abrusco et al. 2019, see also Figure 2). The SALT-NOT ELLs thus represent a population of candidate BL Lacs that is underrepresented in the MIR-selected population.

The most crucial and somewhat controversial aspect of establishing the BL Lac nature of AGN is to confirm its featureless optical spectra. Our SALT-NOT spectra are adequate to detect the broad emission lines from AGN but weak lines may be missed due to the poor spectral resolution and noisy data. This is illustrated by the case of two ELL candidates, M0051+1747 and M0105+1845, for which no redshift determination could be established based on the NOT spectra alone. However, these targets have later been observed as part of SDSS and have been identified as AGNs at $z_{em} = 1.536$ and 1.074, respectively. We note that these redshifts are consistent with weak and narrow emission lines in the NOT spectra, which were originally marked as tentative. Thus, the objective of the analysis presented here is to identify BL Lac candidates based on the general properties of blazars: large time variability at all wavelengths and timescales, polarized emission, and a flat or inverted radio spectrum (e.g., Rector & Stocke 2001).

We evaluate the variability of ELLs using the data from the Zwicky Transient Facility (ZTF; Masci et al. 2019). The r-band light curves are available for 15 AGN (median PS1 $r = 19.9$ mag; see Figure A1 in Appendix A). The remaining targets are either not covered (only three) in ZTF or are fainter (median PS1 $r = 20.9$ mag) and have time series with less than 10 data points. From the light curves, we estimate the variability amplitude ($\sigma^2_{\rm rms}$) and error (S^2_D) on it using the normalized excess variance method described in Nandra et al. (1997) and Vaughan et al. (2003). The variability amplitude strength, VAS $= \sigma^2_{\rm rms}/S^2_D$, is provided in Figure A1.

We also estimate the observed $\chi^2_{\rm obs}$ using $\chi^2_{\rm obs} = \sum_{i=1}^{N}(m_i - \overline{m})^2)/\sigma_i^2$, where m_i are N measured fluxes with individual error σ_i and mean $\overline{m}$. The hypothesis of the AGN being intrinsically non-variable can be rejected at 99% confidence level for 11/15 targets. The remaining four targets are among the faintest (PS1 r band: 20.3–21.7 mag) and the conclusion is likely influenced by the low S/N of the light curve. Rejecting these and considering objects with VAS > 3.0, we obtain a sample of four promising (M0022+0608, M0029-1740, M1245-1616, and M2142-2444) and two marginal (M0010-2157 and M0824-1029) BL Lac candidates (see Figure A1). Optical spectrum of M1245-1616 obtained with SALT is shown in Figure 5.

Interestingly, the candidate with the highest VAS (M0022+0608; see Figure A1) is in fact a bona fide γ-ray emitting BL Lac (Massaro et al. 2009). Further, the candidates M0010-2157, M0029-1740, M1245-1616, and M2142-2444 are also identified in the blazar catalog of D'Abrusco et al. (2019) but as

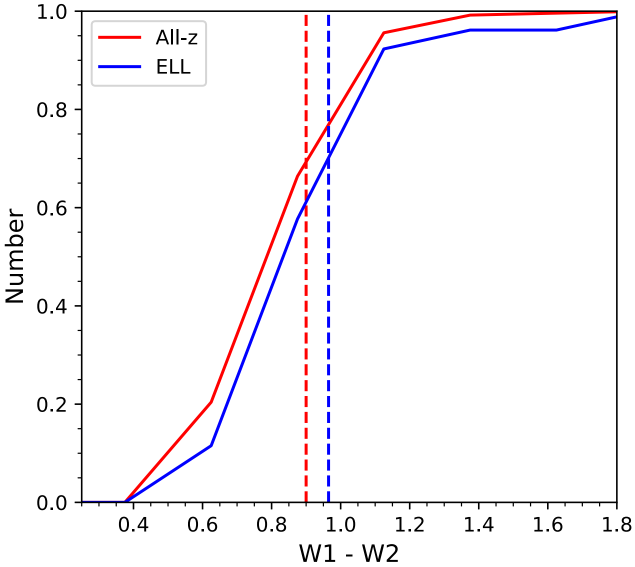

Figure 12. W1-W2 color distribution for SALT-NOT targets with and without redshift determinations. The median values are marked using dashed and dotted lines, respectively.

BZQ candidates on the basis of their position in the three-dimensional (W1-W2-W3-W4) WISE color space based on the locus of confirmed Fermi blazars (Massaro et al. 2009; Acero et al. 2015). Further, 4/6 candidates are also polarized at 2%–4% level in NVSS (Taylor et al. 2009), and except one (M0029-1740) all are core dominated in the VLASS 3 GHz images. Note that it is not unusual for BL Lacs to exhibit extended radio emission (Rector & Stocke 2001).

If the BL Lacs are similarly represented in the 11 remaining ELLs not analyzed due to the lack of ZTF light curves, then we expect another four candidates. In this context, it is also useful to cross-correlate all 26 ELLs with the latest Fermi data release (4FGL DR2; Ballet et al. 2020). We recover previously noted M0022+0608, and find two new matches corresponding to M0010-2157 and M0553-0840.

In summary, we have seven high-probability BL Lac candidates; six identified on the basis of variability analysis and one through crossmatching with γ-ray sources, i.e., a detection rate of 7/303 ($2 \pm 1\%$). Stickel et al. (1991) used 1 Jy sample to estimate the surface density (0.005 for >1 Jy at 5 GHz) of radio-selected BL Lacs. The fraction of BL Lacs in the 1 Jy sample of radio sources brighter than 20 mag (r band) is 15%. Therefore, we expect that better quality data through a targeted optical follow-up will confirm more of these ELLs as BL Lacs.

5.8. DFs

The 27 targets for which there is no firm optical identification, i.e., DFs, are also presented in Table 1. For 14 of these, the stacked PS1 catalog implies optical counterparts with a median i-band magnitude of 22.5 mag (Waters et al. 2020). Clearly, these represent the faintest targets in our sample (see the last panel of Figure 3). On average they are also fainter in WISE (see the last panel of Figure 3). But the W1 magnitudes are still well within the range over which we have successfully obtained optical spectra (middle panel of Figure 3). Thus, misidentifications due to errors in radio–MIR crossmatching is unlikely to significantly contribute to DFs. This is also confirmed by the VLASS–PS1 overlays of 24 DFs covered in PS1 (see Figure A2). In 20/24 cases, the radio source is compact and coincides ($<1''$) with the MIR position marked by the cross. In the remaining four cases, the radio emission is extended, exhibits a double-lobe morphology and the MIR source is located between them, i.e., at the expected location of the AGN.

The above implies that DFs are truly fainter than the implicit magnitude limit of SALT-NOT observations and barely detectable in PS1.[24] Thus, it is reasonable to assume that these have the same redshift distribution (median $z = 1.8$) as the other SALT-NOT targets. The basic statistics of MIR wedge implies that 5% of these are low-redshift radio galaxies. Indeed, upon careful inspection of the PS1 images, we identify diffuse, low-surface brightness emission associated with two targets: M0959-0236 and M1144-1455. These two targets could plausibly be radio galaxies at $z < 1$.

The optical faintness of the remaining DFs, presumably quasars, could be due to (i) an intrinsically low luminosity; (ii) very large amounts of dust in the foreground (intrinsic or intervening) or (iii) a very high redshift ($z > 5$) such that the detectable continuum and emission lines are redshifted into the near-infrared; or (iv) a non-quasar origin of the radio/MIR emission. There is already a tentative indication of a slight excess of intervening and associated DLAs toward optically faint quasars (Ellison et al. 2008; Gupta et al. 2021b). Thus, the identified DFs in our survey may be hiding a small but important population of dusty H I absorbers. The MALS observations of these central DF targets and the other optically faint AGN in the MeerKAT field of view will reveal any such absorbers at $z < 2$.

6. Summary and Outlook

In this paper, we describe a large spectroscopic survey of radio-bright AGN selected based on the following criteria: (i) radio flux density at 1.4 GHz >200 mJy; (ii) $\delta < +20°$; and (iii) WISE MIR colors: W1-W2 $<1.3 \times$ (W2-W3) -3.04 and W1-W2 > 0.6. These criteria are optimized to select powerful quasars at $z > 1.4$. Starting from 25,325 sources brighter than 200 mJy in NVSS we identify 2011 candidate quasars, of which 303 were observed with SALT (180 hr) and NOT (6 nights; Krogager et al. 2018).

The SALT-NOT sample of 303 objects presented in this paper consists of (i) AGN with emission lines in the optical spectrum (250); (ii) objects with no emission lines in the optical spectrum, i.e., (ELLs; 26); and (iii) DFs; 27), i.e., neither emission lines nor a continuum source in the optical spectra or photometry (also see Table 2).

We compare the SALT-NOT sample with the highly complete spectroscopic sample of 10,498 quasars from the SDSS (DR16) in the so-called Stripe 82 region, and with a reference sample of 2294 AGN from SDSS selected by applying the same constraints on the radio flux density and MIR colors as the SALT-NOT sample. We show that our imposed WISE criteria has lead to a sample of radio-bright quasars that are fainter ($\Delta i = 0.6$ mag) and redder ($\Delta(g - i) = 0.2$ mag) than radio-selected quasars in the reference sample, and representative of a fainter quasar population detected in optical surveys.

---

[24] Note that the 5σ depth of the PS1 i-band stack images is 23.1 mag.

Table 2
Summary of SALT-NOT and MALS (Central AGN) Sample

	SALT-NOT	MALS[a]
Number of AGN	303	650[b]
Median flux density (mJy)	300	340[c]
Median W1 (mag)	15.9	15.6
Median i (mag)	19.8	19.4[d]
Inside MIR wedge (Equation (1))	100%	70%
With spectroscopic redshift	83%	79%
Median spectroscopic-z	1.8	1.7

Notes.
[a] Includes SALT-NOT sample.
[b] 70 at $\delta < -40°$ selected using SUMSS. The remaining at $\delta > -40°$ are based on NVSS.
[c] Estimated at 1.4 GHz. SUMSS 0.850 MHz flux densities computed at 1.4 GHz assuming $\alpha = -0.8$.
[d] Only ~550 targets overlapping with PS1 considered. Note slight increase in the i-band brightness due to the inclusion of redshifts from the literature.

About 20% (51/303) of the AGN in our sample only have narrow emission lines. The majority of these (33/51) at $z < 0.5$ are galaxies without strong nuclear emission. In two cases, the emission line is double peaked and likely corresponds to a rare dual AGN. The highest redshift NLAGN (M1513-2524) is at $z = 3.132$. The details of this optically faint ($r > 23$ mag) AGN associated with a large (~90 kpc) and luminous Lyα nebula are presented by Shukla et al. (2021). The double-lobed radio emission associated with M1513-2524 has an extent of 184 kpc. In general, the NLAGN in our sample exhibit extended radio emission with lobes and in some cases cores–the largest being M0909-3133 ($z_{\rm em} = 0.884$) with a projected linear size of 330 kpc.

Based on the reference sample, we expect only 5% of objects in the SALT-NOT sample to be NLAGN. The discrepancy is primarily due to the $z < 0.5$ contaminants. Excluding these would render the z-distribution and BLAGN versus NLAGN composition of the SALT-NOT sample identical to the reference sample. Overall, the application of our WISE color criteria improves the efficiency of identifying $z > 1.4$ AGN by a factor of ~1.7 (i.e., from ~30% to ~50%).

We discuss in detail the properties of the 110 SALT-NOT AGN at $1.9 < z < 3.5$. The four NLAGN in this subsample show emission line ratios similar to high-z radio galaxies. The radio emission associated with two of these (M1315-2745 and M1513-2524) are among the largest at these redshifts (280 and 184 kpc, respectively). We estimate bolometric luminosities, radio-loudness parameters ($R = f_{5\rm GHz}/f_{2500\,\text{Å}}$), BH masses ($M_{\rm BH}$), and Eddington ratios of the remaining 106 AGN in this subsample. In comparison to the optically selected core-dominated SDSS quasars from Shen et al. (2011), the SALT-NOT quasars are fainter (~0.5 dex lower L_{1350}) and, consequently, have lower (~0.4 dex) $M_{\rm BH}$. It is intriguing to note that despite representing the most radio-loud quasars (median $R = 3685$), the Eddington ratios of our objects are similar to the less radio-loud (median $R = 100$) SDSS quasars. In fact, we do not find any dependence between radio loudness and Eddington ratio in the SALT-NOT and SDSS quasar samples spanning four orders of magnitude in R. This confirms the saturation of radio loudness observed at low Eddington ratios (Sikora et al. 2007), and the significance of physical parameters such as BH spin and the in situ magnetic field in influencing the overall appearance of AGN.

Among $1.9 < z < 3.5$ AGN, we also detect four C IV BAL quasars. All are associated with objects of least radio loudness, and highest BH masses and Eddington ratios. The low BAL quasar detection rate 4^{+3}_{-2}%) is consistent with that seen in extremely powerful ($L_{1.4\rm GHz} > 10^{25}$ W Hz^{-1}) radio-loud quasars (Shankar et al. 2008). The systematic H I 21 cm absorption line search in these quasars suggests deficiency of cold atomic gas at host galaxy scales (Gupta et al. 2021b). In this context, it will be interesting to confirm the slight excess of proximate DLAs observed in our sample (Gupta et al. 2021b). The details of gaseous environment of these quasars at larger (>10 kpc) scales are presented in a separate paper (Shukla et al. 2022).

Based on detailed optical variability analysis, radio polarization, and γ-ray properties we identify seven high-probability BL Lacs among 26 ELLs in our sample. Better quality optical spectra will likely confirm a larger fraction of these ELLs as bona fide BL Lacs. Finally, we discuss 27 DFs in our sample which could be due to (i) an intrinsically low luminosity; (ii) very large amounts of dust in the foreground (intrinsic or intervening) or (iii) a very high redshift ($z > 5$) such that the continuum is strongly absorbed by the intervening Lyα forest and emission lines are redshifted into the near-infrared; or (iv) a non-quasar origin of the radio/MIR emission.

The selection criteria of SALT-NOT sample are based on the requirements of MALS. The entire MALS footprint of ~500 pointings each at L and UHF bands is based on the SALT-NOT sample presented here and additional ~350 bright radio sources selected from the literature. The overall properties of this larger pool of 650 AGN are presented in Table 2 (see also Figure 13 for the survey footprint and overlap with various optical surveys).

The complete details of the MALS sample will be provided in future papers. But, in short, these additional sources are AGN: (i) with known spectroscopic redshift and $\delta > -40°$ from the literature (see Figure 1, i.e., the green box with 597 AGN), and (ii) brighter than 200 mJy at 843 MHz and $\delta < -40°$ in the SUMSS (Mauch et al. 2003). Further, priority has been given to AGN having excellent multiwavelength data or close to nearby ($z < 0.1$) galaxies. This extended sky coverage through a larger pool of 650 sources offers flexibility in selecting pointings for the observations, and maximizing the scientific output corresponding to various galaxies and AGN detected within the MALS field of view (see Gupta et al. 2016 for some of the science cases).

Currently, ~400 pointings mostly at the L band have already been observed (Figure 13). Looking forward, MALS will continue to observe with the MeerKAT from 2021–2022 and afterward primarily in the UHF band. We plan to release all radio continuum images and spectra along with the catalogs of detected sources and spectral lines through our survey website: https://mals.iucaa.in. This will include multiwavelength data such as the SALT-NOT spectra presented here. We expect all these to be an excellent resource for the astronomical community for a broad range of galactic and extragalactic applications.

We thank the anonymous referee for useful comments and suggestions. P.P.J. was supported in part by the French National Research Agency (ANR) under contract No. ANR-16-CE310021. P.P.J. thanks Camille Nóus (Laboratoire

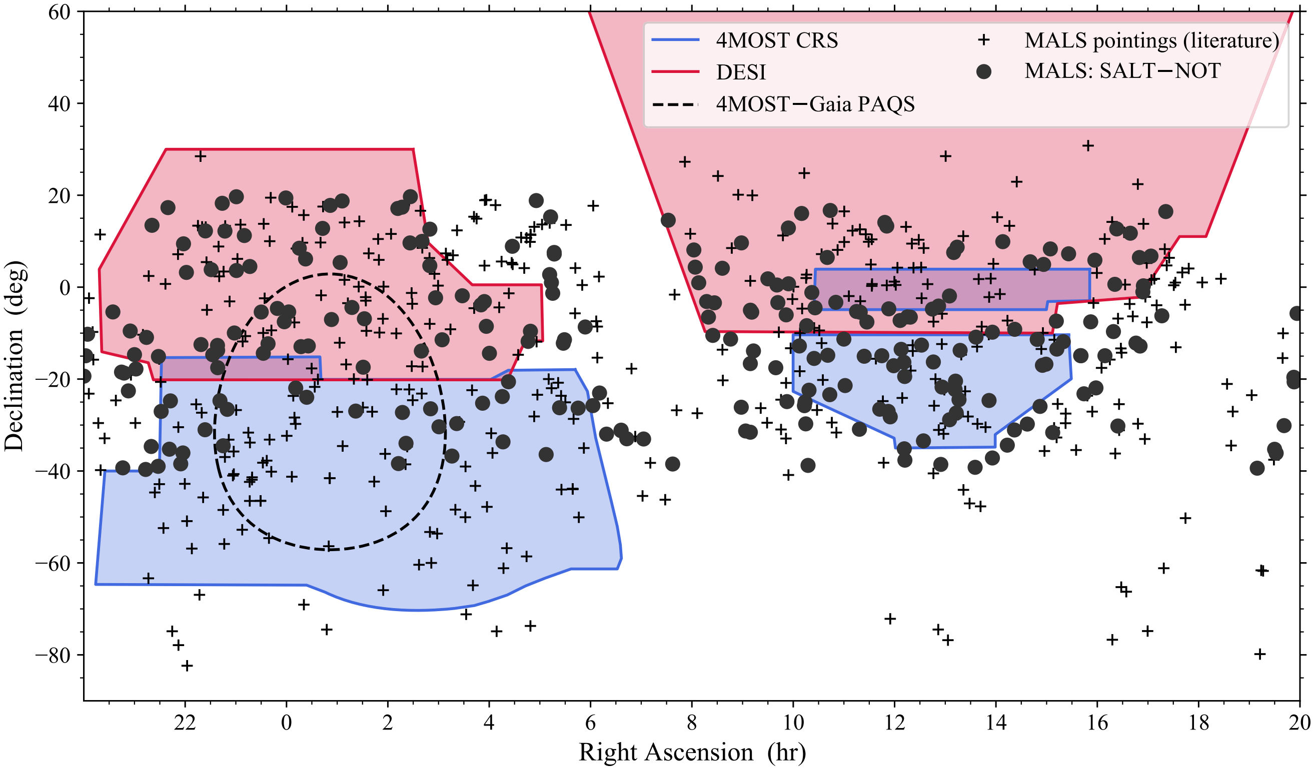

Figure 13. Compilation of MALS pointings from the literature (black crosses) and from our dedicated SALT and NOT observations (solid circles). Overlaid are the footprints of a few upcoming spectroscopic surveys: DESI (red), 4MOST Cosmology Redshift Survey (CRS; blue) and the 4MOST-Gaia Purely Astrometric Quasar Survey (PAQS; black dashed line). Note that ESO's 4MOST-Gaia PAQS survey (PI: Krogager) will observe 120,000 targets over 5 yr.

Cogitamus) for often unnoticed discussions, advice, and support. This work is based on observations made with SALT and NOT. We thank the NOT and SALT staff for their support during the observations. The National Radio Astronomy Observatory is a facility of the National Science Foundation operated under cooperative agreement by Associated Universities, Inc. Based on observations obtained with the Samuel Oschin Telescope 48 inch and the 60 inch Telescope at the Palomar Observatory as part of the Zwicky Transient Facility project. ZTF is supported by the National Science Foundation under grant No. AST-2034437 and a collaboration including Caltech, IPAC, the Weizmann Institute for Science, the Oskar Klein Center at Stockholm University, the University of Maryland, Deutsches Elektronen-Synchrotron and Humboldt University, the TANGO Consortium of Taiwan, the University of Wisconsin at Milwaukee, Trinity College Dublin, Lawrence Livermore National Laboratories, and IN2P3, France. Operations are conducted by COO, IPAC, and UW.

Appendix A
Properties of the MALS SALT-NOT Sample

The properties of AGNs in the SALT-NOT sample are provided in Table 3. The ZTF light curves and radio-optical overlays for ELLs and DFs, respectively, are also provided (see Figures A1 and A2).

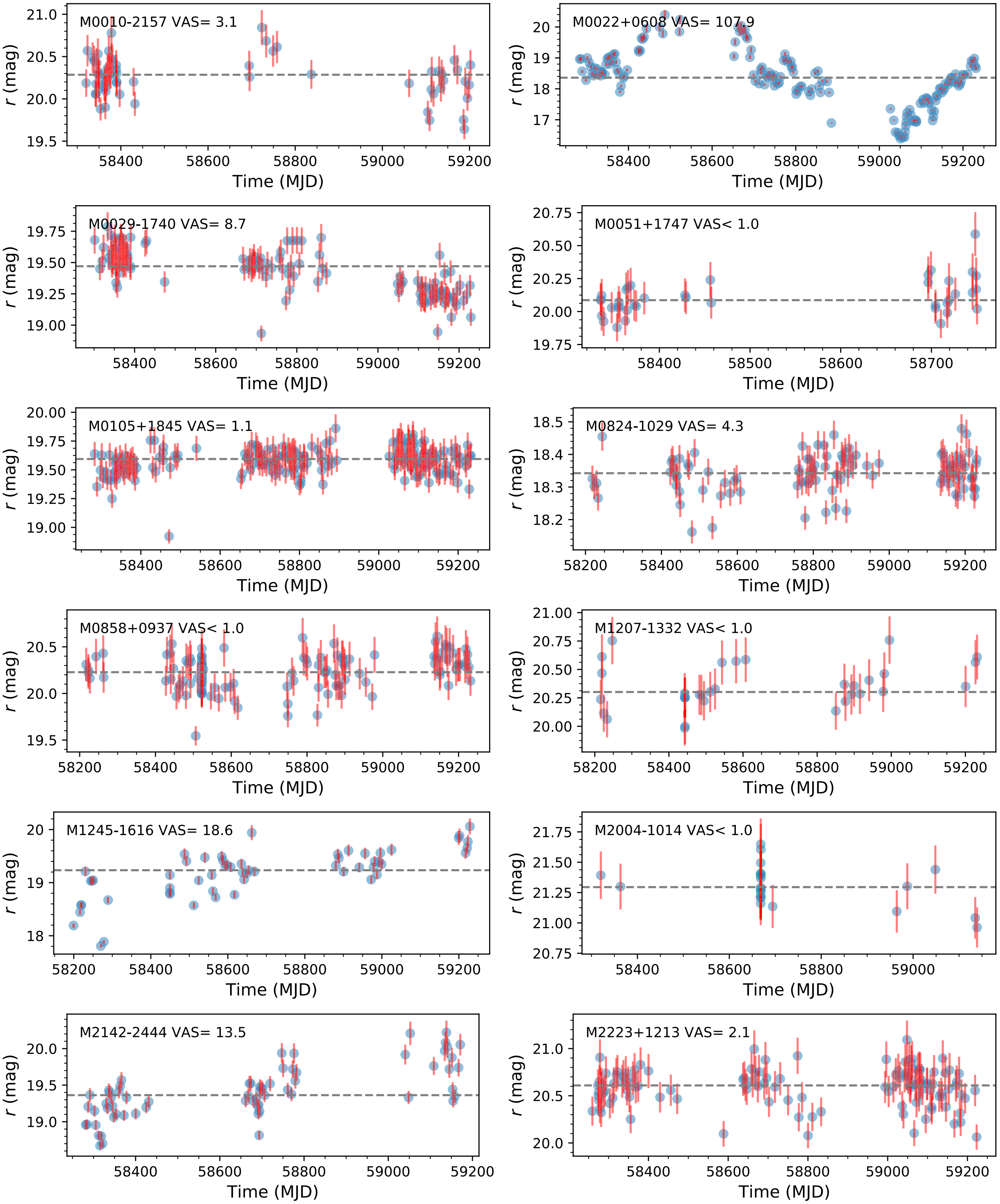

Figure A1. ZTF light curves (*r* band) and the variability amplitude strength (VAS) for targets with no emission lines. The horizontal dashed line represents the median value.

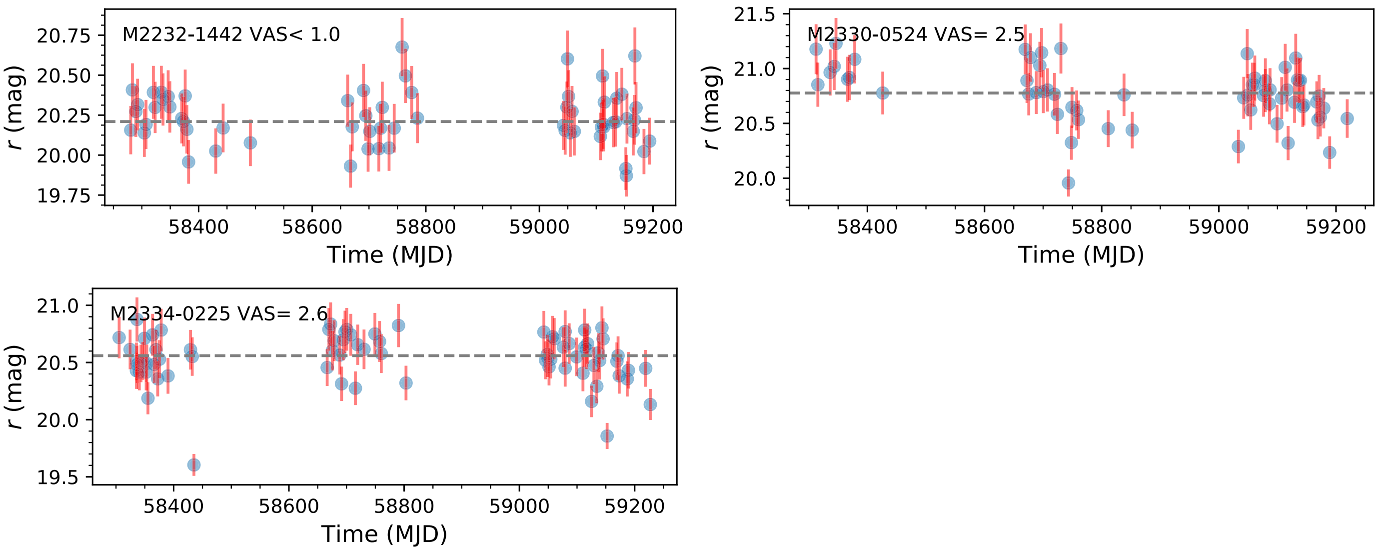

Figure A1. (Continued.)

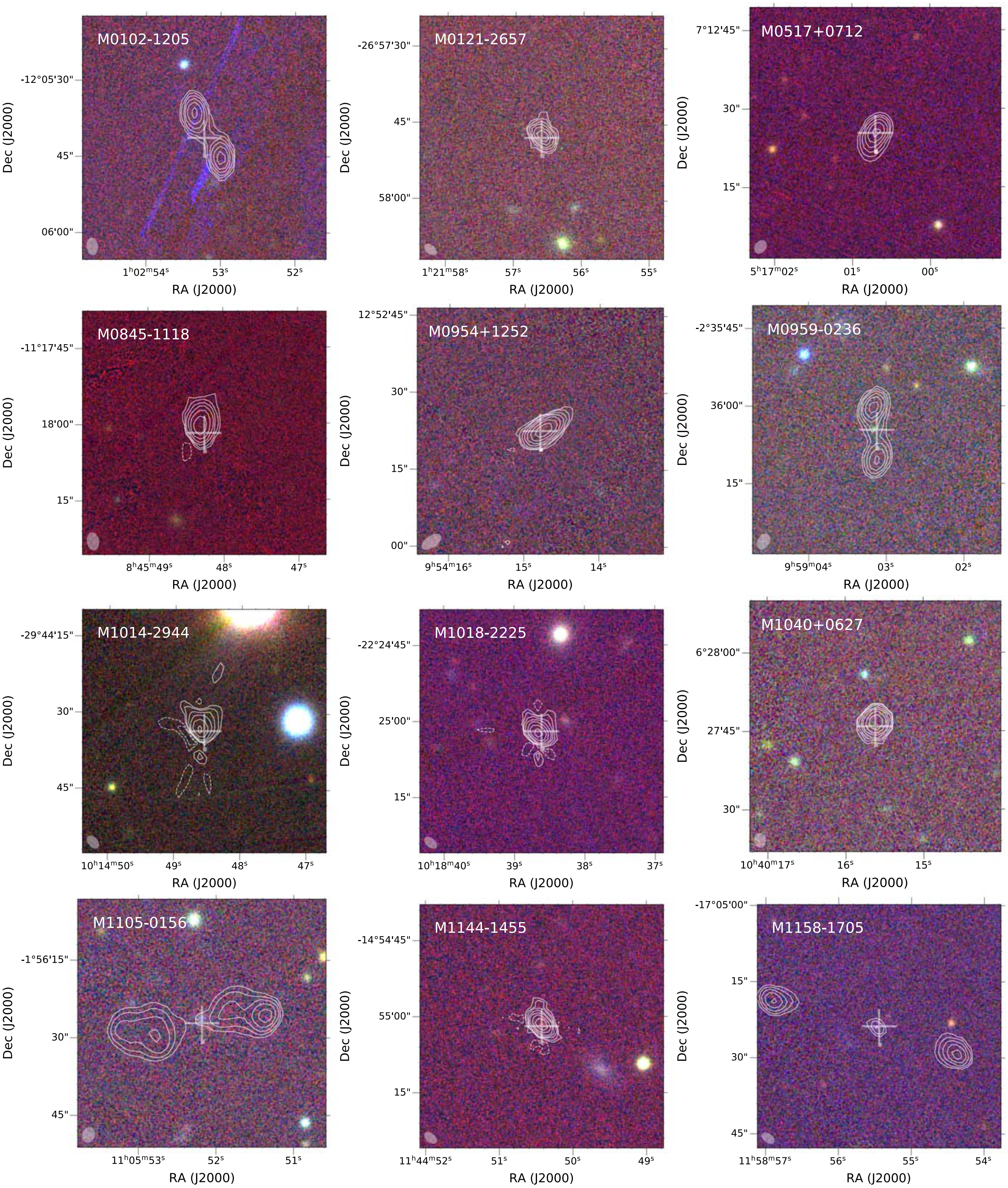

Figure A2. VLASS (3 GHz) contours overlaid on PS1 *yig* color composite images. The contour levels are shown at 1.5 × (−1, 1, 2, 4, 8, ...) mJy beam^{-1}. The synthesized beam is shown at the bottom left corner. The position of WISE source is marked with a cross.

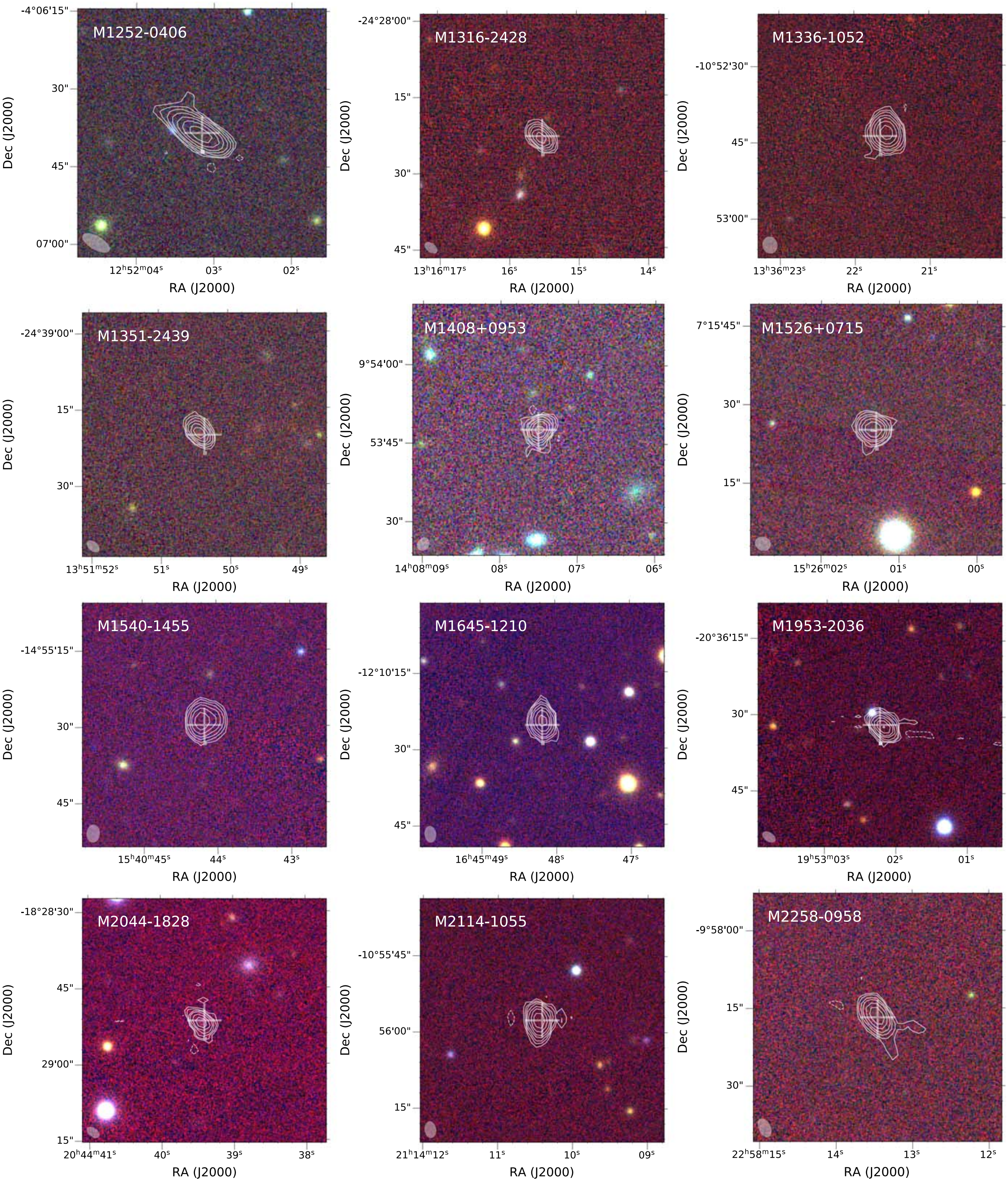

Figure A2. (Continued.)

Table 3
Flux Densities of M1312-2026

Frequency (GHz)	Flux (mJy)	Deconvolved Size	Ref.
0.23	2577	$7\farcs1 \times 3\farcs3$, $0\fdg0$	(1)
1.39	677	$0\farcs8 \times 0\farcs2$, $5\fdg0$	(2)
1.40	778	$<17\farcs9$	(3)
4.86	233	$<2''$	(4)

References: (1) Gupta et al. (2021b); (2) This work. Observed on 2018 July 14 for 10 minutes (on-source time) using uGMRT with a 200 MHz wideband covering 1260–1460 MHz.); (3) NVSS; (4) Kapahi et al. (1998).

Appendix B
Notes on Individual Targets

Here we briefly summarize the properties of interesting individual targets relevant to discussions in Sections 5.2–5.5.

B.1. AGN at $z < 0.5$

1. M0314-0909 ($z_{\rm em} = 0.312$) and M1024-0852 ($z_{\rm em} = 0.455$): the associated radio emission has projected linear sizes of 240–250 kpc.
2. M0133-0256 ($z_{\rm em} = 0.259$) and M1703+0645 ($z_{\rm em} = 0.399$): these show double-peaked emission lines. For the former, the AGN host also shows signs of interaction with a nearby galaxy.
3. J0609+0217 ($z_{\rm em} = 0.174$) and M1219-1809 ($z_{\rm em} = 0.189$): the host galaxies are part of an interacting group of galaxies.

B.2. AGN at $0.5 < z < 1.0$

1. M0909-3133 ($z_{\rm em} = 0.884$): the radio emission associated with this NLAGN has an extent of 330 kpc. The optical spectrum is shown in Figure 5).
2. M2220+1307 ($z_{\rm em} = 0.760$): the projected linear size of radio emission associated with this BLAGN is 180 kpc.
3. M1440+0531, M2058-1736, and M2059-1440: these have distorted radio morphologies suggesting interaction with the ambient medium.

B.3. AGN at $1.0 < z < 1.9$

1. M0552-3459 ($z_{\rm em} = 1.776$): this NLAGN has clear detections of He II, C III, C II, and Ne IV (see Figure 5). The FWHM measured based on the C III emission line is 835 km s^{-1}. At 3 GHz, the associated radio emission is resolved into two lobes separated by $8\farcs3$ (71 kpc).
2. M1033-1210 ($z_{\rm em} = 1.328$): Krogager et al. (2018) identified this as a NLAGN based on the presence of a narrow [O II] line and the absence of broad emission lines like Mg II and C III. In this case too the radio emission is resolved into a double-lobed morphology with a separation of $3\farcs2$ (28 kpc).
3. M0956-1317 ($z_{\rm em} = 1.198$): the associated radio emission has an extent of $23\farcs3$ (194 kpc), which is the largest in our sample among the AGN at $1.0 < z < 1.9$.

B.4. AGN at $1.9 < z < 3.5$

1. M0516+0732 ($z_{\rm em} = 2.594$): the radio emission associated with this NLAGN is compact with a deconvolved size of $<0\farcs5$, i.e., <4 kpc. It also shows strong continuum emission in the optical spectrum. The C IV emission profile may be affected by the associated absorption. We measure the Lyα to C IV emission line ratio, $f_{{\rm Ly}\alpha}/f_{\rm C\,IV} = 2.40 \pm 0.10$. This is similar to the ratios observed in high-z radio galaxies.
2. M1315-2745 ($z_{\rm em} = 1.911$): the radio emission associated with this NLAGN exhibits a double-lobed morphology with an extent of $32\farcs8$ (280 kpc). We detect the emission lines of C IV, He II, C III, C II, and Ne IV. The optical continuum emission is very weak. While we do not clearly detect the AGN in PS1 images, it is clearly seen in the WISE image. The deconvolved velocity width of the C IV emission line is 375 km s^{-1}. The ratio $f_{C\,\rm IV}/f_{\rm He\,II}$ is found to be 1.88 ± 0.34. This is typical of ratios observed in high-z radio galaxies (see, for example, Figure 6 of Shukla et al. 2021, and references therein) but more than what is seen in typical quasars.
3. M1455-0957 ($z_{\rm em} = 1.995$): the double-lobed radio emission associated with this NLAGN has an extent of $8\farcs1$ (i.e., 69 kpc). The optical and IR characteristics are also very similar to M1315-2745. The C IV, He II, C III, C II, and Ne IV emission lines are clearly detected. The deconvolved velocity width of the C IV emission line is 430 km s^{-1}. We estimate $f_{C\,\rm IV}/f_{\rm He\,II} = 0.69 \pm 0.14$, which is again typical of the ratios observed in high-z radio galaxies.
4. M1513-2524 ($z_{\rm em} = 3.132$): this NLAGN is associated with a double-lobed radio emission with an extent of $23\farcs7$ (184 kpc). It exhibits extended Lyα, C IV, and He II emission. The detailed analysis of this object is presented by Shukla et al. (2021).

ORCID iDs

N. Gupta https://orcid.org/0000-0001-7547-4241
R. Srianand https://orcid.org/0000-0002-9062-1921
J.-K. Krogager https://orcid.org/0000-0002-4912-9388
P. Noterdaeme https://orcid.org/0000-0002-5777-1629
A. J. Baker https://orcid.org/0000-0002-7892-396X
F. Combes https://orcid.org/0000-0003-2658-7893
J. P. U. Fynbo https://orcid.org/0000-0002-8149-8298
E. Momjian https://orcid.org/0000-0003-3168-5922
M. Hilton https://orcid.org/0000-0002-8490-8117
K. Moodley https://orcid.org/0000-0001-6606-7142
J. Jose https://orcid.org/0000-0003-0608-6258
K. Knowles https://orcid.org/0000-0002-8452-0825

References

Acero, F., Ackermann, M., Ajello, M., et al. 2015, ApJS, 218, 23
Assef, R. J., Stern, D., Noirot, G., et al. 2018, ApJS, 234, 23
Assef, R. J., Kochanek, C. S., Brodwin, M., et al. 2010, ApJ, 713, 970
Balashev, S. A., & Noterdaeme, P. 2018, MNRAS, 478, L7
Ballet, J., Burnett, T. H., Digel, S. W., & Lott, B. 2020, arXiv:2005.11208
Barrows, R. S., Comerford, J. M., Stern, D., & Assef, R. J. 2021, ApJ, 922, 179
Becker, R. H., White, R. L., Gregg, M. D., et al. 2000, ApJ, 538, 72
Becker, R. H., White, R. L., & Helfand, D. J. 1995, ApJ, 450, 559
Boettcher, E., Chen, H.-W., Zahedy, F. S., et al. 2021, ApJ, 913, 18
Burgh, E. B., Nordsieck, K. H., Kobulnicky, H. A., et al. 2003, Proc. SPIE, 4841, 1463
Chambers, K. C., Magnier, E. A., Metcalfe, N., et al. 2016, arXiv:1612.05560
Chang, Y. L., Arsioli, B., Giommi, P., & Padovani, P. 2017, A&A, 598, A17

Coatman, L., Hewett, P. C., Banerji, M., & Richards, G. T. 2016, MNRAS, 461, 647

Combes, F., Gupta, N., Muller, S., et al. 2021, A&A, 648, A116

Condon, J. J., Cotton, W. D., Greisen, E. W., et al. 1998, AJ, 115, 1693

Crawford, S. M., Still, M., Schellart, P., et al. 2010, Proc. SPIE, 7737, 773725

Cutri, R. M., Wright, E. L., Conrow, T., et al. 2014, yCat, 2328

D'Abrusco, R., Álvarez Crespo, N., Massaro, F., et al. 2019, ApJS, 242, 4

Denney, K. D., Peterson, B. M., Pogge, R. W., et al. 2010, ApJ, 721, 715

Ellison, S. L., Yan, L., Hook, I. M., et al. 2001, A&A, 379, 393

Ellison, S. L., York, B. A., Pettini, M., & Kanekar, N. 2008, MNRAS, 388, 1349

Fabian, A. C. 2012, ARA&A, 50, 455

Frank, S., & Péroux, C. 2010, MNRAS, 406, 2235

Ghisellini, G., Celotti, A., Tavecchio, F., Haardt, F., & Sbarrato, T. 2014, MNRAS, 438, 2694

Gupta, N., Jagannathan, P., Srianand, R., et al. 2021a, ApJ, 907, 11

Gupta, N., Srianand, R., Baan, W., et al. 2016, in Proc. of Science 277, MeerKAT Science: On the Pathway to the SKA, ed. R. Taylor (Trieste: Sissa Medialab), 14

Gupta, N., Srianand, R., & Saikia, D. J. 2005, MNRAS, 361, 451

Gupta, N., Srianand, R., Shukla, G., et al. 2021b, ApJS, 255, 28

Heckman, T. M., & Best, P. N. 2014, ARA&A, 52, 589

Hickox, R. C., & Alexander, D. M. 2018, ARA&A, 56, 625

Jauncey, D. L., Reynolds, J. E., Tzioumis, A. K., et al. 1991, Natur, 352, 132

Jonas, J. & MeerKAT Team 2016, in Proc. of Science 277, MeerKAT Science: On the Pathway to the SKA, ed. R. Taylor et al. (Trieste: Sissa Medialab), 1

Kapahi, V. K., Athreya, R. M., van Breugel, W., McCarthy, P. J., & Subrahmanya, C. R. 1998, ApJS, 118, 275

Kaspi, S., Smith, P. S., Netzer, H., et al. 2000, ApJ, 533, 631

Kobulnicky, H. A., Nordsieck, K. H., Burgh, E. B., et al. 2003, Proc. SPIE, 4841, 1634

Krogager, J.-K., Fynbo, J. P. U., Møller, P., et al. 2019, MNRAS, 486, 4377

Krogager, J. K., Gupta, N., Noterdaeme, P., et al. 2018, ApJS, 235, 10

Lacy, M., Storrie-Lombardi, L. J., Sajina, A., et al. 2004, ApJS, 154, 166

Lacy, M., Baum, S. A., Chandler, C. J., et al. 2020, PASP, 132, 035001

Laor, A. 2000, ApJL, 543, L111

Ledoux, C., Petitjean, P., & Srianand, R. 2003, MNRAS, 346, 209

Liu, X., Shen, Y., Strauss, M. A., & Greene, J. E. 2010, ApJ, 708, 427

Lu, Y., Wang, T., Zhou, H., & Wu, J. 2007, AJ, 133, 1615

Masci, F. J., Laher, R. R., Rusholme, B., et al. 2019, PASP, 131, 018003

Massaro, E., Giommi, P., Leto, C., et al. 2009, A&A, 495, 691

Mateos, S., Alonso-Herrero, A., Carrera, F. J., et al. 2012, MNRAS, 426, 3271

Mathur, S., & Nair, S. 1997, ApJ, 484, 140

Mauch, T., Murphy, T., Buttery, H. J., et al. 2003, MNRAS, 342, 1117

McConnell, D., Hale, C. L., Lenc, E., et al. 2020, PASA, 37, e048

Mullaney, J. R., Alexander, D. M., Fine, S., et al. 2013, MNRAS, 433, 622

Murphy, M. T., & Liske, J. 2004, MNRAS, 354, L31

Muzahid, S., Srianand, R., & Charlton, J. 2015, MNRAS, 448, 2840

Nandra, K., George, I. M., Mushotzky, R. F., Turner, T. J., & Yaqoob, T. 1997, ApJ, 476, 70

Netzer, H., Lutz, D., Schweitzer, M., et al. 2007, ApJ, 666, 806

Noterdaeme, P., Ledoux, C., Petitjean, P., & Srianand, R. 2008, A&A, 481, 327

Noterdaeme, P., Petitjean, P., Ledoux, C., & Srianand, R. 2009, A&A, 505, 1087

Noterdaeme, P., Srianand, R., Rahmani, H., et al. 2015, A&A, 577, A24

Onken, C. A., Ferrarese, L., Merritt, D., et al. 2004, ApJ, 615, 645

Padovani, P., Alexander, D. M., Assef, R. J., et al. 2017, A&ARv, 25, 2

Parks, D., Prochaska, J. X., Dong, S., & Cai, Z. 2018, MNRAS, 476, 1151

Pei, Y. C., Fall, S. M., & Bechtold, J. 1991, ApJ, 378, 6

Petitjean, P., Srianand, R., & Ledoux, C. 2000, A&A, 364, L26

Planck Collaboration, Aghanim, N., Akrami, Y., et al. 2020, A&A, 641, A6

Pontzen, A., & Pettini, M. 2009, MNRAS, 393, 557

Pramesh Rao, A., & Subrahmanyan, R. 1988, MNRAS, 231, 229

Rector, T. A., & Stocke, J. T. 2001, AJ, 122, 565

Richards, G. T., Fan, X., Newberg, H. J., et al. 2002, AJ, 123, 2945

Richards, G. T., Lacy, M., Storrie-Lombardi, L. J., et al. 2006, ApJS, 166, 470

Sanders, D. B., & Mirabel, I. F. 1996, ARA&A, 34, 749

Satyapal, S., Secrest, N. J., Ricci, C., et al. 2017, ApJ, 848, 126

Shankar, F., Dai, X., & Sivakoff, G. R. 2008, ApJ, 687, 859

Shen, Y., Richards, G. T., Strauss, M. A., et al. 2011, ApJS, 194, 45

Shukla, G., Srianand, R., Gupta, N., et al. 2021, MNRAS, 501, 5362

Shukla, G., Srianand, R., Gupta, N., et al. 2022, MNRAS, 510, 786

Sikora, M., & Begelman, M. C. 2013, ApJL, 764, L24

Sikora, M., Stawarz, Ł., & Lasota, J.-P. 2007, ApJ, 658, 815

Srianand, R., Gupta, N., Petitjean, P., et al. 2012, MNRAS, 421, 651

Srianand, R., & Kembhavi, A. 1997, ApJ, 478, 70

Stern, D., Eisenhardt, P., Gorjian, V., et al. 2005, ApJ, 631, 163

Stern, D., Assef, R. J., Benford, D. J., et al. 2012, ApJ, 753, 30

Stickel, M., Padovani, P., Urry, C. M., Fried, J. W., & Kuehr, H. 1991, ApJ, 374, 431

Taylor, A. R., Stil, J. M., & Sunstrum, C. 2009, ApJ, 702, 1230

Urry, C. M., & Padovani, P. 1995, PASP, 107, 803

Vaughan, S., Edelson, R., Warwick, R. S., & Uttley, P. 2003, MNRAS, 345, 1271

Vestergaard, M., & Peterson, B. M. 2006, ApJ, 641, 689

Waters, C. Z., Magnier, E. A., Price, P. A., et al. 2020, ApJS, 251, 4

Wiklind, T., & Combes, F. 1996, Natur, 379, 139

Wolfe, A. M., Gawiser, E., & Prochaska, J. X. 2005, ARA&A, 43, 861

Wolfe, A. M., & Prochaska, J. X. 2000, ApJ, 545, 591

Wright, E. L., Eisenhardt, P. R. M., Mainzer, A. K., et al. 2010, AJ, 140, 1868

Zahedy, F. S., Chen, H.-W., Boettcher, E., et al. 2020, ApJL, 904, L10